Light-based tomography

for mixing in bio-reactors

Rafal Fiuk

TUDelft

Light-based tomography

for mixing in bio-reactors

by

Rafal Fiuk

Student number:	137534	
Project duration:	December 1, 2023 – July 1, 2023	
Faculty:	Faculty of Applied Natural Sciences, Delft	
Thesis committee:	Dr. ir. Cees Haringa,	TU Delft, supervisor
	Dr. Luis Portela	TU Delft
	Dr. Adrie J.J. Straathof,	TU Delft

Preface

This thesis is submitted in partial fulfilment of the requirements for the Master of Chemical Engineering at Delft University of Technology. Throughout the course of this research, I had the unique opportunity to delve deep into the intricate world of tomographic reconstruction and imaging. This exploration not only expanded my understanding of this complex field but also unexpectedly offered me the chance to hone my woodworking skills.

I would like to express my deepest gratitude to my supervisor, Dr. ir. Cees Haringa, from the Biotechnology Department, for his invaluable guidance, patience, and support throughout the course of this research. His expertise and insights have been instrumental in shaping this work.

Lastly, I would also like to extend heartfelt thanks to my family and friends whose unfailing support has been a steady source of comfort and encouragement. Above all, my deepest gratitude goes to my partner, whose support has been indispensable. Without them, the completion of this research would not have been possible.

Rafal Fiuk
Delft, July 2023

Summary

Presented works describe a novel approach to assess mixing in a stirred vessel using light-based tomography. The study is driven by key research questions: What are the obstacles in three-dimensional dynamic tracer distribution reconstruction? How should the experimental equipment be constructed to obtain the best possible data from three cameras recording the back-lit stirred tank? How can raw images be processed to isolate the ray-dye interaction? And, how can relevant mixing information be obtained from projections and reconstructed volumetric data?

The research begins with a short introduction of traditional mixing measurement techniques, establishing the context and relevance of the work. The theoretical background of the study is then presented, including the principles of tomographic reconstruction and the main algorithms used in the process.

The methodology involves the use of synthetic data obtained from LES for the framework and baseline creation followed by the acquisition of experimental data. A significant part of the methodology is dedicated to image pre-processing, which incorporates as main steps the inverted grayscale transformation, brightness normalization, background removal using image similarity metrics and object removal with the use of a neural network. The use of the simplistic forward model based on the Lambert-Beer law is described, followed by the implementation of the projection matrix-free Simultaneous Algebraic Reconstruction Technique.

The outcomes of both synthetic and experimental data reconstruction are presented and despite the shortcomings of the used experimental setup the 2D and 3D mixing maps were created, supported by the local Coefficient of Variance calculation to gain further insight into the process.

The conclusions highlight the potential of light-based tomography for evaluating mixing while acknowledging the need for significant refinement and validation of the methodology. Recommendations include the improvement of imaging, equipment modifications, and reconstruction implementation.

Contents

Preface i

Summary ii

Nomenclature v

1 Introduction 1
- 1.1 Context and Relevance 1
  - 1.1.1 Traditional mixing measurement 1

2 Theoretical Background 3
- 2.1 Mixing definition 3
- 2.2 Tomographic reconstruction principles & main algorithms 4
  - 2.2.1 Main algorithms - iterative reconstruction 4
- 2.3 Research Definition 6
  - 2.3.1 Pre-eliminary literature study 6

3 Methodology 8
- 3.1 Synthetic data - framework development 8
- 3.2 Experimental data acquisition 9
  - 3.2.1 Equipment description 10
  - 3.2.2 Limitations 13
- 3.3 Image pre-processing pipeline 13
  - 3.3.1 Manual steps 14
  - 3.3.2 Brightness normalization 15
  - 3.3.3 Background removal 16
  - 3.3.4 Use of YOLOv7 17
- 3.4 Reconstruction 20
  - 3.4.1 Reconstruction algorithm implementation 21
- 3.5 Mixing quantification 23
  - 3.5.1 Global mixing times 23
  - 3.5.2 Local mixing times 24
  - 3.5.3 Concentration calibration 27

4 Results & discussion 29
- 4.1 Synthetic data reconstruction 29
  - 4.1.1 Image reconstruction 29
  - 4.1.2 3D tracer distribution reconstruction 32
  - 4.1.3 Mixing 34
- 4.2 Experimental data reconstruction 37
  - 4.2.1 Image reconstruction 37
  - 4.2.2 3D structure reconstruction 39
  - 4.2.3 Mixing 41

5 Conclusions & Recommendations 44
- 5.1 Conclusions 44
- 5.2 Recommendations 45

References 47

A 50
- A.1 Sythetic frames reconstruction errors 50
- A.2 Synthetic data reconstruction, reference & local CoV 52

A.3 Experimental data reconstruction & local CoV 61
A.4 Experimental data mixing maps 69

Nomenclature

Abbreviations

Abbreviation	Definition
ART	Algebraic Reconstruction Technique
CFD	Computational Fluid Dynamics
CoV	Coefficient of Variation
CT	Computed Tomography
CSV	Comma-Separated Values
EHS	Error Histogram Similarity
FBP	Filtered Back Projection
FPS	Frames Per Second
GPU	Graphics Processing Unit
IoU	Intersection over Union
ISSM	Information theoretic-based Statistic Similarity Measure
LES	Large Eddy Simulations
mAP50	mean Average Precision with Intersection over Union of 50%
mAP50-95	mean Average Precision with IoU from 50% to 95%
MSSIM	Mean Structural Similarity Index
Numpy	Numerical Python
OpenCV	Open Source Computer Vision Library
P	Precision
RMSE	Root Mean Square Error
SART	Simultaneous Algebraic Reconstruction Technique
SHS	Shannon–Histogram Similarity
SIRT	Simultaneous Iterative Reconstructive Technique
SSIM	The Structural Similarity Index Measure

Symbols

Symbol	Definition	Unit
a	Attenuation	[1]
A_{avg}	Average grayscale value of attenuation	[1]
$A_{\text{avg, norm}}$	Normalized average grayscale value of attenuation	[1]
a_{ij}	Factor approximating the product of projection operator and basis function	[1]
C	Dye concentration	[mol/m^3]
C_{mix}	Coefficient of Mixing	[1]
C_i	Tracer concentration at node i	- [mol/m^3]
D	Impeller diameter	[m]
dI	Change in light intensity	-
dx	Change in position along the x-axis	[m]
$f(x,y)$	Function describing reconstructed image	-
f_j	The value assigned to each cell of reconstruction grid	-

Symbol	Definition	Unit
g_j	Finite set of numbers which describes the picture relative to the chosen basis set	-
H	Tank height	[m]
I	Intensity	[1]
$I(x_i)$	Light intensity at position x_i	-
$I(C)$	Pixel value for a given concentration	[1]
I_0	Pixel value in grayscale corresponding to the dye-free tank/background light intensity	[1]
l	Tank length measured in the direction of the light path	[m]
M, N, O	Resolution of the frames or reconstruction grid	[1]
m, n, o	Pixel or voxel indices	[1]
N	Total number of cells within the ray path	[1]
N_i	Number of cells within the ray path	-
p	Projection pixel value	-
p_i	Observed value along ith ray	-
q_i	Previously calculated value along ith ray	-
R_i	Projection operator along the jth ray	-
Re	Reynolds number	[1]
t	Time	[s]
t_U	Mixing time for a given threshold U	[s]
T	Tank diameter	[m]
U	Given threshold for mixing time calculation	[1]
w_{ij}	Weight assigned to each grid cell - the contribution of the jth cell to the ith ray sum	[1]
α	Molar absorption coefficient	[m^2/mol]
α_b	Brightness adjustment factor	[1]
Θ	Angle	[rad]
δ	Spacing in between the nodes	[m]
ΔI_i	Change in light intensity at node i	-
Δx_i	Change in position at node i	[m]
μ	Dynamic viscosity	[Pa*s]
ρ	Density	[kg/m^3]
τ	Step size parameter	[1]

1

Introduction

Tomography, a potent technique that allows for the imaging of cross-sectional or full volumetric data of an object's internal structure, has significantly revolutionized many scientific fields. Examining the interactions between energy waves and the object reveals details otherwise obscured by the object's exterior. From medicine to archaeology, tomographic reconstruction techniques have provided researchers with a unique window into the hidden aspects of their subjects, fueling countless discoveries and advancements.

By offering non-invasive, detailed, and three-dimensional visualizations, tomography has transformed our approach to understanding complex systems and processes. Instead of relying on destructive methods or educated guesswork to determine what lies beneath an object's surface, we can now accurately map and analyze internal structures and processes.

In this work, we sought to use tomographic reconstruction based on tracer light absorption, hoping to find a cheap, simplistic method for the evaluation of the mixing intensity and its variation within a stirred tank. Obtaining accurately reconstructed in three dimensions tracer data, would allow us to achieve the analytical freedom characteristic of the Computational Fluid Dynamics results. The possibility of direct comparison between the chosen cross-sections, iso-contours and many others could lead to a better link between the experimental data and CFD calculations, opening new ways for simulation validation.

1.1. Context and Relevance

Mixing is a critical process in many industrial applications, particularly in bioreactors. The thoroughness of mixing can directly influence cell growth, product yield, and the overall performance of the bioreactor. Uneven mixing can result in gradients of nutrients and metabolites, affecting the uniformity and predictability of biological reactions. Mixing in bioprocesses also aids in enhancing the mass and heat transfer rates, which are crucial for the efficient functioning of biological systems. The Stirred Tank Bioreactors are one of the biotechnological work-horses, used in around 90% of the industrial bioprocesses, most of the time in a batch mode. [11] Understanding and optimizing the mixing process can contribute to process intensification, leading to cost-effective and environmentally friendly industrial bioprocesses. In fermentation operations, which are one of the most common, for a long time Rushton turbines of a diameter equal to around one-third of the stirring vessel were considered optimal. However, using such turbines can sometimes lead to poor blending in the bulk of the liquid due to flow compartmentalization. [2] Therefore it is essential to attempt to monitor not only the bulk mixing but a spatial distribution of its intensity to provide a homogenous environment that facilitates uniform distribution of substrates, metabolites, and heat.

1.1.1. Traditional mixing measurement

Mixing is often described through only global mixing time - a time needed to reach the desired level of the measured value in the bulk of the tank. Given the tank dimensions, type of impeller and operating conditions the global mixing times, especially in turbulent conditions can be easily predicted by many of the empirical correlations developed through the years of studies. [7]. The traditional single-phase liquid blending measurement mostly relies on point probes to monitor the fluctuations of the modified properties of the bulk due to tracer addition. Some common methods are pH and conductivity monitoring. The biggest flaws of such an approach are the intrusive character of the measurements as the probes can influence the flow patterns within the tank and the dependency of the measured mixing times on the probe's location. Generally, the probes should be placed in the low-intensity mixing zones assuming they are the last to be fully mixed. If too few probes are placed incorrectly the obtained mixing description can be strongly biased. Other approaches are dye addition and dye decolourization. Decolourization is the most commonly used [5] technique. At first, the whole volume of the tank is coloured by adding one chemical such as pH indicator, to then add the second chemical causing the colour removal. The poorly mixed regions are then identified as they are becoming transparent last. In the dye addition method, the spread of the dye is observed, however, the higher concentration zones can occlude the lower ones leading to mistakes in mixing time calculation. By introducing multiple points of view and reconstructing the three-dimensional tracer distribution following work attempt to expand the dye addition method.

2

Theoretical Background

The following chapter is limited to the main concepts introduction and serves as a foundation for the methodology development. A more in-depth description of applied theory can be found in chapter 3.

2.1. Mixing definition

Due to the mixing process being seen as intuitive, multiple definitions exist often dependent on particular industrial processes. The comprehensive definition was developed in [22] and can be later found in for example [21]:

> *Industrial mixing is the control of segregation in unit operations. The instantaneous segregation of a minor species has three dimensions, the intensity of segregation, the scale of segregation, and the rate of change of segregation. The intensity of segregation is the uniformity of concentration of the minor species. The intensity of segregation is defined relative to a fixed volume of investigation and scale of measurement. The scale of segregation is the degree of spatial proximity, or clustering, of members of a population, and is inversely correlated with the degree of spatial dispersion of the minor species. The rate of change of segregation is determined by the exposure or potential for reduction in segregation. The exposure is determined by three factors: the deviation from the minimum state of segregation, the physical contact between populations, and the strength of interaction between members of the populations (either attractive or repulsive).*

Mixing understood as in the above definition has three main objectives [21]:

- Achieving a uniform concentration of species within a mixing domain
- A specified scale of segregation, equivalent to cluster or drop size
- Reaching one or both of the previously mentioned objectives within a certain mixing time

The mixing process takes place at three different spatial scales: macro-, meso- and microscale. Macromixing known also as distributive, is described by the bulk flow of the mixture within the system and corresponds to the elimination of large-scale segregation such as species layers at the surface or bottom of the mixing tank. Mesomixing or dispersive mixing is mostly considered a reduction of the scale of segregation. Micromixing happens at a scale governed by diffusion and chemical reaction rates. [21]

The following study is concentrated on the blending of miscible liquids through mechanical mixing therefore only the first and third objectives of mixing will be investigated. The areas of interest are overall distributive mixing characterized by concentration uniformity and mixing times; and their spatial distribution within a stirred tank.

The final phase of the work presented involves assessing mixing in three dimensions. Therefore, the two-dimensional photographs of the mixing liquids must be mapped to the volume of the mixing tank. To accomplish this, it is essential to first understand the fundamental concepts of tomographic reconstruction, which are presented in the following section.

2.2. Tomographic reconstruction principles & main algorithms

Tomography in its simplest form, transmission tomography, relies upon placing an object between the ray emitter and a detector and measuring the intensity of the ray after passing through. The recorded value corresponds to the ray integral which describes object interaction with the ray along the ray path. A collection of 1D ray integrals from a certain viewing angle is called a projection.[19] Repeating this measurement from multiple points of view results in a set of object projections used to reconstruct the object by back-projecting obtained values using an image-formation model describing the physics of the measurement process. [14] Finding such a model and ray paths fulfilling it is a forward problem as it describes how projections are created through the experimental procedure. The reconstruction is a reverse problem as it attempts to recreate the object geometry from its projections. Three-dimensional object reconstructions are made mostly by stacking multiple cross-sections.

2.2.1. Main algorithms - iterative reconstruction

There are two main approaches to image reconstruction from tomographic data:

- Analytical (e.g. Filtered Back Projection - FBP)
- Iterative (e.g. Algebraic Reconstruction Technique - ART, Simultaneous Algebraic Reconstruction Technique - SART)

Although, the first algorithm used in CT was iterative - in 1970 Gordon published his works on ART [12]; initially due to lack of computation power analytical approach dominated with FBP being the most popular in medical imaging for many years. [34] FBW algorithm is based on the Fourier Slice Theorem stating that: ”The Fourier transform of a parallel projection of an image f(x, y) taken at angle Θ gives a slice of the two-dimensional transform, F(u, u), subtending an angle Θ with the u-axis.” [20] Therefore by measuring infinite projections at different angles, calculating the Fourier Transform of each and adding them, it is possible to recover imaged object by using the inverse 2D Fourier Transform. To limit the imperfections of the measured projections, the projections are multiplied by a filter function such as a Ramp filter or Hamming window. At a large number of viewing angles, FBP algorithms are precise, but in the case of a limited number of projections or projections being non-uniformly distributed over 180 degrees, the transform-based approach is outperformed by the iterative algorithms. [9]

The iterative approach to image reconstruction from projection data is straightforward. First, the image is discretized over a grid. Then the rays’ paths from the emitter to the detector are either assumed (linear in the simplest versions) or calculated using the ray tracing methods. With given ray paths, each ray is represented as a fat line passing the grid with ray integral discretized as a ray sum 2.1

$$\sum_{j=1}^{N} w_{ij} f_j = p_i, \quad i = 1, 2, \cdots, M \tag{2.1}$$

where:

- p_i - observed value along the ith ray
- f_j - the value assigned to each cell
- $w_{i,j}$ - weight assigned to each grid cell - the contribution of the jth cell to the ith ray sum.

Therefore problem can be written as a set of algebraic equations in a matrix form representing the inverse problem:

$$W * F = P \tag{2.2}$$

It is not possible to solve it through simple matrix inversion due to measurement noise and a limited number of views.

In ART first and the simplest of iterative algorithms weight factors take the form of 1 and 0 depending if the centre of the image cell within the ray. The ART can be described as taking the following steps starting with the zero matrix representing the image grid (F)[9]:

- calculate the ray sums along all ray paths in projection in ith angle (forward projection)

- calculate the difference between previous step ray sums and measured data - error
- distribute the error evenly along the ray paths (back projection)
- repeat the previous steps for all the viewing angles

The correction to the ith cell can be written as:

$$\Delta f_j^{(i)} = \frac{p_i - q_i}{N_i} \tag{2.3}$$

where:

- p_i - observed value along the ith ray
- q_i - previously calculated value along the ith ray
- N_i - number of cells within the ray path

There is a version of ART based on multiplication rather than addition in which the multiplicative update step instead of the additive update step is used. The correction term is calculated by dividing the projection data by the forward projection of the current estimate.

In SIRT - Simultaneous Iterative Reconstructive Technique) the correction to the ith cell is calculated the same way as in ART 2.3, although the cell values are actualized only at the end of the iteration and by the average of all the corrections calculated for each ray. In a matrix form, it can be written as [3]:

$$\boldsymbol{x}^{\delta(k+1)} = \boldsymbol{x}^{\delta(k)} + \tau \mathsf{A}^{\mathsf{T}} \mathsf{R}_2^{-2} \left(\boldsymbol{y}^{\delta} - \mathsf{A}\boldsymbol{x}^{\delta(k)} \right) \tag{2.4}$$

where:

- $\boldsymbol{x}^{\delta(k)}$: The estimate of the volume at iteration k. This is a vector of length V.
- τ: A step size parameter.
- A: The matrix representing the relationship between the projection and the reconstructed object-ray paths.
- R_2^2: A diagonal matrix with the squared L2 norms of the rows of A.
- y^{δ}: projection vector

The SART algorithm is quite different. Rather than discretizing the image into a pixel-based grid, bilinear basis functions are used to model forward projection steps in a continuous way resulting in 2.5:

$$p_i = R_i f(x, y) \approx R_i \hat{f}(x, y) = \sum_{j=1}^{N} g_j R_i b_j(x, y) = \sum_{j=1}^{N} g_j a_{ij} \tag{2.5}$$

where:

- R_j - projection operator along the jth ray
- $f(x, y)$ - function describing reconstructed image
- $b_i(x, y)$ - chosen basis function
- g_i - finite set of numbers which describes the picture relative to the chosen basis set
- a_{ij} - factor approximating the product of projection operator and basis function

To approximate a_{ij} a sample lattice over the reconstruction area is imposed with equidistant (with δs in between) points. Then a_{ij} is approximated by adding the weights of neighbouring sample points. The pixel update equation can then be written as 2.6

$$g_j^{(k+1)} = g_j^{(k)} + \frac{\sum_i \left[a_{ij} \frac{p_i - \vec{a}_i^T \vec{g}^{(k)}}{\sum_{j=1}^{N} a_{ij}} \right]}{\sum_i a_{ij}} \tag{2.6}$$

or in a matrix representation [3]:

$$\boldsymbol{x}^{\delta(k+1)} = \boldsymbol{x}^{\delta(k)} + \tau \mathsf{C}_1^{-1} \, \mathsf{A}^{\mathsf{T}} \mathsf{R}_1^{-1} \left(\boldsymbol{y}^{\delta} - \mathsf{A}\boldsymbol{x}^{\delta(k)} \right) \tag{2.7}$$

where:

- $\boldsymbol{x}^{\delta(k)}$: The estimate of the volume at iteration k. This is a vector of length V.
- τ: A step size parameter.
- A: The matrix representing the relationship between the projection and the reconstructed object-ray paths.
- R$_1$: A diagonal matrix with the row sums of A.
- C$_1$: A diagonal matrix with the column sums of A.
- y^{δ}: projection vector

The formulation of the method is finalised by modifying the back projection step by replacing the distribution according to the values of a_{ij} with a weighted version using Hamming window to give more influence to the central parts of the rays. In [35] researchers combined the SART algorithm with Adaptive Genetic Algorithm to further improve the reconstruction achieving promising results.

An alternative approach was shown in [14] in so-called Stochastic Tomography in which authors use the random walk to evaluate the increase in residuals and minimize the objective function with several added regularizers, outperforming the SART algorithm in the test of Shepp-Logan phantom. Also, recently in X-ray tomography, the use of neural networks is explored [30]. The use for the mixing liquids reconstruction was not found.

2.3. Research Definition

The goal of the project was to create from scratch both an experimental setup and software implementation of the tomographic reconstruction techniques in an attempt to quantify mixing in a stirred tank using a maximum of three viewpoints.

To achieve said objective following research questions had to be answered:

- What are the obstacles in three-dimensional dynamic tracer distribution reconstruction?
- How the experimental equipment should be constructed to obtain the best possible data from three cameras recording the back-lit stirred tank?
- How to process raw images to isolate the ray-dye interaction?
- How to obtain relevant mixing information from projections and reconstructed volumetric data?

2.3.1. Pre-eliminary literature study

During the preliminary research, very few publications were found showing attempts to evaluate mixing times using light-based tomographic methods, leaving plenty of room for innovation and the development of new techniques. Most of the reconstruction algorithms were developed for use in medical imaging using X-Ray tomography with few attempts found to use it for visualising mixing or flow [17], [25]. Parallels between X-Ray tomography and planned experimental setup can be drawn, and as the most described technique in the field, it served as the main source of inspiration.

Most of the publications found in which researchers describe utilising visible light describe either mixing time measurements without volume reconstruction [4, 8, 23] or volume reconstruction of light emitting objects such as flames [26, 13, 31] or fluorescent ink [14] injected into the vessel. Additionally, previously mentioned articles about volume reconstruction mostly use multiple camera setups with a minimum of 5 in proof of concept setup and use 15 cameras in most of their experiments in [14]. Description of experiments in [10] seems to be the closest to the planned setup. The author used two syringe pumps to draw fluids A and B, combine them with a T-junction, and convey them through a measurement section for 3D imaging using a camera/lighting arrangement shown in the fig 2.1 taken from [10]

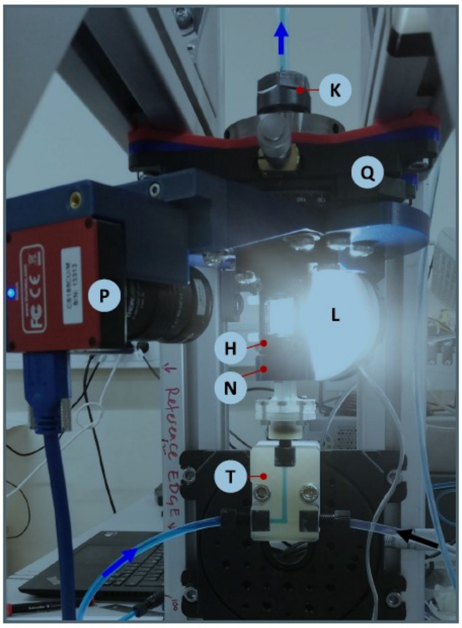

Fig. 2 Annotated photo of the experimental setup: *T* component-fluid junction, *N* support tube, *H* light-shield, *L* light-source, *P* camera, *Q* micropositioner, *K* tube-clamp

Figure 2.1: Experimental setup with rotating camera

The camera was mounted on a micropositioner to rotate and view the fluid tube from 13 viewing angles, with a shield tube and radial seals to reduce environmental lighting alterations. To reconstruct the images simple least squares approach was used resulting in the estimated component fluid distribution in cross-section.

Another approach is to use a plenoptic camera which captures additional information about light direction and angle by using an array of microlenses placed in front of the image sensor, providing spatial-angular data called the light field. This allows for the reconstruction of the object volume using light field deconvolution. [6]

In [24] and [36] Electrical Resistance Tomography and Electrical Capacitance Tomography are shown as leading tomographic techniques used in the industry for mixing and multiphase flow measurement. The array of electrodes is placed around the periphery of the reactor and a small alternating current is passed through these electrodes. The resulting potential difference (or voltage) is measured. By applying a known current and measuring the resulting voltage, the electrical resistance, and hence the conductivity/tracer distribution within the system, can be inferred. Although measuring principles are vastly different some ideas regarding image reconstruction might later be proven useful.

A thorough description of forward and inverse problems of optical tomography used in biomedical imaging of tissue can be found in [3]. The mathematical formulation of the forward problem is widely discussed including the Maxwell equations, radiative transport equation and diffusion theory. Due to the extremely dynamic nature of mixing and tissue being a much more scattering medium than water, it was concluded that a simplistic approach to the forward problem will be taken as described in chapter 3. No bubbles or other highly scattering objects inclusion is planned in the experiments. Moreover, the reflections as well as light refraction can be nullified, by careful design of the experimental setup. Thus, absorption is assumed to be solely responsible for ray intensity decrease after passing through the vessel and the Lambert-Beer law will be used. The project image acquisition is limited to only three points of view which means the problem is heavily underdetermined. Therefore the leading idea behind the use of a simplistic forward model - the discretization of Lambert-Beer law, can help in incorporating the filtering or refining techniques as the causal link between the recorded phenomena, obtained projections and reconstructed volume is easy to understand.

In order to establish the required data processing workflow and comprehend the limitations of using only three viewing angles, the initial decision was to utilize synthetic mixing data, free of unexpected disturbances.

3

Methodology

The following chapter guides the reader through the process of tomographic assessment of mixing, starting with setup construction and data acquisition to image pre- and post-processing. During the methodology development simplicity of the applied solutions was desired to achieve a clear overview and control over the outcome in a multistep workflow. All of the described procedures were implemented in Python using mostly Numpy and OpenCV libraries for image manipulation; matplotlib.pyplot for the visualization tasks, os for Generic Operating System Services and occasional usage of Scipy and Pandas for optimization and data analysis. Code can be accessed upon request submitted to the project supervisor (c.haringa@tudelft.nl)

3.1. Synthetic data - framework development

Using synthetic data to create a digital sandbox for reconstruction trials allowed us to identify some of the obstacles in reconstruction and freely test ideas in a perfect, noise-free environment. Development started by extracting the tracer concentration data from the simulation results supplied by the supervisor. Mixing of a tracer in a square tank with a single Rushton turbine in a centre was simulated in M-STAR CFD, using Large Eddy Simulations (LES) to create dynamic, high-resolution tracer concentration fields. The concentration data were extracted to separate CSV files at each timestep using ParaView (an open-source post-processing visualization engine) to allow for easy array manipulation in Numpy. The simulation lattices used equidistant cubic node spacing, thus the CSV files can be read into a cubic array of a shape corresponding to the number of nodes in each axis. Indexes of such an array corresponding to the three-dimensional Cartesian coordinate system result in intuitive data representation. Next assuming a perfect pencil beam of light aligned with each of the system axis (x,y,z) passing through the discretized concentration field and concentration-independent extinction coefficient (α), the discrete Lambert-Beer equation 3.3 over each pixel array is integrated to create projections, simplifying the forward problem. The use of the Lambert-Beer equation and the assumption of the pencil beam is equivalent to assuming neither light diffraction nor scattering is present.

$$\frac{dI}{dx} = \alpha * C \tag{3.1}$$

discretising eq.3.1 along example ray in x-direction on nodes from i to N:

$$\frac{I(x_i) - I(x_{i+1})}{x_i - x_{i+1}} = \frac{\Delta I_i}{\Delta x_i} = \alpha * C_i \tag{3.2}$$

summing over the ray path to approximate the ray integral with an equidistant spacing of the nodes $\Delta x_i = \delta$:

$$p = \sum_{i=1}^{N} \Delta I_i = \sum_{i=1}^{N} (\alpha * C_i * \delta) \tag{3.3}$$

Assuming both unit thickness $\delta = 1$ and unit extinction coefficient ($\alpha = 1$) calculating ray integrals simplify to summing the concentration values along the axis for each projection pixel. As a final step in each projection, all the pixel values are min-max normalised to the 8-bit grayscale (pixels take the value between 0 and 255)

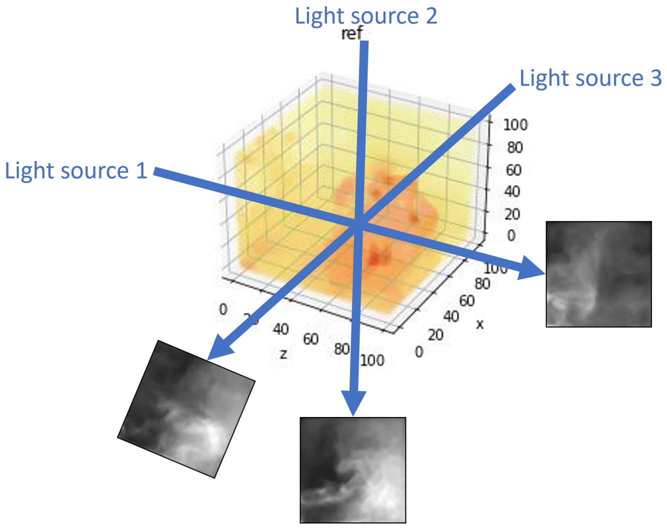

Figure 3.1: Synthetic frames creation

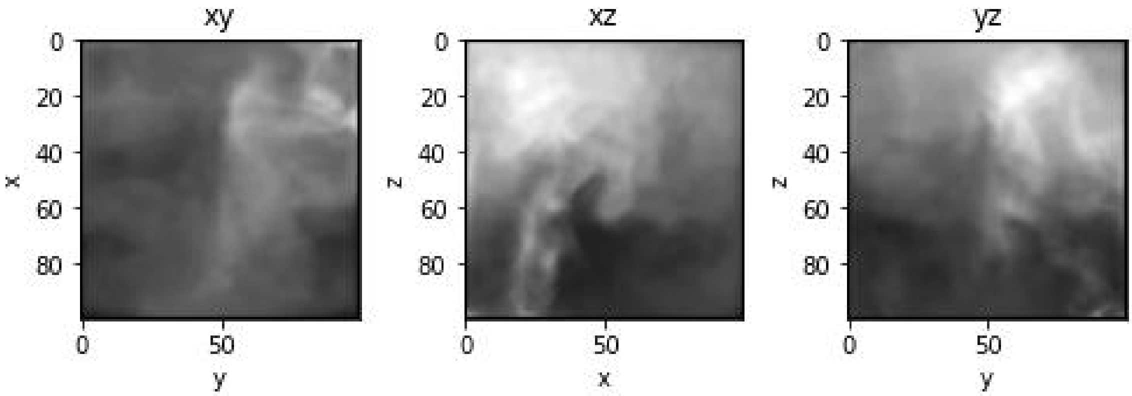

Figure 3.2: Example synthetic frames at 67th timestep

The concentration data were collected with a timestep of 0.1003 [s]. Basing on the synthetic frames both reconstruction and post-processing routine was later developed as described in sections 3.4, 3.5.

3.2. Experimental data acquisition

To collect real-life data and gain the insight necessary to design the triple-view tomographic table a single camera was used to obtain footage of dye mixing with a Rushton turbine in a backlit beaker (fig. 3.3). Single-camera and reconstruction trials using synthetic data resulted in the formulation of the following design ideas:

- Tank side facing the camera should be flat to avoid distortion. If the stirred tank has curved walls it should be placed in the polygonal tank filled with water to match the refractive index similar to the setup in [8]

- LED panels should be placed close to the tank to efficiently use their area of illumination.
- To best replicate the conditions of a pencil beam, cameras should be equipped with optics that have the smallest available aperture. Additionally, they should be positioned at a sufficient distance to ensure collimation. The cameras should be placed at a distance that not only ensures collimation but also allows only the face of the tank to be captured, thereby eliminating perspective effects and simulating the assumption of the linear ray path. For the used Basler camera equipped with FLCC251 2M lens 85 cm was enough.
- Proper alignment of the cameras and the LED panels should result in only one-panel visibility per viewing point
- To simplify the forward problem as in the case of the synthetic data and circumvent the challenge of correctly angling the LED panels orthogonal to each camera's viewing axis, viewing points should be positioned along each axis of the tank. This arrangement would involve one point at the bottom and two points on the sides, each separated by a 90-degree angle. Due to the tank being surrounded by LED panels, they serve the additional function of shielding the tank from external light.
- Using the bottom camera creates a challenge for tank support as the bottom needs to be transparent and accessible. Additionally, the shaft of the mixer needs to pass through the top LED panel
- The dye used as a tracer should be concentrated and used in low volume for its injection time to be as short as possible
- All of the elements within the imaging zone should be black to avoid reflections

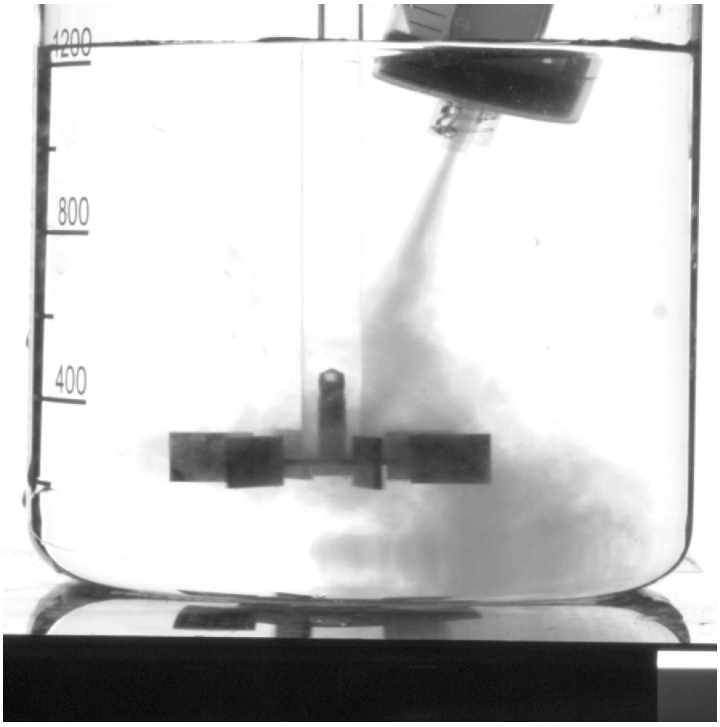

Figure 3.3: Single Basler camera trial

3.2.1. Equipment description

Having in mind conclusions from the single camera trials a tomography table was first designed in AutoCAD Inventor as seen in Fig. 3.4

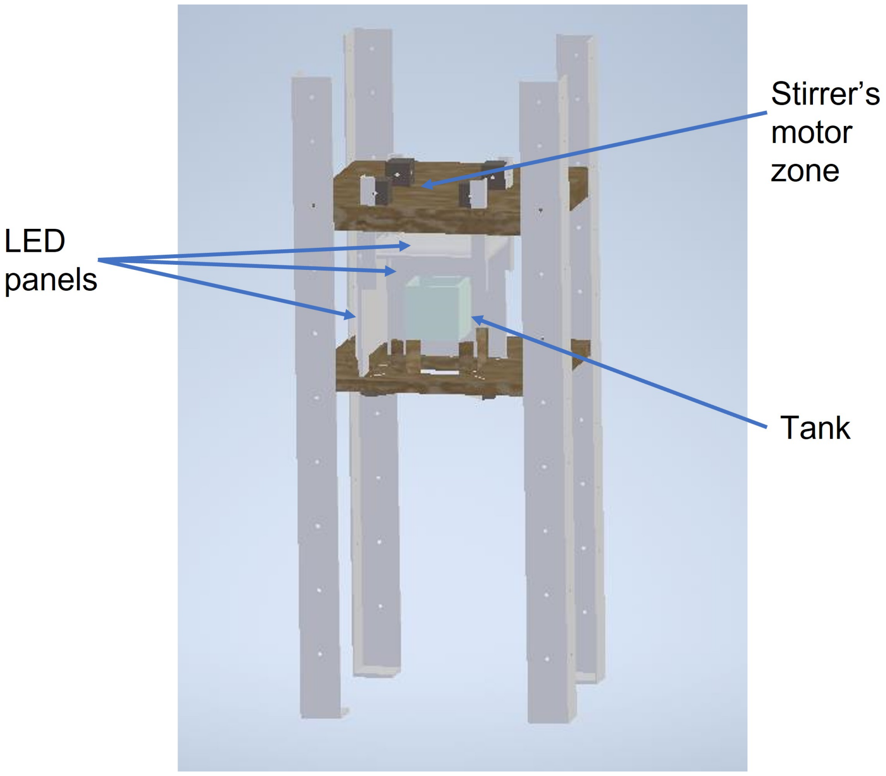

Figure 3.4: Setup visualization

The legs were made out of 40x40x2mm 2m long aluminium corner profiles. The legs length allows placing the tank far enough from the bottom camera to fulfil the design assumptions. Both the tabletop and stirrer's shelf are made with 18 mm thick plywood. The tank is supported in the corners by four wooden legs which can be adjusted depending on the tank's dimensions. All the LED panel mounts can be moved along the guiding tracks allowing for the panel-tank distance adjustment.

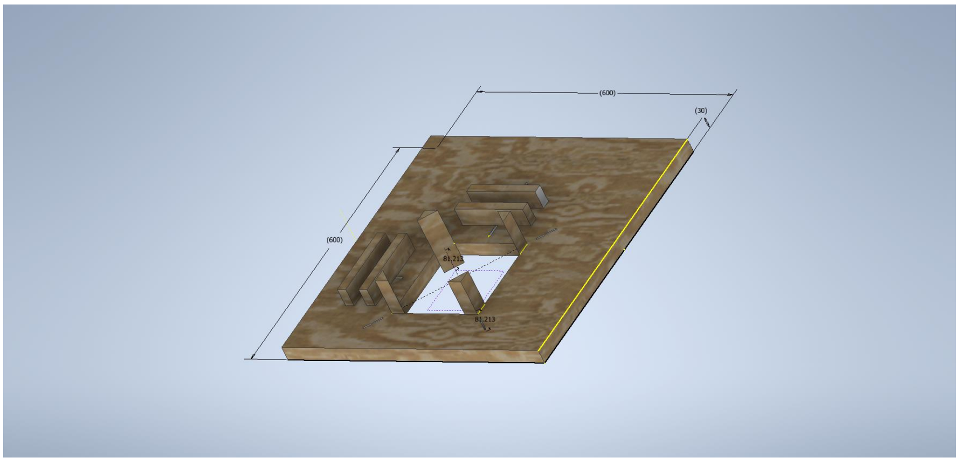

Figure 3.5: Tabletop allowing bottom view

The experimental setup was designed for three cameras, similar to the one used in single-camera experiments. However, due to the unavailability of enough Basler cameras and the proof-of-concept nature of the work, we resorted to using three inexpensive webcams to capture the frames. This substitution of the widely recognized in computer vision community Basler cameras and specific optics with webcams resulted not only in a decrease in image quality but also in a breach of some of the assumptions and design concepts outlined at the start of section 3.2. The imaging issues arising from this change are further elaborated in subsection 3.2.2. The final version of an experimental setup can be seen in fig 3.6 and characteristic parameters can be found in tab. 3.1

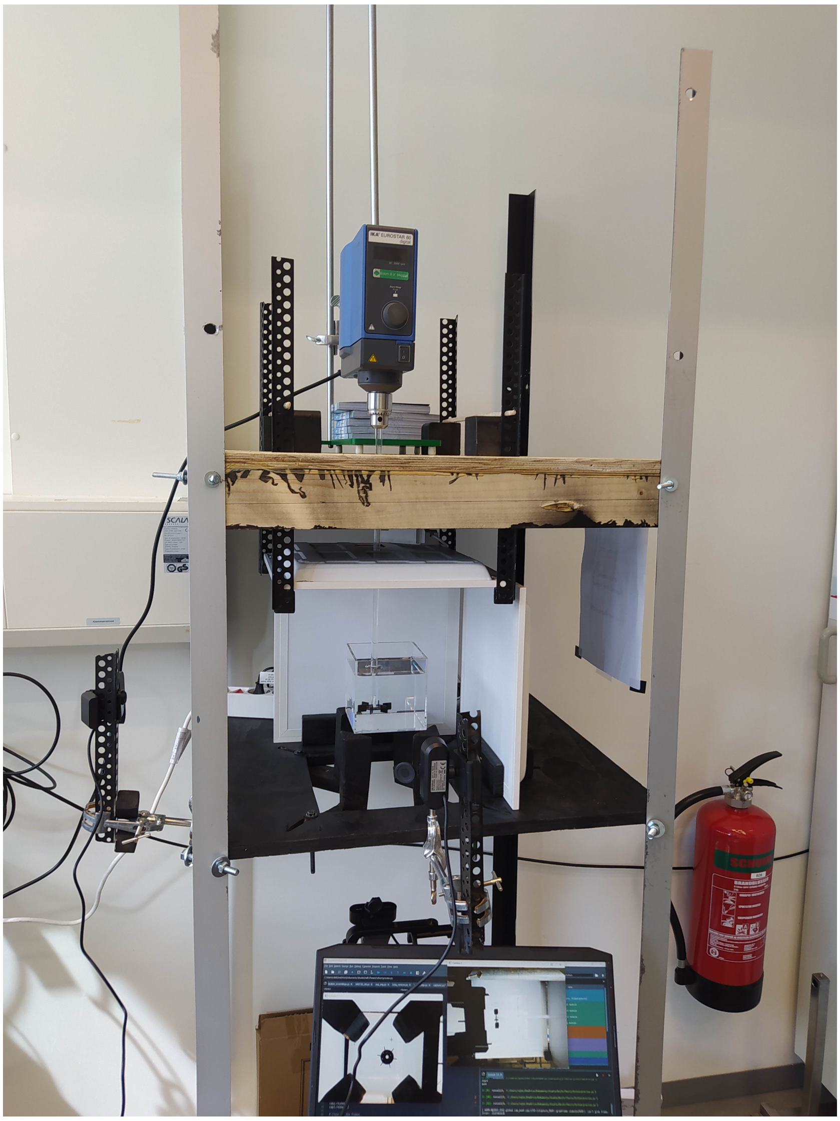

Figure 3.6: Final experimental setup

Equipment type	Name	Parameters	Value	Unit
Impeller	Rushton turbine	D (blade tip diameter)	6	[cm]
		d (plate diameter)	4	[cm]
		l	1	[cm]
		Number of blades	6	[1]
Tank	Acrylic glass cube	Side length	13	[cm]
Camera	Nor-Tec webcam	Quantity	3	[1]
		FPS	25	[1/s]
		Resolution	480x640	[pixels]
		Aperture	?	
		distance to tank side	30	[cm]
Light Source	Square LED panels	Quantity	3	[cm]
		Side length	30	[cm]
		Temperature	4000	[K]
		Wattage	20	[Watt]
		[HTML]RGBA(155, 155, 155, 0.05)Light output	2000	[Lumen]
		Light angle	120	[°]
Tracer	Sugarflair Liquid Food Coloring - Super Black			

Table 3.1: Equipment characteristic parameters

3.2.2. Limitations

The final setup utilising webcams has the following limitations:

- Fixed unknown aperture is not small enough to assume good collimation
- Automatic white balance prevents placing the camera at a distance long enough to achieve collimation and eliminate perspective effects. The maximum distance from the tank providing stable white balance in a range allowing to image the dye is 30 cm instead of the planned 85 cm. Therefore reflections on tank walls and light scattering on the tank edges are significant.
- Fixed 25 FPS lowers the maximum impeller RPM to 40 to avoid motion blur and the impeller moving too much in between frames. Operating at 40 RPMs which is the lowest possible speed of a motor leads to unstable rotation speed.
- Using hardware trigger for cameras synchronization is no longer possible
- Tank size is limited by 2 factors tabletop opening (20x20 cm) and LED panel dimensions (30x30 cm)
- Impeller size occlude certain areas within the tank. The most influential is plate diameter it is beneficial to use the smallest possible.

Due to webcams not supporting hardware triggering, it was necessary to implement a software trigger giving the best possible synchronization. A short script was written in which threading is used to capture video from multiple cameras simultaneously. Each camera has its own thread, and each thread continuously captures frames from its associated camera. This allows the script to capture video from all cameras at the same time, rather than having to capture from each camera in sequence. After the initialization of the threads, a signal to start recording is given by pressing the space on the keyboard passing the argument initializing the frame saving to each of the threads simultaneously.

3.3. Image pre-processing pipeline

Acquired raw data vary greatly from the synthetic one used for framework development described in section 3.1. Moreover, the final experimental setup differs from the ideal image acquisition design as described in section 3.2. Therefore it was necessary to create an extensive pre-processing routine that would minimize the differences in experimental footage of mixing liquids and projections created from simulation data in order to increase the chance of successful reconstruction.

(a) Raw webcam frame

(b) Pre-processed webcam frame

Figure 3.7: Raw data vs Pre-processing

The workflow implemented in Python using mostly OpenCV and Numpy libraries is illustrated on the following page (fig. 3.8 and explained in detail in the individual subsections.

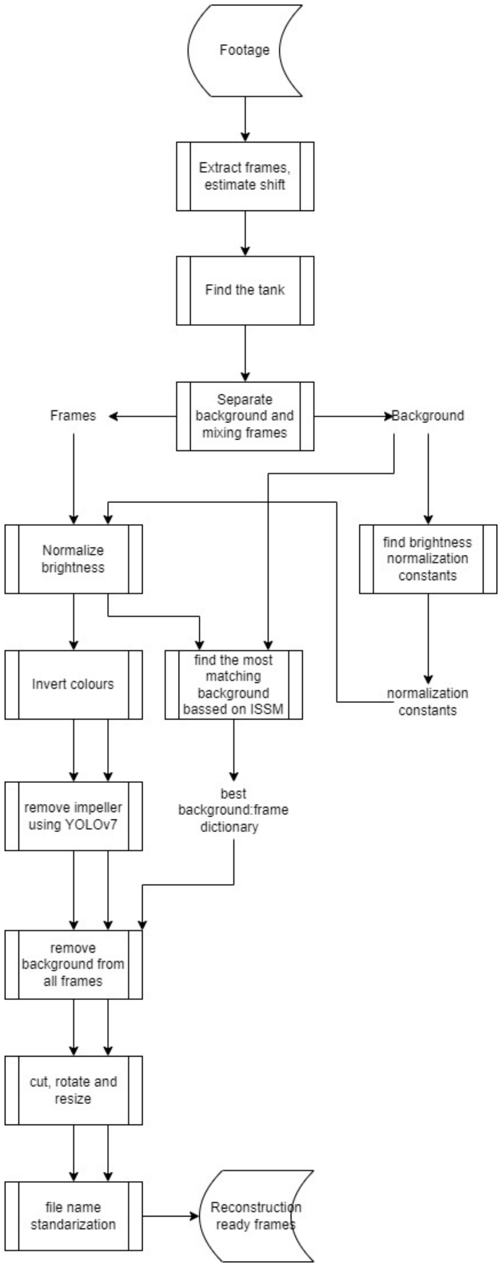

Figure 3.8: Image pre-processing workflow

3.3.1. Manual steps

The first step after successfully recording an experiment is to divide obtained footage into individual grey-scale frames - cheap cameras do not have an option for individual frame acquisition. As explained in 3.2.2 the cameras were synchronized with software rather than the hardware trigger. To validate synchronization the moment of turning the illumination is used. If necessary the frames are renamed using a simple script to shift the frames and achieve proper synchronization. The next task is to find the location of the tank in each view and save the pixel indexes of interest for further use. Each recording consists of a couple of seconds of pure background at the beginning therefore it is necessary to identify the moment of tracer injection and separate background frames from mixing frames.

3.3.2. Brightness normalization

In an ideal situation where all light sources, detectors and their settings are identical, placed at exactly the same distance from the recorded symmetrical tank (as per Lambert-Beer law absorbance is proportional to the light path length through the medium) the sensor response should be uniform before the tracer injection. In practice, none of those assumptions are strictly fulfilled and approximated at best. Reconstruction in later steps relies on uniform input from all the views therefore it is essential to normalize and establish a pixel intensity baseline. Assuming the normal distribution of noise, the pixel means within a given time are calculated from the background frames, creating the most probable intensity distribution of the background. A region of pure background without any wall or impeller present is chosen for all viewing points. The next step is to calculate the average pixel value of chosen region per view $I_{avg,i}$

$$I_{\text{avg},i} = \frac{1}{N * M} \sum_{m=1}^{M} \sum_{n=1}^{N} (I(n,m,i) - I(n,m,i)) \tag{3.4}$$

Then the adjustment factor α_b is calculated as a difference between $max(I_{avg}, i)$ and $I_{\text{avg},i}$. to normalize the frames to the brightest one, as after the colour inversion, this leads to the lowest noise.

$$\alpha_b = max(I_{avg}, i) - I_{\text{avg},i} \tag{3.5}$$

Images are adjusted by re-scaling the image brightness according to the adjustment factors. As a final step, the α_b are applied to all of the acquired frames resulting in a uniform brightness baseline. The whole procedure is illustrated in Fig. 3.9

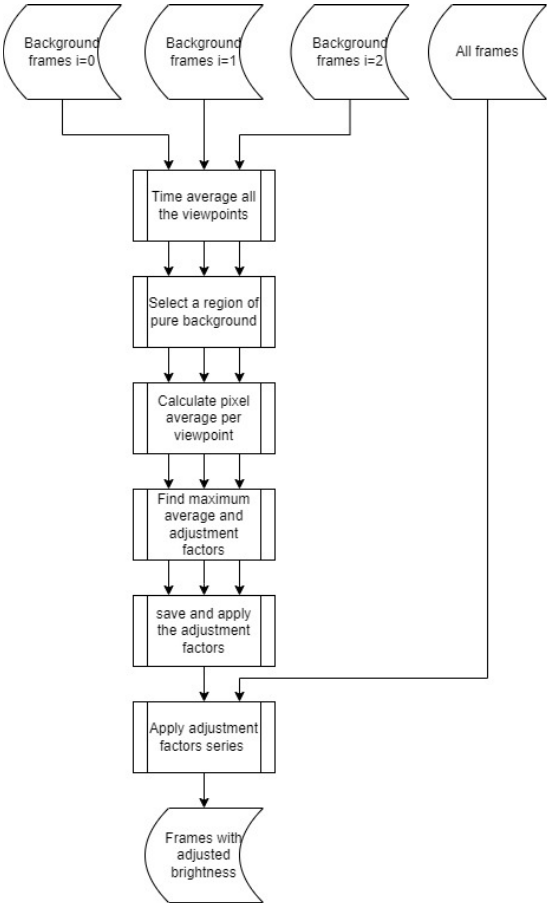

Figure 3.9: Brightness normalization workflow

3.3.3. Background removal

One of the final steps is the background removal. The reconstruction is the easiest if only the tracer representation takes non-zero values in the input images. With a perfectly monotonic background, this step would consist only of subtracting the single value corresponding to the initial light intensity passing through a tank without a tracer. Unfortunately, in a real set-up, there is some non-uniformity within the picture due to for example LED panel construction defects such as imperfect light diffusive layer. Additionally, the impeller is removed together with the background if used with a high enough frame rate for the experiment capture. The applied method matches the background frame with the most similar mixing frame based on image similarity metrics of uncut, raw grey-scale frames. Three different similarity metrics were implemented from scratch and tested:

- Root Mean Square Error [RMSE]
- Mean Structural Similarity Index Measure [MSSIM]
- Shannon–Histogram Similarity [EHS]

as well as their combinations and when applied to frame fragments.
RMSE is the simplest metric in which the point-wise difference between two images is taken, squared, averaged per pixel and finally quadratic root is taken. As it was not giving promising results it was discarded very early.

SSIM is a little bit more complicated statics-based approach and its basic version was implemented using the definitions in [33]. As the name suggests it is focused on structural similarity of the images. First, the mean of each of compared images is calculated using a Gaussian blur. A standard deviation of 1.5 and a kernel size of 11x11 are used, which are common parameters for SSIM as described in [33]. Then the square of the mean and the product of the means are calculated. The variance for each image and the covariance are calculated. This is done by blurring the square of the images and then subtracting the square of the blurred images. The SSIM map is calculated using 3.6:

$$\text{SSIM}(\mathbf{x}, \mathbf{y}) = \frac{(2\mu_x\mu_y + C_1)(2\sigma_{xy} + C_2)}{(\mu_x^2 + \mu_y^2 + C_1)(\sigma_x^2 + \sigma_y^2 + C_2)} \tag{3.6}$$

which takes into account the brightness (mean), contrast (variance), and structure (covariance) of the images, all evaluated locally. Parameters C_1 and C_2 were set as 6.5025 and 8.5225 respectively, which is standard for 8-bit greyscale. Finally the $\text{SSIM}(\mathbf{x}, \mathbf{y})$ is averaged over all pixels to return a single value describing the similarity.

EHS is a metric with roots in the information theory utilising the concept of Shannon entropy as described in [1]. Its simple implementation essentially compares the histograms of two images and their joint histogram. First, a histogram of each image with 256 bins corresponding to the grayscale values is created and normalized to represent Probability Mass Function. Then joint PMF is calculated in the same way by first storing the 2 images in a flattened array and creating its normalised histogram. Next, Shannon entropy as defined in [1] for each of obtained PMFs is calculated.

$$E_s(x) = -\sum_{i=1}^{n} p(x_i) \log_2 [p(x_i)] \tag{3.7}$$

where x_i is pixel value and $p(x_i)$ is PMF value for given x_i. Finally, the mutual information is calculated as the sum of the entropies of the two images minus the joint entropy and then divided by the average of the entropies of the two images to obtain the EHS score. Calculating EHS and SSIM is part of the hybrid metric called ISSM [1], but due to sufficient performance of SHS, ISSM was not fully implemented.

The testing set for metric evaluation consists of 59 images representing different stages of mixing pooled out of the 180 FPS recording of a tracer being mixed in a beaker with 40 rotations per minute. The 300 background frames were obtained from the same recording before tracer addition. The result of background subtraction of the most similar background found per test case was inspected for artefact creation as it was evident SHS performed the best and further detailed analysis was not necessary.

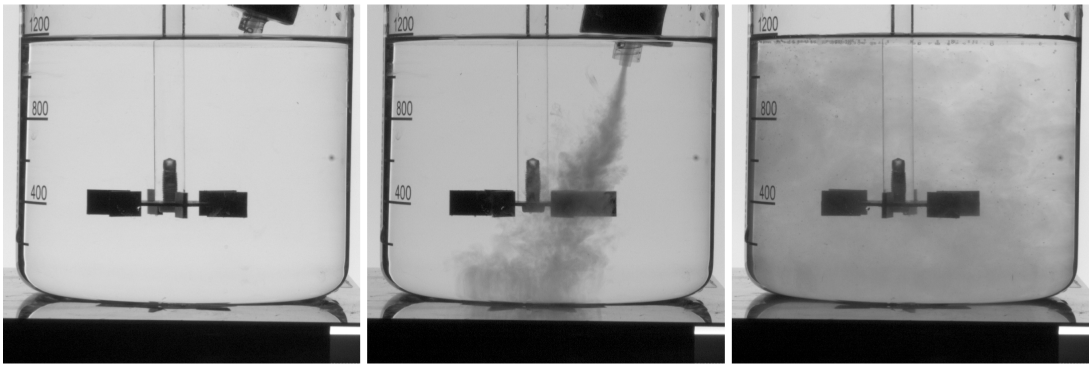

Figure 3.10: Example test photos

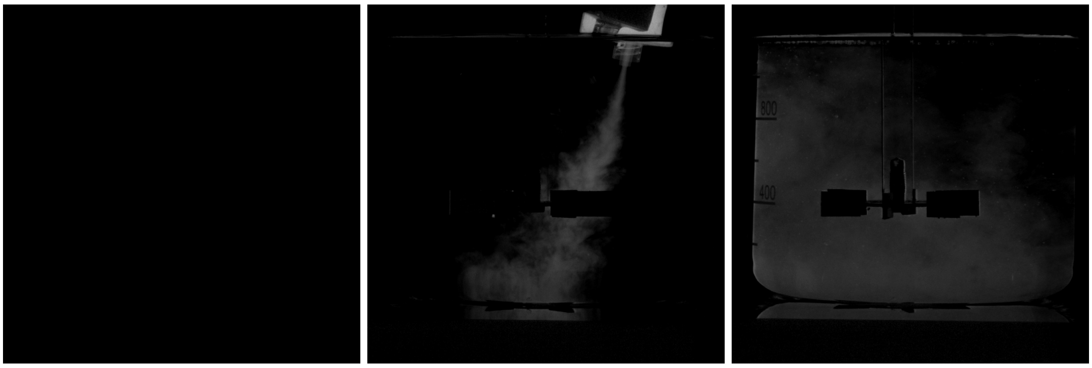

Figure 3.11: Example of MSSIM background removal

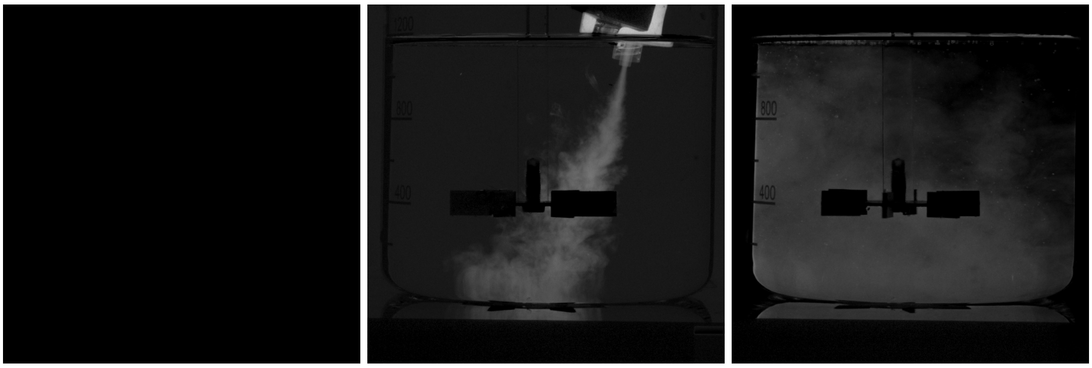

Figure 3.12: Example of SHS background removal

3.3.4. Use of YOLOv7

The used Rushton turbine was black therefore complete light absorption of interacting rays is assumed. The tracer was also black, therefore numerically the impeller is indistinguishable from the regions of maximum tracer concentration. Combined with strong ghosting resulting from limited projection angles it could completely dominate the reconstruction leading to the loss of tracer contribution to the voxels attenuation. The previously described background removal procedure (subsection 3.3.3) efficiently removes the impeller when using a high frame rate over a sufficient time span of background imaging. However, with lower FPS and unstable rotor speed, the impeller's position might not perfectly align with the background frame within an acceptable time window. To improve the reconstruction a method for impeller detection and elimination from the frames was developed. You Only Look Once version 7 (YOLOv7) is a state-of-the-art neural-network model for object detection described in detail in [32] trained on Microsoft COCO dataset (Common Objects in Context - one of the most popular large-scale labelled image datasets available for public use [27]). YOLOv7 is publicly available on GitHub, the version of the model used was based on the state of the main branch in the official GitHub repository (https://github.com/WongKinYiu/yolov7) as of May 2023. The repository is actively maintained with regular contributions from both the original authors of the paper and the broader community. The COCO dataset does not include any pictures of impellers hence 254 frames were hand-annotated using the Roboflow platform [29]. Chosen frames include images from all experimental viewpoints with a combination of the following characteristics:

- raw grayscale
- inverted colours
- early beaker trials as a tank
- square tank
- various occlusion by the dye
- clear background

The platform also allows for easy dataset augmentation (creating a modified version of existing labelled pictures for more robust detection). The following augmentation techniques were used to account for different impeller positions, tilted cameras in the setup, motion blur, and incorrect focus:

- Horizontal flip
- Rotation between -15° and +15°
- Gaussian blur - up to a 2.5-pixel radius
- Random noise to 5% of the pixels

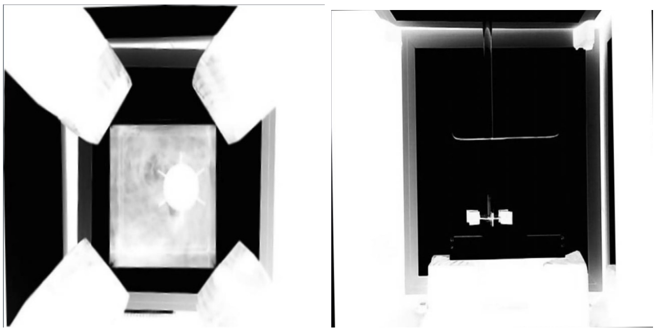

(a) Bottom view, late mixing stages **(b)** Side view, clear background

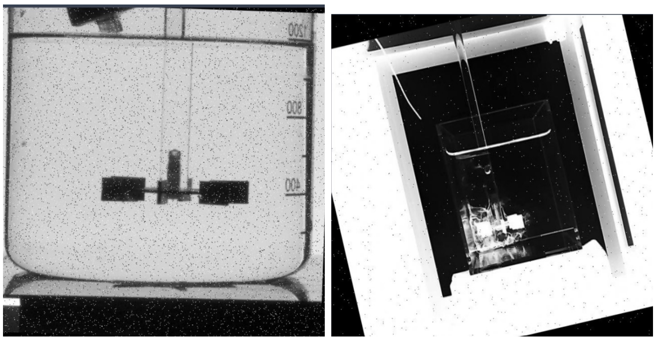

(c) Tilted beaker, raw grayscale with noise **(d)** Heavily tilted side view at early mixing stage

Figure 3.13: Examples of images within created dataset

The created dataset contains 608 images split into training, validation and test sets (531/49/28 frames). The next step is retraining the model to fine-tune it into impeller recognition. The training was done in 9 epochs on Tesla T4 NVIDIA-SMI 525.85.12 in the Google Colab environment due to the readily accessible high-performance GPUs, significantly accelerating the process. After each epoch of training, a number of metrics are recorded. These include 'Box' and 'Mask' values for precision (P), recall (R), mean Average Precision with Intersection over Union (IoU) of 50% (mAP50), and mean

Average Precision with IoU from 50% to 95% (mAP50-95). Precision is the ratio of correctly predicted instances to the total instances predicted. The recall is the ratio of correctly predicted instances to the total actual instances. Mean Average Precision is the average of the precision values at different recall levels. Initially, the precision, recall, and mAP50 values were quite low. This is normal as the model was still learning to recognize the objects. By the 9th (final) epoch, the precision for Box and Mask predictions had improved to around 0.96 and 0.978 respectively, the recall was at 0.94 and 0.96 respectively, and mAP50 values had risen to 0.955 and 0.958. These high values suggest that the model was doing a very good job of recognizing and locating the objects in the images. During the validation step (after the training), the final model achieved even higher precision and recall values, further demonstrating its strong performance. The model required about 14 GB of GPU memory for the training process, and the whole process took about 6 minutes to complete. On the test set, the model continued to perform strongly detecting correctly impellers in all of the images proving to be a viable step of image pre-processing for the reconstruction.

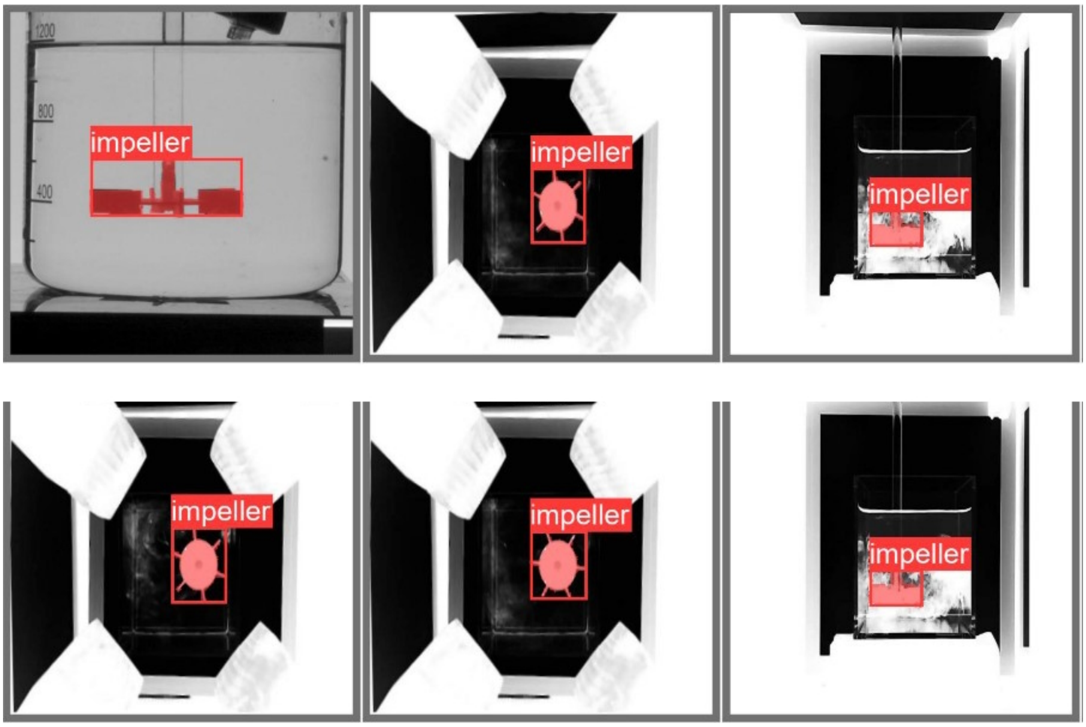

Figure 3.14: YOLOv7 detection examples

Having a dataset and detection model ready it is necessary to adjust the prediction script shifting its purpose from annotating detected objects to removing them by replacing all the detected pixels with zeroes (black in the grayscale). To assure that the impeller is fully removed a dilation operation with (9,9) kernel is applied on the pixels of the detected object. Dilation is a morphological operation in image processing in which a small matrix is used to enlarge an object by moving the centre of a matrix through the object's pixels and copying the value from the centre to all pixels within the matrix index range. Used kernel size results in adding 4 black pixels around the object boundaries. Example final results can be found in Fig. 3.15

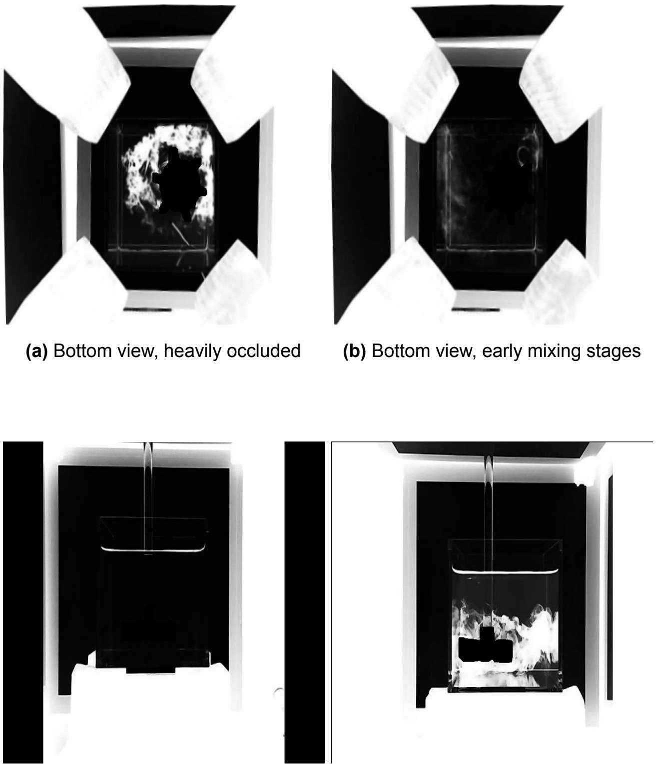
(a) Bottom view, heavily occluded **(b)** Bottom view, early mixing stages

(c) Side view, background **(d)** Side view, heavily occluded

Figure 3.15: Examples of impeller removal using YOLOv7

3.4. Reconstruction

A reconstruction using a limited number of viewpoints suffers from significant ghosting - back-projecting the data behind the actual location of the object.

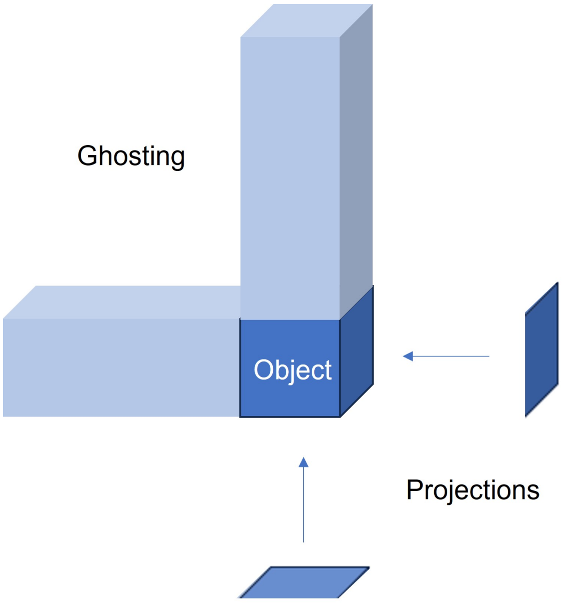

Figure 3.16: Ghosting in reconstruction

Increasing the number of viewing angles in tomography improves the information describing the object and mitigates ghosting. This effect can be further minimized by integrating priors and regularizers into the reconstruction process. In the case of mixing liquids, the structures are of extremely complex geometry, constantly deforming and moving in the reconstruction space, leading to unpredictable ghosting artefacts. Found attempts of tomographic reconstruction of deforming objects, consider mostly solid objects of constant underlying core geometry with limited movement [18]. Due to the ghosting and dye spreading similarity, regularization is difficult as attempts of limiting the creation of the artefacts can lead to limiting the tracer spread. Additionally, the reconstruction is complicated by the imaging noise and the discrepancy between forward model assumptions and experimental conditions. Due to only three viewing angles to optimize the use of available information regarding the object geometry, reconstruction was performed on a total frame sequence instead of individual frames. If FPS is high enough, the core geometry should remain unchanged in-between time steps. This approach confines the reconstruction to volume deformation and offers two initial geometry candidates: a sphere at the dye injection site at the start, or the tank geometry at the end when the tracer fills the entire volume. The simplified SART algorithm was chosen as a base for the reconstruction process implementation due to its straightforward nature, resulting in the observable process of artefact creation and ease of the addition of the prior.

3.4.1. Reconstruction algorithm implementation

Although SART can be formulated simply as in eq. 2.7 it is desirable to avoid explicitly writing such a system to implement the algorithm as a projection matrix A (especially in the case of 3D reconstruction) is a large sparse matrix specific for each angle. [18] Naive implementation using projections of a shape NxM from 3 different angles for a volume discretized as a matrix of a shape XxYxZ results in the projection matrix A of a size $3 * N * M * X * Y * Z$ as it relates each ray contribution to each voxel. Using the assumptions and simplifications described in section 3.1 writing the linear system is avoided, replaced by the steps shown in the Fig. 3.17 reducing the problem to the pointwise operations on matrices of maximum NxMxO shape and their indices.

The reconstruction operation is divided into the following:

- Initialization
- Outer loop - feeding frames in a sequence to the reconstruction and saving results
- Inner loop - implementation of the chosen reconstruction algorithm

After the initialization of the grid, weight and error arrays the first step is reading the projections to the 2D Numpy arrays of a shape (NxM) by the outer loop and then stepping into the inner loop to reshape them into NxMxO target shape by stacking the projections in third dimension O times. As each of the projections was taken along a different axis (x, y, z) the operation of stacking should be understood as simply back-projection into a dummy volume. As the stacking in 3rd dimension rebuilds different axis for each projection it is necessary to rotate the 3D projections to align the indexing with a reconstruction grid. Again due to the ray paths parallel to the axis x, y, and z, this operation reduces to the transposition of two of three 3D projections as one of them should be aligned with the reconstruction grid from the start. The next step is crucial, as by pointwise multiplying each of the 3D projections times a weight matrix it is possible to apply all kinds of priors and regularizers. If the weights are symmetrical for each projection this step can also be carried out later after calculating the voxel update. In the final implementation, two parameters are used:

- relaxation matrix used to modify the ”strength” of projection in certain areas.
- number of non-zero weights - as 3D projection voxels are equal to the value of the ray integral, projections need to be divided by the estimated number of voxels containing the tracer along the ray path. It is done by finding the range of indexes around non-zero values in the projections.

After calculating the 3D weighted projections, a point-wise average is taken to calculate the voxel update, therefore providing the simultaneous use of all projections. Adding the average to the reconstruction grid finalizes the back-projection sequence.

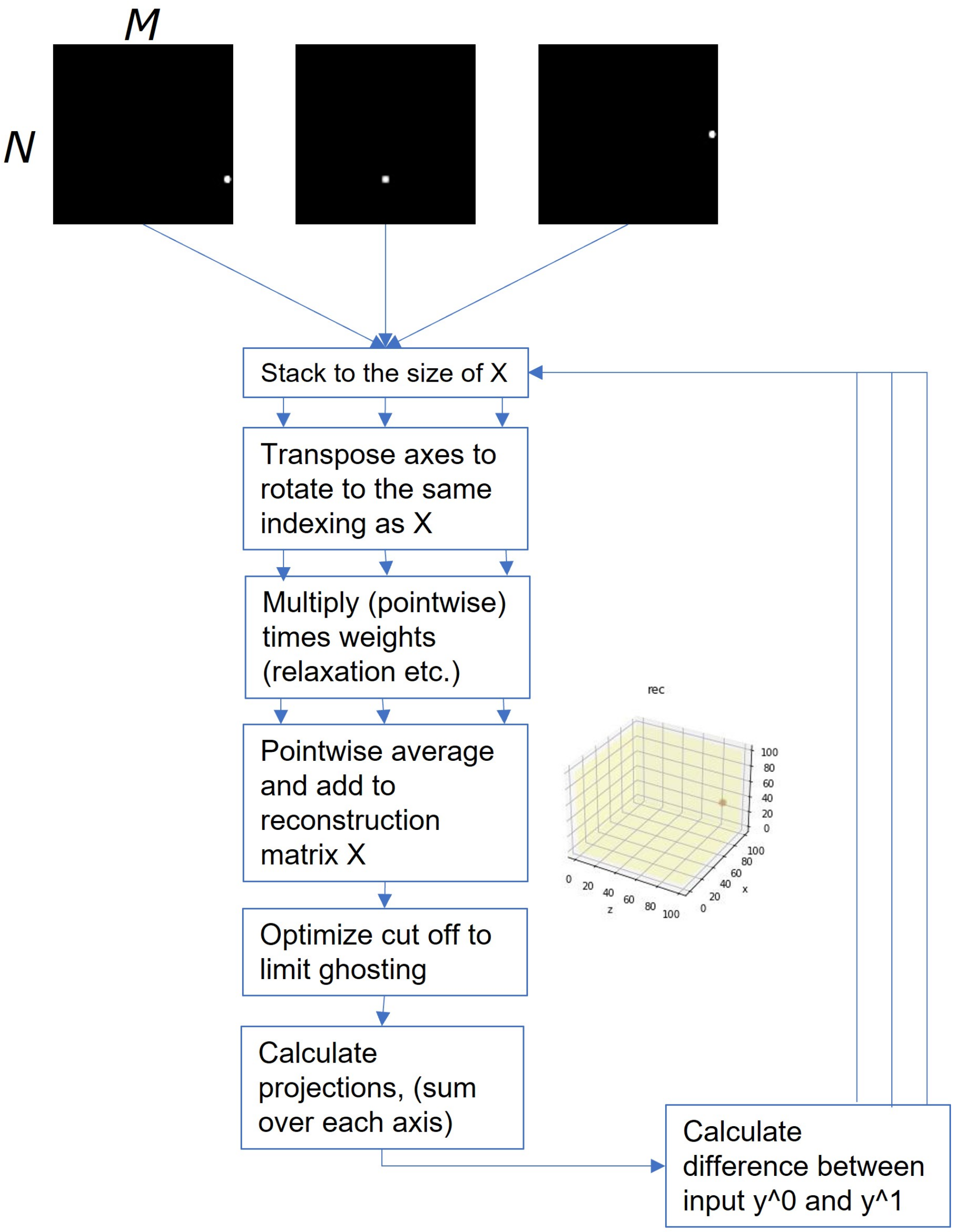

Figure 3.17: Reconstruction workflow

At this stage, ghosting is already incorporated into the reconstruction grid after the back projection completion. Given that the ghosting originates from a single projection and is mitigated by the relaxation process, it is expected to be less intense than the reconstructed object. This suggests that it should be feasible to largely eliminate ghosting that does not overlap with the actual tracer by identifying a single scalar threshold. To accomplish this, the optimization step is introduced. However, this optimization step substantially increases the computational cost of the entire process, particularly for gradient-based methods. Thus on a copy of the current state of the reconstruction grid, a Powell scheme [28] (as implemented in Scipy minimize package) is used to find a threshold by minimizing the total pointwise difference between projections derived from the filtered grid and the input projections. Opting for direct difference over more conventional cost functions like square norm has proven effective in finding a local minimum without noticeable loss in tracer spread. After identifying and applying the threshold filter, final iteration projections are computed based on the forward model. Subsequently, the pointwise difference between the input projections and the iteration result is calculated and utilized in the next iteration. In the case of frames being zero-padded, a reppading step is added to avoid error accumulation. Padding of the data allows for faster convergence of the optimisation step as it creates regions in which at all timesteps only ghosting is present. The iterating of the inner loop is terminated upon reaching a tolerance threshold for error change between the iterations or reaching the maximum number of iterations. The succeeding frame is loaded by the outer loop and the process is repeated starting with the previous timestep volume estimation. Eat each timestep the grid is saved to the CSV files and the final projections are plotted.

3.5. Mixing quantification

As outlined in the previous sections, the reconstructed volume represents relative attenuation coefficients rather than concentration data. To convert the reconstructed volume to a 3D concentration field, a series of calibration measurements is required, as described in section 3.5.3. However, this conversion introduces an additional source of experimental error and can magnify artefacts, particularly in noisy mixing data. Therefore the mixing quantification, interpreted as attenuation uniformity calculation could yield more precise results, despite complicating the comparison with concentration-based calculations. Moreover, using the attenuation domain allows for a direct comparison between the mixing metrics derived from projections and those obtained from the reconstructed data.

The coefficient of Variation (CoV) and the average grayscale value of attenuation, along with their versions normalized to the final timestep, were adapted for use with both projections and reconstruction data to assess mixing in both global and local contexts. Using the last frame as a normalization base is possible under the assumption of a long enough measuring time to achieve perfect mixing. To verify this assumption it is important to check the non-normalized CoV in the final timesteps as it by definition should be approaching zero in a homogeneous mixture.

3.5.1. Global mixing times

Inspired by works of [8] at first the average grayscale value of each projection is calculated for all timesteps,

$$A_{\text{avg}}(t) = \frac{1}{N * M} \sum_{m=1}^{M} \sum_{n=1}^{N} (a(n,m,t) - a(n,m,t=0)) \tag{3.8}$$

where (n,m) denotes the pixel indices and N, M is the resolution of the frames. Next $A_{\text{avg}}(t)$ is normalized to the final frame.

$$A_{\text{avg, norm}}(t) = \frac{A_{\text{avg}}(t)}{A_{\text{avg}}(t=\infty) - A_{\text{avg}}(t=0)} \tag{3.9}$$

Although the background subtraction is part of the preprocessing pipeline the initial frame should be substracted to assure the (0,1) normalization. For the reconstruction data means are calculated and normalized by extending eq. (3.8), (3.9) to the 'o' indices and 'O' resolution of the reconstruction grid.

For the probes of equal volume or the whole tank being the domain of the measurement CoV of concentration is equivalent to the Coefficient of Mixing as defined in [15]

$$c_{\text{mix}} = \sqrt{\left(\frac{\sum_i \left(\frac{c_i - \bar{c}}{\bar{c}}\right)^2 \Delta V_i}{\sum_i \Delta V_i} \right)} \tag{3.10}$$

Therefore to characterize the mixing intensity CoV [22] of attenuation was calculated at each timestep.

$$CoV(t) = \sqrt{\frac{1}{N_t} \sum_{i=1}^{N_t} \left(\frac{a_i - A_{\text{avg}}(t)}{A_{\text{avg}}(t)} \right)^2} \tag{3.11}$$

where N_t is the size of the reconstruction grid or frame (NxMxO or NxM).

The evaluation of global mixing times is shown in Fig. 3.18 involves determining the first frame or grid number where $A_{\text{avg, norm}}(t)$ exceed the threshold and continue to do so thereafter. As all of the timestep values are stored in one Numpy array, a boolean mask of threshold comparison is created. In the case of projection-based evaluation, the global mixing mask is created for each view and then a row product is taken to aggregate the individual comparison results as it is assumed that a threshold crossing condition is met only if it is satisfied in all projections at a given time. Next, the frame/grid number satisfying the condition is found by finding the array index at which the product of all further mask elements is True. Finally, the mixing time corresponding to this threshold is then calculated by multiplying the found frame/grid number by the average Frames Per Second (FPS) of the collected projections.

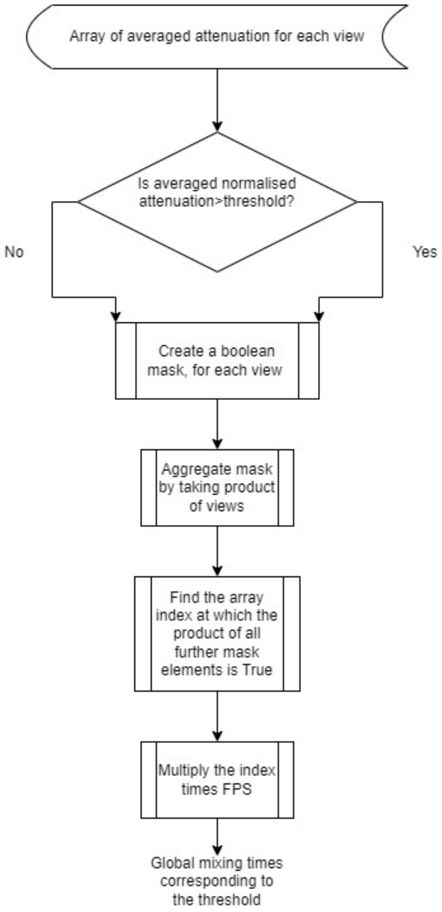

Figure 3.18: Global mixing time evaluation

3.5.2. Local mixing times

To evaluate local mixing as described in [8] mixing time map is created and then extending the idea to 3D reconstruction data, the local mixing time distribution is found in the whole mixing volume.

At first, the obtained images are used. Every frame is normalized relative to the final one on a pixel base.

$$a_{\text{norm}}(n,m,t) = \frac{a(n,m)}{a(n,m,t=\infty) - a(n,m,t=0)} \tag{3.12}$$

Then a histogram of attenuation for each timestep is generated to illustrate the temporal distribution of the normalized attenuation. In a similar manner as with global mixing the threshold is compared to the local attenuation, this time on a pixel base. Map creation workflow is summarised in Fig. 3.19

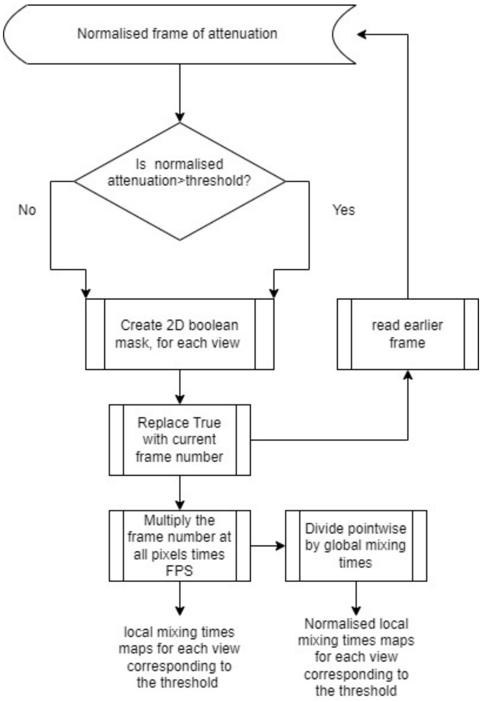

Figure 3.19: Local mixing time evaluation

Passing through the frames in reverse order a frame for each view is calculated with each pixel value being replaced by the number of timesteps needed to pass and remain above the threshold. The resulting frame is multiplied times FPS to create a mixing time map of each reactor view. To relate global and local mixing, the mixing time map is divided by the global mixing time. Such a map as seen in 3.20 could be a very valuable visualisation, as it allows to approximate the location of the dead zones.

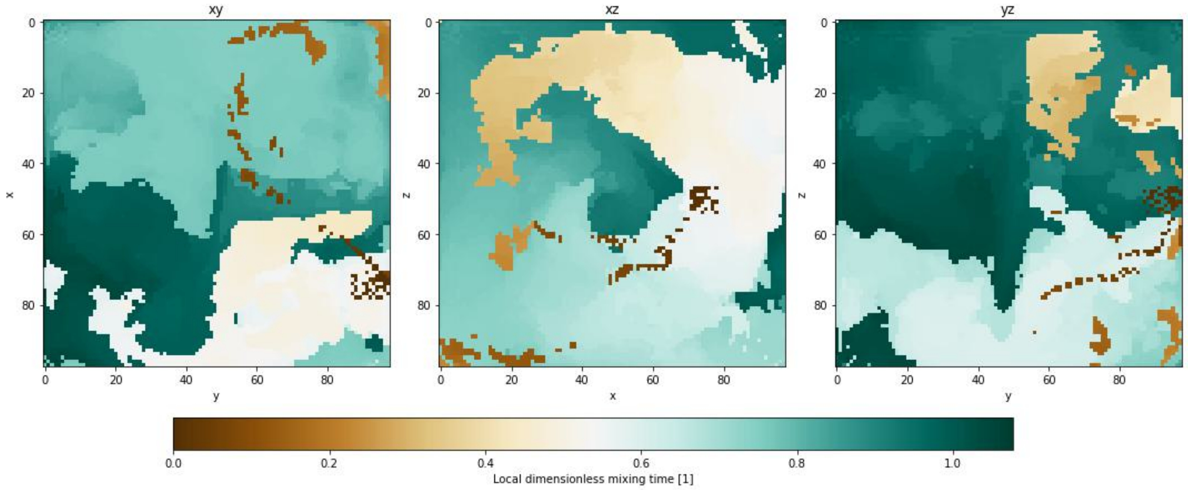

Figure 3.20: Example normalised mixing map

Although it can be confusing due to the representation of essentially three-dimensional phenomena on a two-dimensional plane.

Using the tomographic reconstruction data 3D mixing time map is calculated in essentially the same manner as in 2D case 3.19

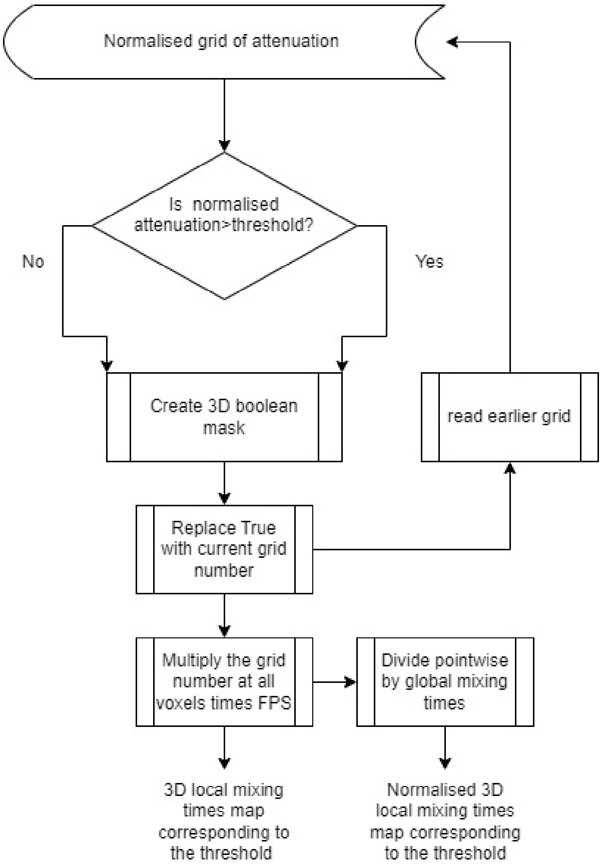

Figure 3.21: Local mixing time evaluation in 3D

Some minor changes in implementation due to the operation on much larger matrices are required as well as shifting from pixel-based calculation to operating on voxels as shown in fig.3.21. An example final result of a 3D normalised mixing map is shown in Fig. 3.22

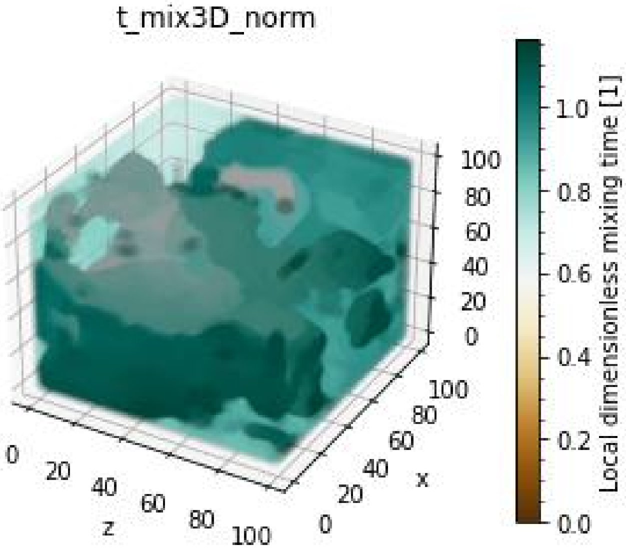

Figure 3.22: 3D normalised mixing map

To show the mixing intensity progression CoV is calculated using a non-overlapping sliding window (later called cube due to its three-dimensional nature) as in eq. 3.13 relating the values within the cube to the global grid average.

$$CoV(t) = \sqrt{\frac{1}{C}\sum_{i=1}^{C}\left(\frac{a_i - A_{\text{avg}}(t)}{A_{\text{avg}}(t)}\right)^2} \tag{3.13}$$

where C is in the range of sliding cube indexes at the current position.

The resulting visualization as in the fig. reffig:3DCoV shows the difference in homogeneity at a local scale (of the cube size) at each timestep.

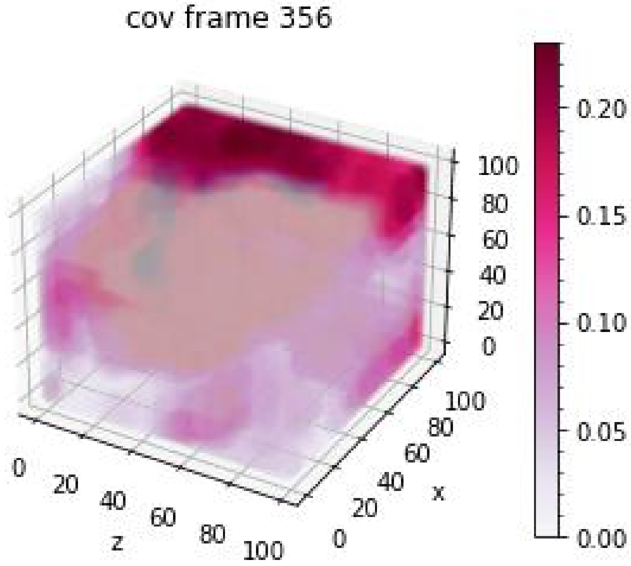

Figure 3.23: 3D CoV distribution

3.5.3. Concentration calibration

For the direct mixing evaluation, creating a calibration curve relating the light absorption with the tracer concentration is unnecessary, but if the goal is to compare with CFD results recreating the three-dimensional concentration field is beneficial. The reconstructed voxels attenuation is related to the dye concentration through the forward problem solution. Therefore a series of thoroughly mixed tanks with varying concentrations should be captured within the same setting as the mixing experiment. Knowing the tank length the Lambert-Beer equation can be written:

$$ln(\frac{I_0}{I(C)}) = \alpha * l * C \tag{3.14}$$

where: I_0 is the pixel value in grayscale corresponding to the dye-free tank; $I(C)$ is the pixel value for a given concentration; l is the tank length measured in the direction of the light path, C the dye concentration and α molar absorption coefficient. Plotting the concentration against $ln(\frac{I_0}{I(C)})$ allow to calculate α using linear regression, which now can serve to predict the concentration values for registered I_0 and I.

The voxel's relative attenuation (product of voxel distance and attenuation coefficient) is obtained by back-projecting the pre-processed projections. The pre-processing transform the image from intensity $I(n,m,t)$ to total attenuation $a(n,m,t)$.:

$$a(n,m,t) = \neg I(n,m,t) - \neg I(n,m,t=0) = \sum_{i=0}^{O} a(n,m,o,t) \tag{3.15}$$

where $\neg$ represents the bitwise NOT operation used for colour inversion which in 8-bit greyscale is equivalent to simply subtracting pixel value from 255. So:

$$a(n,m,t) = I(n,m,t=0) - I(n,m,t) = \sum_{i=0}^{O} a(n,m,o,t) \tag{3.16}$$

Recalling the discretization along the ray path from section 3.1:

$$\frac{dI}{dx} = \alpha * C \tag{3.17}$$

$$\frac{I(x_i) - I(x_{i+1})}{x_i - x_{i+1}} = \frac{\Delta I_i}{\Delta x_i} = \alpha * C_i \tag{3.18}$$

$$p = \sum_{i=0}^{N} \Delta I_i = \sum_{i=1}^{N} (\alpha * C_i * \delta) \tag{3.19}$$

following holds:

$$\sum_{i=1}^{O} a(n,m,o,t) = \sum_{i=1}^{O} (\alpha * C(n,m,o,t) * \delta) \tag{3.20}$$

Therefore concentration can be recursively calculated along the ray path knowing $a(n,m,o,t)$, α from the calibration curve and δ as:

$$C(n,m,o+1,t) = \frac{\sum_{i=0}^{o+1} a(n,m,i,t)}{\alpha * \delta} - C(n,m,o,t) \tag{3.21}$$

Due to the lack of time and not essential nature, the concentration calculations were not implemented and the calibration curve of the used dye was not obtained.

4

Results & discussion

4.1. Synthetic data reconstruction

At first synthetic data was used to demonstrate the potential of the method in a perfect experimental environment. The reconstruction grid of a shape (100,100,100) with one-pixel padding. If not mentioned otherwise it should be assumed the following parameters were used for all experiments :

- relaxation parameter: 0.4
- maximum number of iterations: 15000
- tolerance: 0.0001

As the frames were created from concentration data, they are free of impeller projection, which in actual experimental footage is the source of multiple challenges, arising from its interaction with the beam.

4.1.1. Image reconstruction

The comparison between input projections and output projections represents the reconstruction error, as it is the only way to directly evaluate the experimental frames against the results of the reconstruction. In one of the early trials influence of the initialization point was checked. It was found that although the error difference between the two was marginal (Fig. 4.1) the backward reconstruction was much faster and resulted in a better volume reconstruction as the forward approach failed to achieve uniform concentrations in the final grids (as in case the of simulated raw data - Fig 4.2 - scale difference due to normalization of frames). Total pointwise difference and view pointwise difference graphs can be found in Appendix A.1

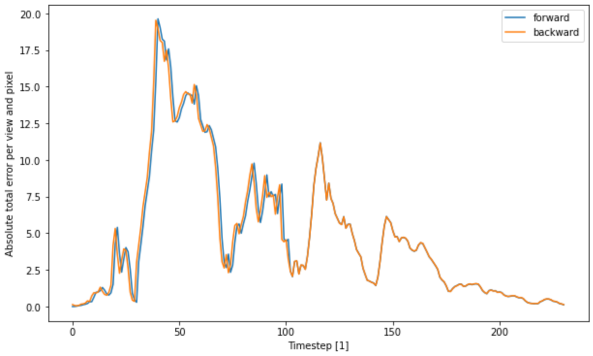

Figure 4.1: Total absolute point-wise difference per pixel after synthetic data reconstruction

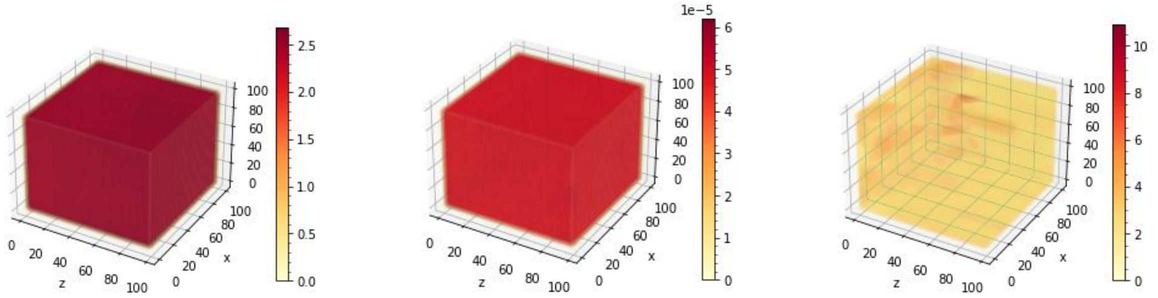

(a) Backward reconstruction

(b) Concentration grid from simulation

(c) Forward reconstruction

Figure 4.2: Forward vs backward reconstruction final grids

Therefore all of the further reconstructions used the backwards sequence. In Fig. 4.3 the reconstruction error understood as a total difference per pixel at each timestep was plotted and divided into four phases:

- I - 0-30 frames of tracer injection, high accuracy
- II - 30-125 full volume mixing, low accuracy
- III - 50-125 full volume mixing, medium accuracy
- IV - final mixing stage, high accuracy

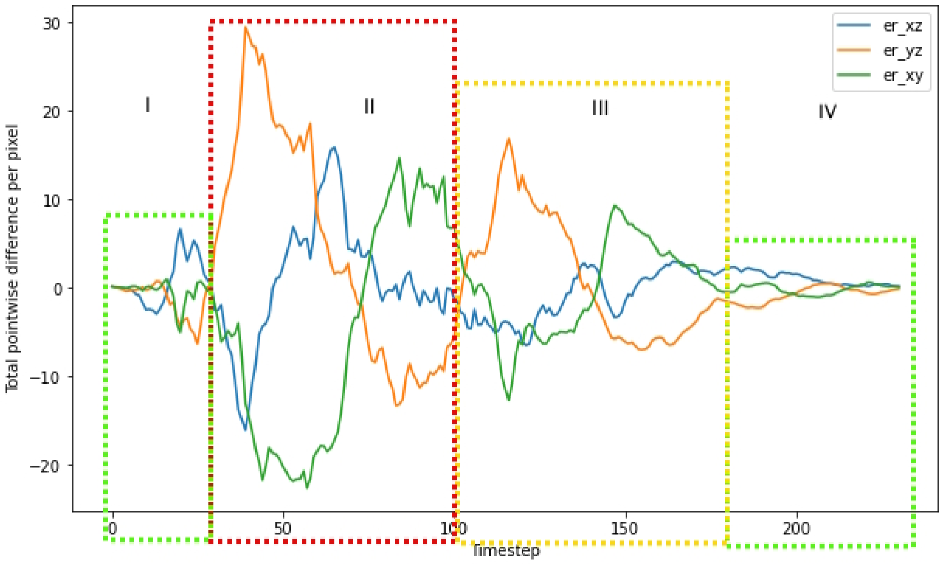

Figure 4.3: Total point-wise difference per pixel after synthetic data reconstruction

Despite the fluctuating reconstruction error, visually there is no difference between the input and output as we can observe in Fig. 4.4. Therefore for each example visible in Fig. 4.4 MSSIM and EHS (subsection 3.3.3) were calculated.

Frame number	MSSIM	EHS
0	1.00	0.99
50	0.98	0.56
175	1.00	0.83
230	1.00	0.90

Table 4.1: Image similarity indexes calculated for example frames

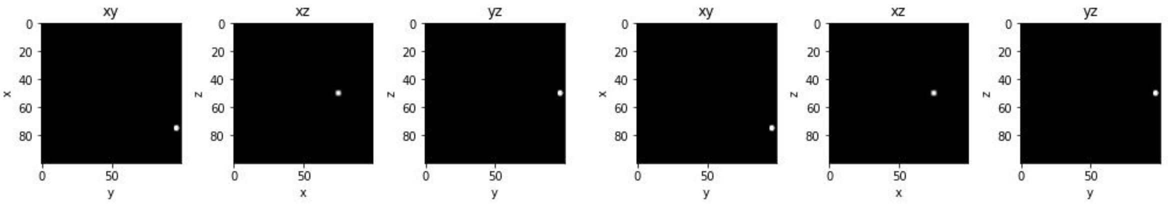

(a) Tracer injection

(e) Tracer injection

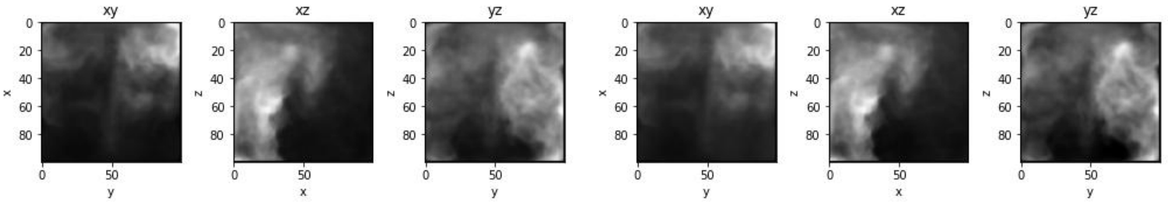

(b) 50th frame, 1st ”error zone”

(f) 50th frame, 1st ”error zone”

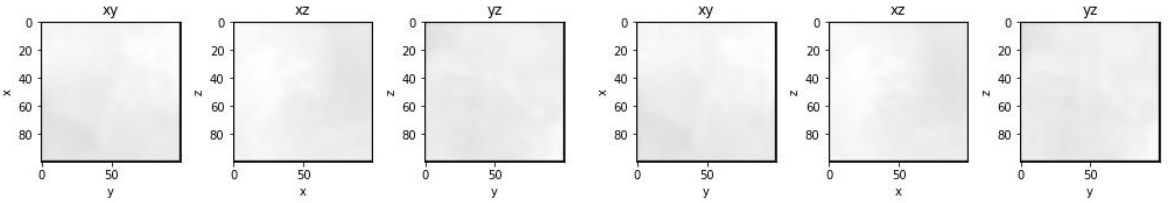

(c) 175th frame, 3rd ”error zone”

(g) 175th frame, 3rd ”error zone”

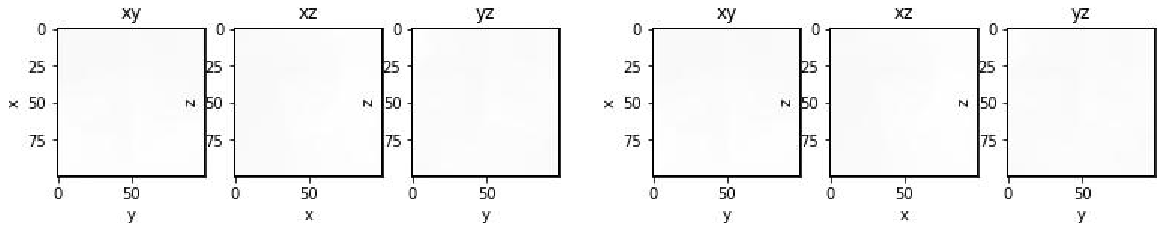

(d) Final input frame

(h) Final frame

Figure 4.4: Input (left) vs output (right) synthetic frames

The discrepancy in metrics could account for the non-observable differences between the input and output. High MSSIM indicates the near-perfect structural similarity of the frames. However, a much lower EHS (which is based on histogram comparison) particularly where the tracer is present in the whole mixing volume, might suggest the occurrence of unfiltered ghosting. Voxels of high attenuation occlude the ones of lower non-zero value ones, increasing the frame's overall brightness. As the tank approaches the fully mixed state, the ghosting is less significant as the whole volume achieves some degree of uniformity. The heightened error in phases II and III implies that the ghosting filtering method may only be partially effective during these stages and could be too computationally demanding to use in all frames. The filtering appears to be most impactful during the early mixing stages when shapes are clearly defined. However, to fully assess its impact, the reconstructed volume must be examined.

4.1.2. 3D tracer distribution reconstruction

The reconstruction grids of each phase identified in the previous subsection, are shown together with the raw concentration data visualizations. Direct comparison of the voxel values and concentration is not straightforward due to frame normalization (resulting in huge scale difference) and the recursive method of translating attenuation back into concentration (3.5.3). Therefore reference data is shown mostly to assess the structural integrity of the reconstruction and allow to identify ghosting.

The reconstruction is reasonably accurate for the first thirty grids, which represent the injection phase (Fig. 4.5). The ghosting filter effectively handles the simple shapes of tracer spreading from the injection point, which due to their low irregularities and occlusion, are easier to reconstruct. Furthermore, ghosting occurs along a longer part of the ray, with object interaction over a short distance. This, coupled with a strong relaxation factor, results in significantly reduced ghosting intensities compared to the reconstructed tracer, leading to easier filtering. The importance of the filtering can be observed in appendix A.9 A three-viewpoint set of observations appears sufficient to perfectly capture the injection conditions.

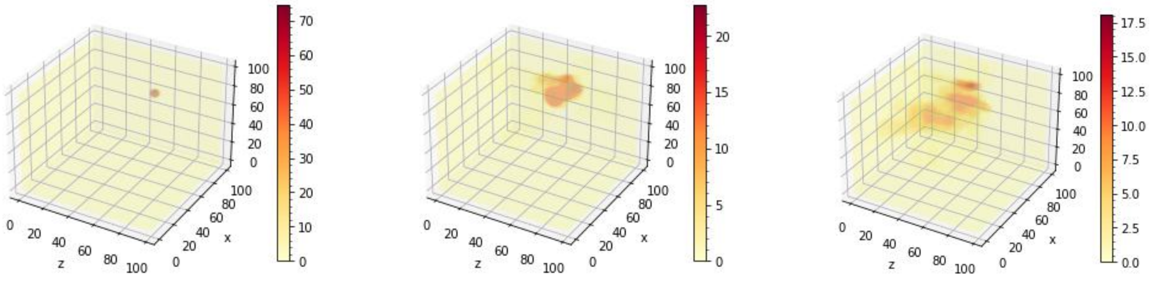

(a) Reconstruction, t=0 [s] **(b)** Reconstruction,t=1 [s] **(c)** Reconstruction, t=2 [s]

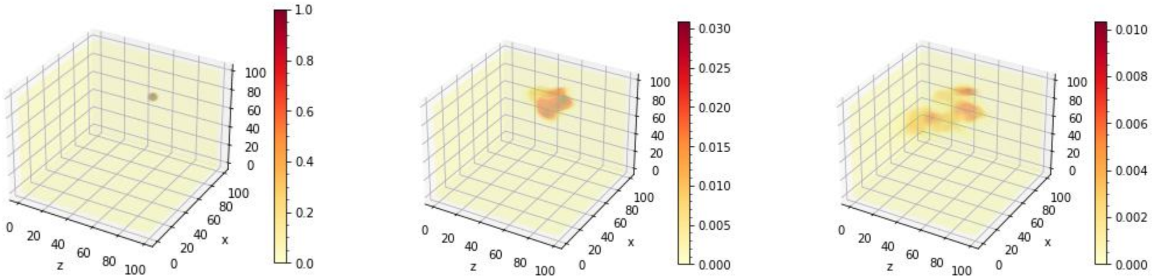

(d) Reference, t=0 [s] **(e)** Reference, t=1 [s] **(f)** Reference, t=2 [s]

Figure 4.5: Injection grids - reconstruction (attenuation) vs reference (concentration)

In the second phase (Fig 4.6) where the tracer occupies (with varying concentration) most of the available volume the ghosting start to be more apparent. The shapes start to be irregular and from some points of view, the tracer structure is highly non-uniform with gaps occluded by the zones of high concentration. These are the most challenging objects to reconstruct and the limitations of only three angles projections acquisition are reflected in the highest projection reconstruction error (Fig.4.3) However, the main tendencies are conserved as the reconstructed shape shows a resemblance to the reference and zones of high concentration correctly placed but blurred due to increasing ghosting.

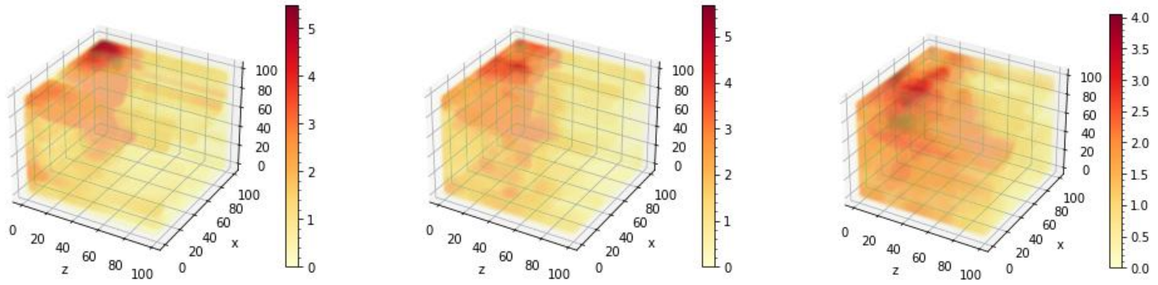

(a) Reconstruction, t=4 [s] **(b)** Reconstruction, t=5 [s] **(c)** Reconstruction, t=6[s]

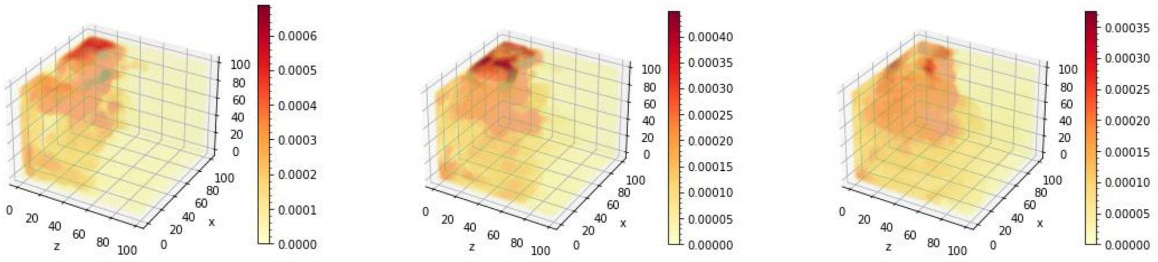

(d) Reference, t=4 [s] **(e)** Reference, t=5 [s] **(f)** Reference, t=6 [s]

Figure 4.6: Phase II - full volume spreading grids - reconstruction (attenuation) vs reference (concentration)

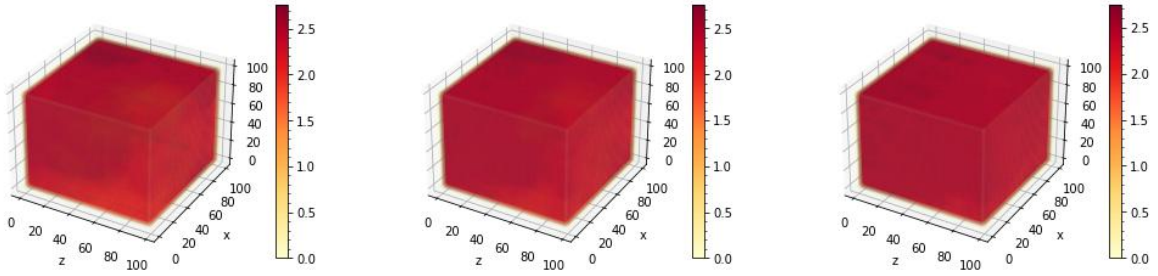

(a) Reconstruction, t=16.5 [s] **(b)** Reconstruction, t=17.5 [s] **(c)** Reconstruction, t=18.5 [s]

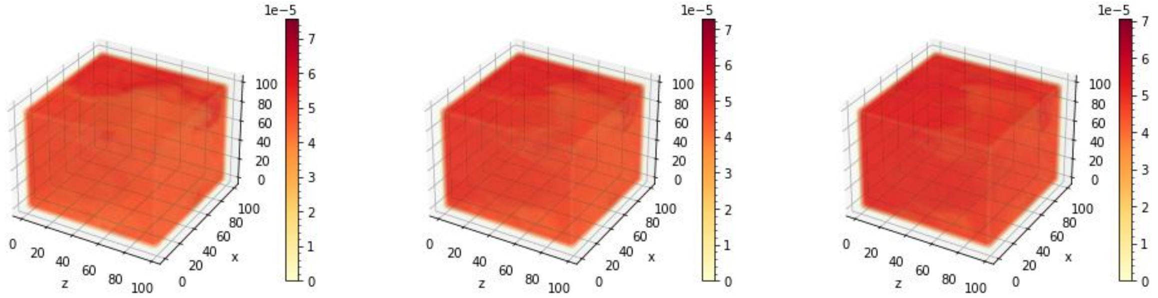

(d) Reference, t=16.5 [s] **(e)** Reference, t=17.5 [s] **(f)** Reference, t=18.5 [s]

Figure 4.7: Phase III - full volume mixing grids - reconstruction (attenuation) vs reference (concentration)

Phase three is characterized by the tracer presence in the entire tank's volume, achieving a high level of uniformity. However, some zones still exhibit noticeable differences in voxel attenuation. The phenomenon of ghosting is less pronounced due to the absence of highly contrasting zones as the distribution of tracer among all the ray paths is much smoother than in phase two. The overall projection reconstruction error is lower than in phase II yet the tracer reconstruction in phase III is not easier as a necessity to capture less evident attenuation variations arises. Although ghosting is less apparent, its presence at this stage can lead to problems in the mixing time calculation, as it increases the grid uniformity which can lead to faster mixing-threshold crossing.

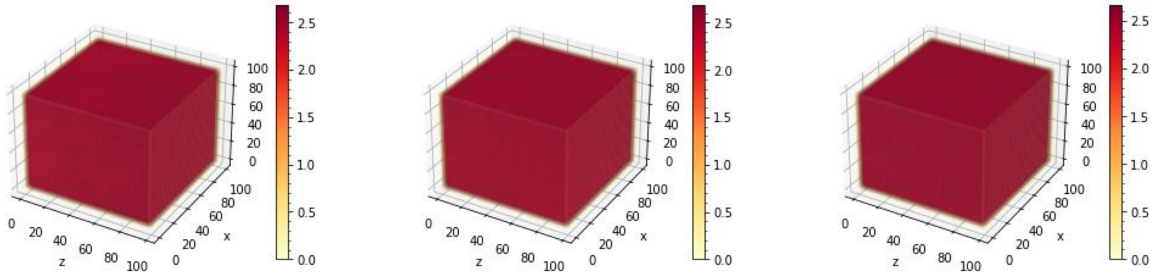

(a) Reconstruction, t=23 [s] **(b)** Reconstruction, t=24 [s] **(c)** Reconstruction, t=25 [s]

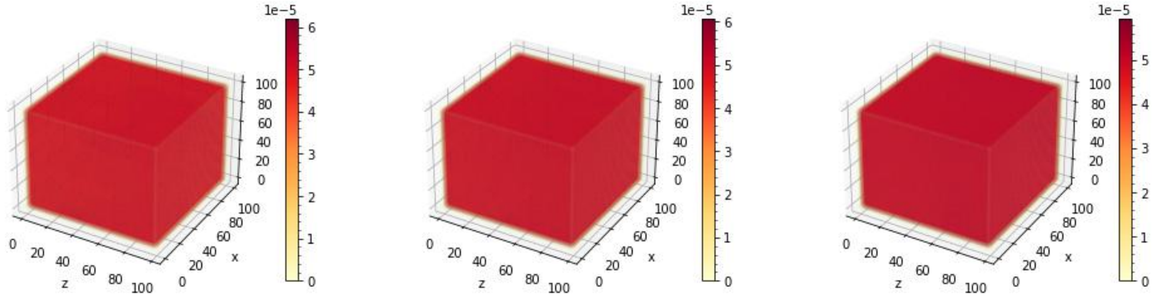

(d) Reference, t=23 [s] **(e)** Reference, t=24 [s] **(f)** Reference, t=25 [s]

Figure 4.8: Phase IV - final fully mixed grids - reconstruction (attenuation) vs reference (concentration)

Phase IV in most cases with a long enough experiment time, reduces to reconstruction of uniform tracer distribution. However, it has a crucial influence over all of the post-processing, as the voxel attenuation values from the last frames serve as a normalization base and to calculate the mixing thresholds. Therefore it is necessary to ensure that in the final frames, the tank volume is well mixed by checking the CoV value.

Source	CoV
Reconstruction	0.00199
Reference Concentration grid	0.00154

Table 4.2: CoV of synthetic data last reconstruction and reference grids

CoVs in both cases are low, so the last grids are assumed to be fully mixed - for example in [15] authors connected $CoV = 0.00566$ to the 99% mixing times. Visualization of more reconstruction timesteps can be found in Appendix A.2

4.1.3. Mixing

First, the mixing times were roughly estimated using the correlation proposed in [7] for Rushton turbines in conditions of turbulent mixing (eq. 4.1).

$$t_U = \frac{-\ln(1-U)}{1.06N(D/T)^{2.17}(T/H)^{0.5}} \tag{4.1}$$

where:

- t_U: mixing time for a given threshold U [s]
- N: rotations per second [s^{-1}]

- D: impeller diameter [m]
- T: tank diameter [m]
- H: tank height [m]

This equation is meant to be used for a cylindrical vessel in turbulent mixing conditions. Therefore the Reynolds number is calculated as:

$$Re = \frac{\rho N D^2}{\mu} \tag{4.2}$$

where the following values were used:

- ρ: density of water at 25 °C ($997[kg/m^3]$)
- μ: dynamic viscosity of water at 25 °C $0.0008891[Pa * s]$
- $N : 0.5[s^{-1}]$
- $D : 0.05[m]$

The resulting Re=934 is much lower than the suggested 5000 [7] to assume turbulent mixing. However, the cubic geometry of the tank can lead to more turbulent mixing and eq. 4.1 serves just as a rough estimate. The global mixing times were assessed as described in section 3.5 and presented in a table below.

Method	Global (95%) mixing times[s]	Global (85%) mixing times[s]
Frames	23.17	16.05
Reconstruction	18.45	13.64
Estimated (eq. 4.1	23.06	14.6

Table 4.3: Global mixing times evaluated on synthetic data

As expected and explained in a previous section, the global mixing time observed in the reconstruction is much lower than the frame based due to the presence of ghosting. The mixing times predicted by the use of the correlation are of similar magnitude.

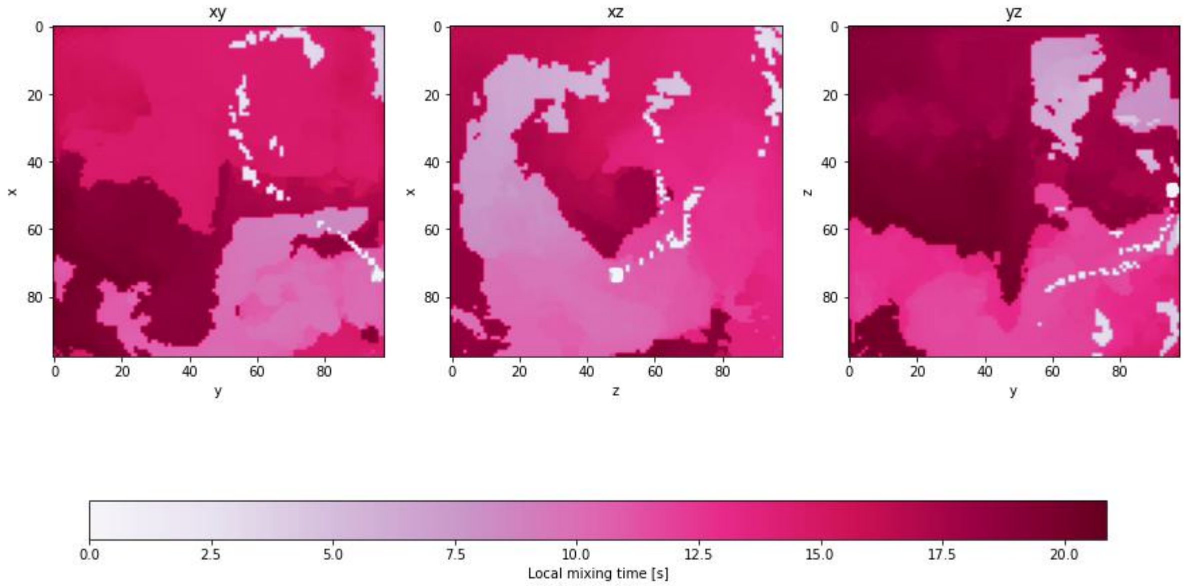

Figure 4.9: Synthetic data non-normalised mixing map

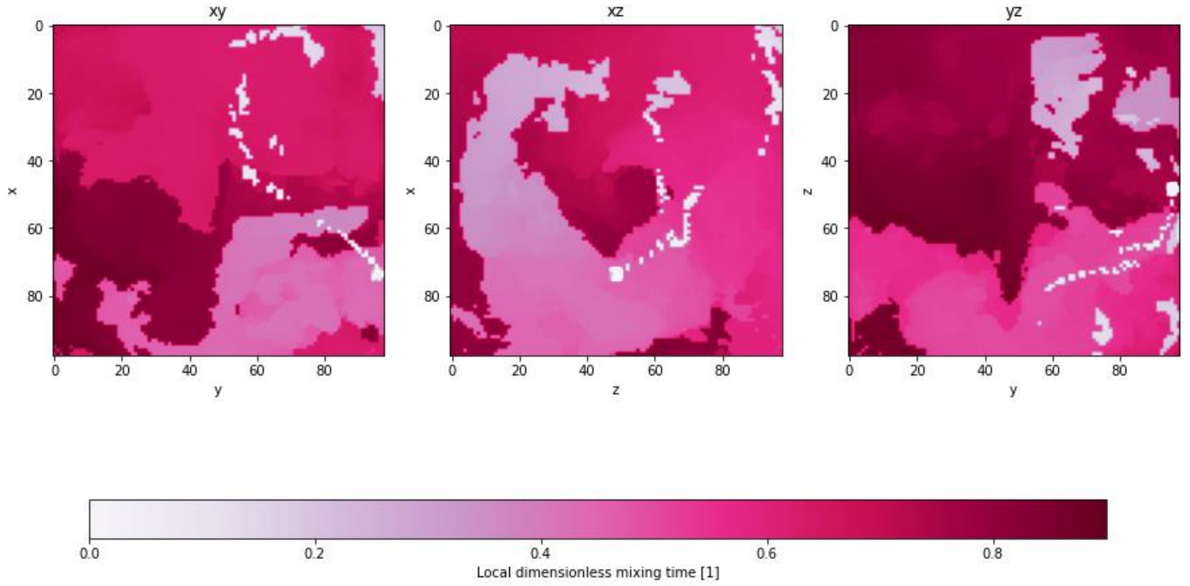

Figure 4.10: Synthetic data normalised mixing map

The 2D mixing maps were successfully created and allowed for the initial estimation of the mixing intensity distribution. In all of the views, the tracer injection point and its initial trajectory towards the wall show the shortest mixing time. Assuming standard radial flow patterns of Rushton turbines [16] mixing distribution seems reasonable. The tracer, initially injected above the impeller, is immediately swept into the upper circulation loop towards the turbine and then propelled towards the wall. Upon contact with the wall, the tracer divides into the top and bottom circulation loops and is directed back towards the centre. Here, it is partially redistributed to the tank's other side, resulting in a prolonged period to reach the corner opposite its initial trajectory.

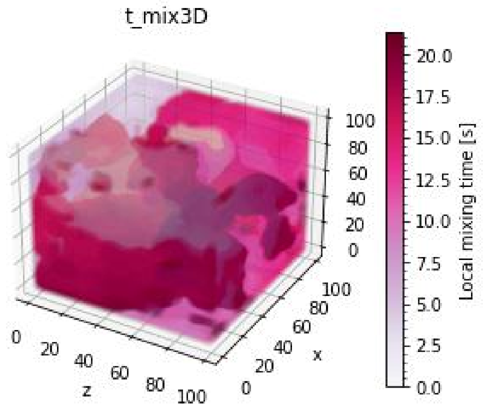

Figure 4.11: Synthetic data 3D non-normalised mixing map

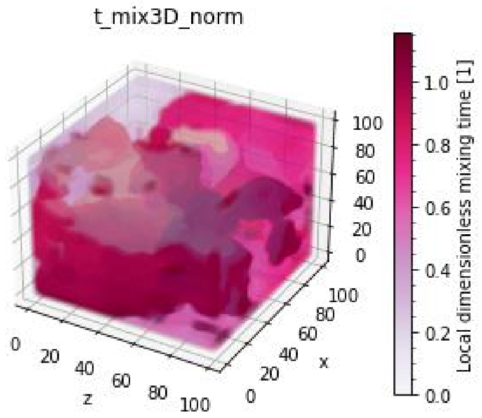

Figure 4.12: Synthetic data 3D normalised mixing map

The 3D mixing map aligns with both the reference data and the reconstructed observations. Areas near the injection site achieve the final concentration quicker than the opposite edges. However, the mixing maps obtained are specific to the injection point. Thus, to gain a comprehensive understanding of the vessel's mixing, it's necessary to compare different injection points. In this study, due to reconstruction times, only a single injection point is considered for both experimental and synthetic data.

Observing the local CoV (calculated over a sliding cube, chapter3.5), especially in the final stages can lead to a better understanding of mixing intensity regardless of the point of injection. In grids well past the global mixing times a small local CoV can be still visible, highlighting the areas of the least mixing intensity:

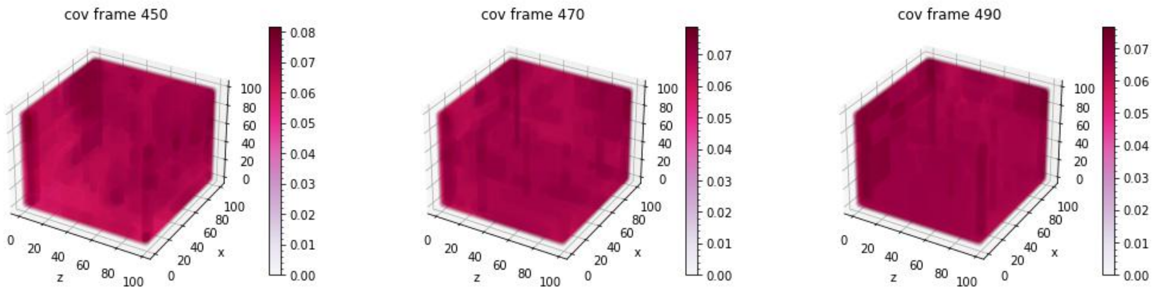

(a) Local CoV, t=25 [s] **(b)** Local CoV,t=27 [s] **(c)** Local CoV, t=29 [s]

Figure 4.13: Local CoV in final grids

In Fig. 4.13 said regions correspond to the vessel corners mostly. In the corners the liquid wall interaction is the strongest strongly limiting the flow and in extreme cases can lead to dead-zones creation and tracer accumulation - especially in the case of a solid-liquid system.

4.2. Experimental data reconstruction

Despite the shortcomings of the experimental setup the data was collected and reconstruction attempted. Due to the larger number of frames the tolerance and maximum number of iterations per timestep had to be lowered to reduce the computational cost and shorten the reconstruction time. The following parameters were used:

- relaxation parameter: 0.4
- maximum number of iterations: 3000
- tolerance: 0.001

Although lowering the parameters lead to worse reconstruction result, the low quality of the input described in chapter 3.2.2, prevent the algorithm convergence causing the use of the maximum number of iterations at all timesteps.

4.2.1. Image reconstruction

In Fig. 4.3 the reconstruction error was plotted and divided into three phases:

- I - 0-75 injection & initial mixing
- II - 75-200 full volume mixing,
- III - 50-125 full volume mixing, error stability

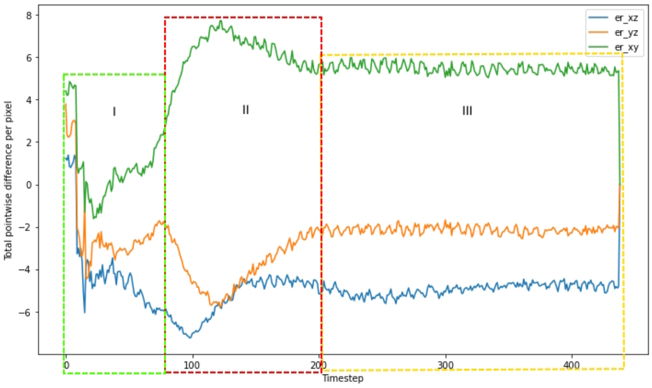

Figure 4.14: Total point-wise difference per pixel after experimental data reconstruction

The frames seem to be reconstructed with higher accuracy than the synthetic data at first glance. It can be associated with the presence of zero-intensity objects in the whole mixing period such as the impeller and the top unfilled part of the tank. Those objects became the main target of ghosting filtering as they take a significant part of the projections. Extensive filtering might be also one of the reasons for increased computational time.

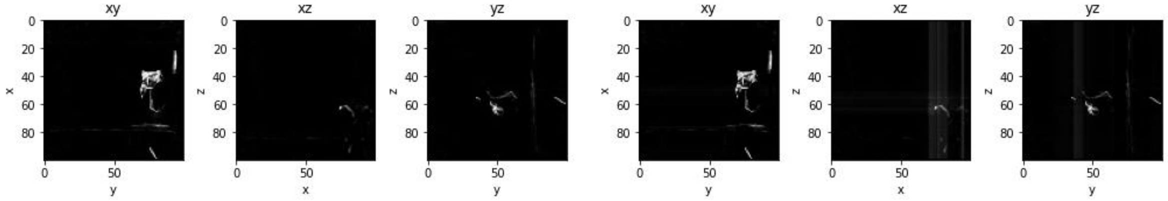

(a) Tracer injection

(f) Tracer injection

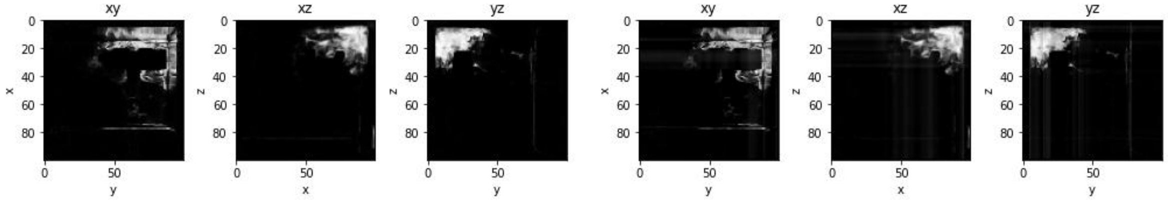

(b) 57th frame, 1st ”error zone”

(g) 57th frame, 1st ”error zone”

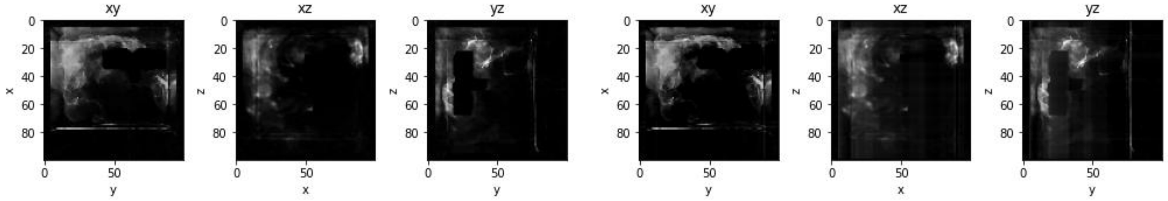

(c) 127th frame, 2nd ”error zone”

(h) 127th frame, 2nd ”error zone”

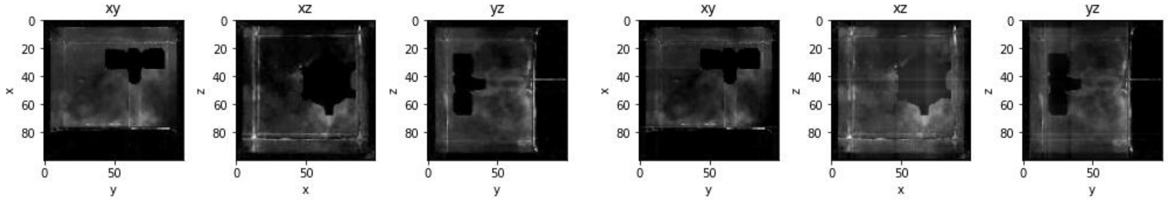

(d) 257th frame, 3rd ”error zone”

(i) 257th frame, 3rd ”error zone”

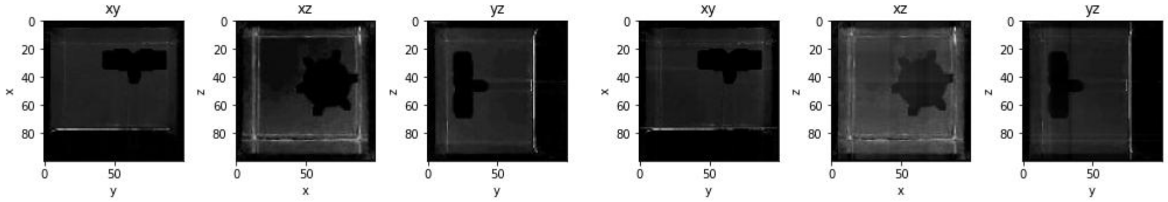

(e) Final input frame

(j) Final input frame

Figure 4.15: Input (left) vs output (right) experimental frames

Analogously to the synthetic data, the differences are not apparent, therefore similarity indexes were calculated.

Frame number	MSSIM	EHS
21	0.91	0.63
55	0.87	0.58
125	0.88	0.51
255	0.91	0.46
532	0.92	0.52

Table 4.4: Image similarity indexes calculated for example frames

Even with the reduced error shown in Fig. 4.14, all sampled frames display lower structural and entropy similarity metrics compared to synthetic data. Thus, the dominance of zero-intensity objects in the reconstruction error is further implied. The observation of the reconstructed volume would give further insight into the matter.

4.2.2. 3D structure reconstruction

The injection reconstruction at first is quite accurate and the difference between input and projections quickly falls below zero. It indicates the higher intensity of the projections in comparison with the input. The underlying cause could be the variable number of pixels constructing the impeller in each view due to preprocessing, leading to discrepancies between its projections. Furthermore, a slight misalignment of the experimental setup could contribute to this issue. Despite these challenges, the reconstructed tracer path generally aligns well with what was observed during the experiments. This is the case even though parts of the tracer are obscured by the impeller, and despite the fact that the tracer was partially eliminated around the impeller projection to minimize artifact creation. Projections gathered from three viewpoints appear to provide the means for the reconstruction of the initial tracer path, for the injection point used. However, if the dye were to be injected directly over the turbine, the bottom view would be entirely obstructed, and the quality of the reconstruction would consequently suffer.

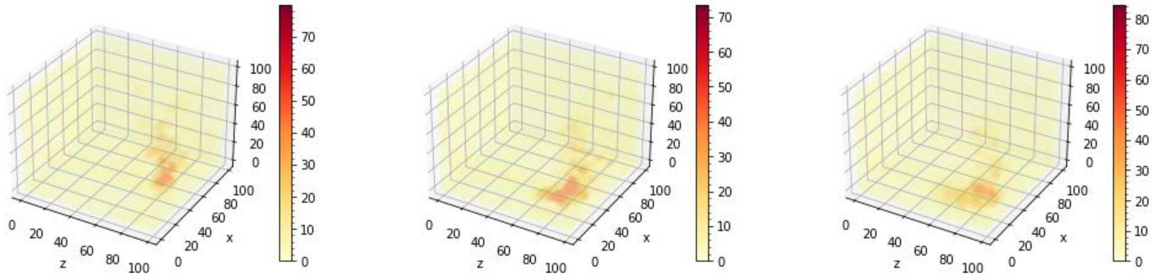

(a) Reconstruction, t=0.4 [s]   **(b)** Reconstruction,t=0.8 [s]   **(c)** Reconstruction, t=1.2 [s]

Figure 4.16: Injection grids - reconstruction of experimental data

In phase II, ghosting begins to emerge, accompanied by surface light refraction. As the tracer disperses further, noise becomes increasingly apparent, a result of the forward problem assumptions being violated, as explained in chapter 3.2.2. The impeller's position is not distinctly identifiable in the reconstruction. Nevertheless, the overall trend of the tracer trajectory appears to be preserved. The radial flow from the impeller towards the wall, followed by its redirection towards the tank corners upon interacting with the wall, seems to be adequately captured. As the ghosting is visible (especially in the regions behind the impeller) more viewing points could improve the reconstruction. However, introducing more projections further breaking the assumption, could lead to the increasing dominance of the reconstruction artifacts.

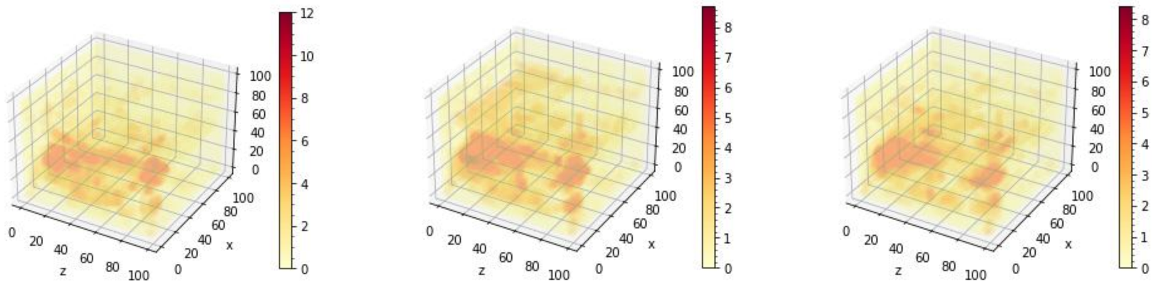

(a) Reconstruction, t=4 [s]

(b) Reconstruction, t=4.4 [s]

(c) Reconstruction, t=4.8 [s]

Figure 4.17: Phase II - full volume mixing

In phase three as the tracer occupies the whole tank volume the main source of irregularities within the reconstruction seems to be the artifacts created from the projections noise and experimental setup flaws. In the next subsection where mixing time was estimated this observation is further supported, as most of the phase III frames show the tank state past the predicted global mixing time. Although it is hard to distinguish between the reconstruction of the edge effects of refracting light and slight tracer accumulation in the corners.

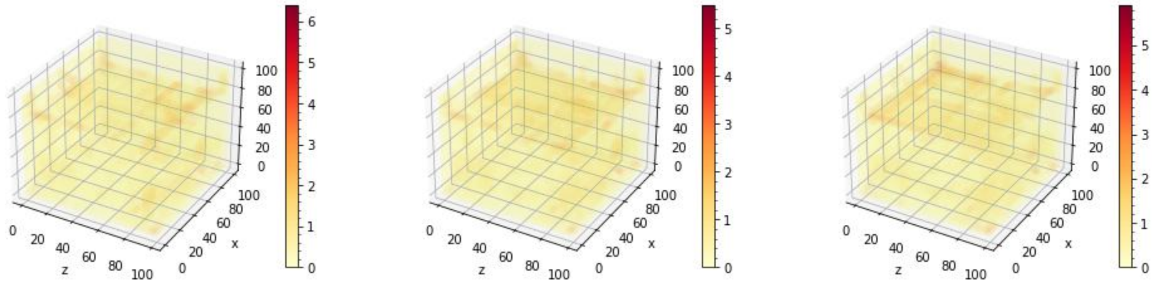

(a) Reconstruction, t=9.6 [s]

(b) Reconstruction, t=10 [s]

(c) Reconstruction, t=10.6 [s]

Figure 4.18: Phase III - error stabilisation

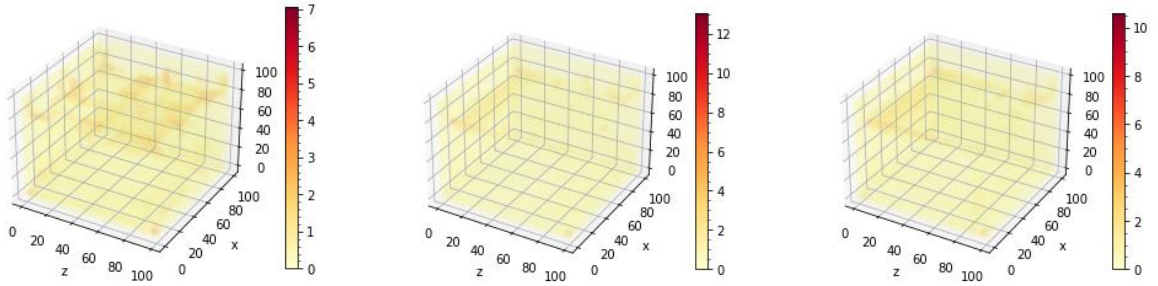

(a) Reconstruction, t=19.8 [s]

(b) Reconstruction, t=20.2 [s]

(c) Reconstruction, t=20.6 [s]

Figure 4.19: Experimental data reconstruction, final grids

The final grids appear to be fully mixed with the exception of the surface and edge zones, which can be linked to the previously explained projection acquisition flaws. The very high CoV equal to 1.24 can also be associated with said flaws as well as the presence of the impeller, which perfectly reconstructed consists of a large zeroes zone and could dominate the CoV calculation.

4.2.3. Mixing

The global mixing times were estimated in the same way as with synthetic data:

Method	Global (92%) mixing times[s]	Global (85%) mixing times[s]
Frames	14.84	11.12
Reconstruction	8.88	7.08
Estimated (eq. 4.1	9.72	7.3

Table 4.5: Global mixing times evaluated on experimental data

The higher impeller speed, determined by the equipment capabilities (20 RPM is below the minimal speed), its eccentricity and the slightly altered dimensions of the experimental setup (see 3.1), leads to more turbulent mixing (evidenced by a higher Re=2018) and a decrease in estimated mixing times. Instead of 95% mixing time 92 % was used since, despite analyzing 24 seconds of footage, the higher threshold did not stabilize. This instability could be attributed to factors such as the interaction of light with the water interface and various other artifacts, like the visibility of the tank edges in the input due to too little distance between the camera and the tank. These factors arise from the unfulfilled assumptions, as discussed in 3.2.2. Further, the impeller, captured in different positions, is composed of a variable number of pixels, which affects the mean calculation.

Interestingly, the global mixing times computed using the reconstruction data align more closely with the values anticipated by eq. 4.1. One plausible explanation for this finding is that the ghosting effect occurring during the reconstruction may reduce the mixing time, thereby counterbalancing the opposing effects of the impeller and projection flaws.

The local two-dimensional mixing maps, despite the high level of grain, still provide basic insight into the occurring mixing. The top corner located furthest from the injection point emerges as the area experiencing the longest mixing times. This is logical as the tracer needs to traverse the longest path to reach this corner. Moreover, corners are typically characterized by lower mixing intensity. The zero mixing time observed in the impeller and empty zones serves as evidence that the ghosting filtering approach effectively confines the tracer's reconstruction to the liquid domain. The coarse granularity in the 2D maps clearly does not accurately reflect the actual mixing dynamics. In the bulk, a smooth profile of mixing times is anticipated, and there is no justification for such compartmentalized mixing intensity.

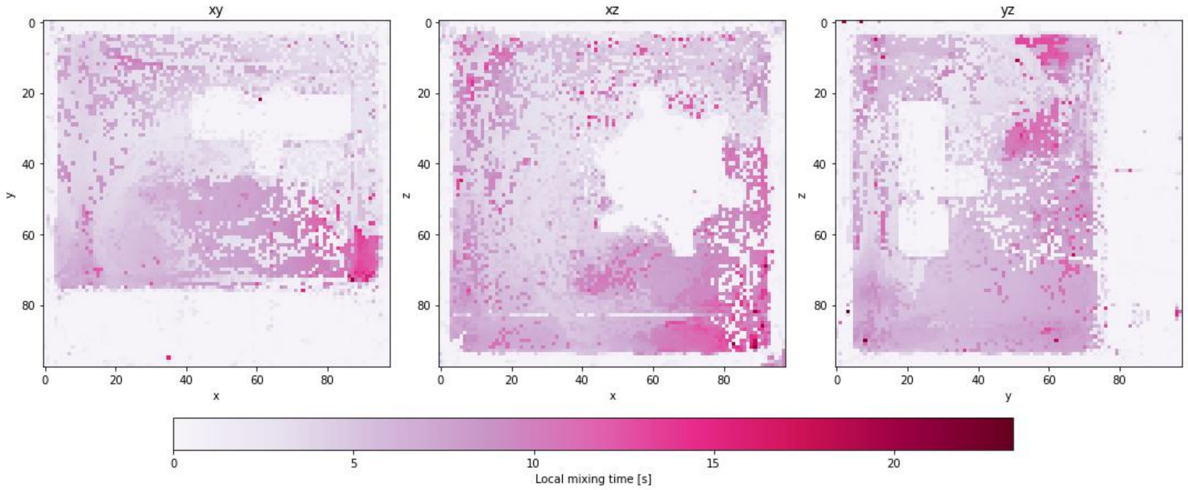

Figure 4.20: Experimental data non-normalised (92%) mixing map

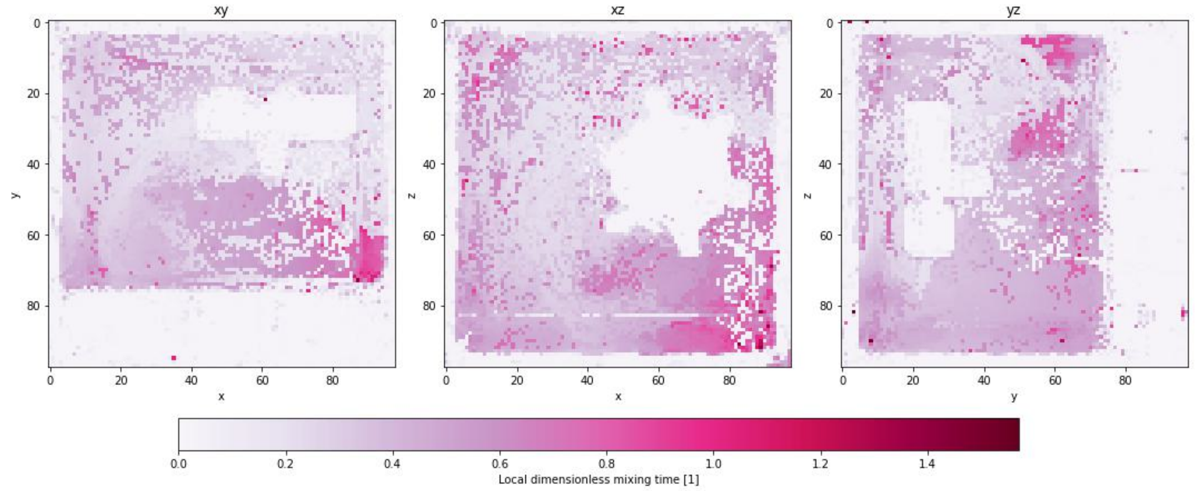

Figure 4.21: Experimental data normalised (92%) mixing map

The three-dimensional mixing maps are presented upside-down as the surface noise and the longest mixing times in the upper part of the tank, occlude the vessels inside. The unrotated version together with the 85% mixing maps can be found in Appendix A.4.

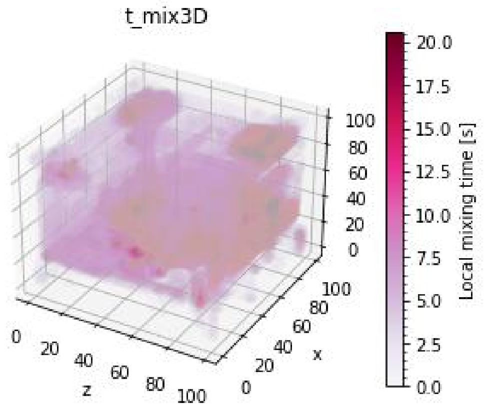

Figure 4.22: Experimental data 3D non-normalised (92%) mixing map

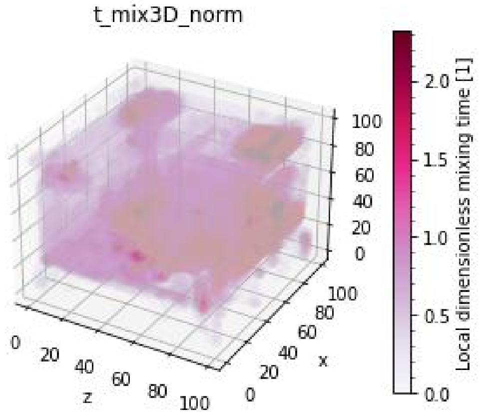

Figure 4.23: Experimental data (92%) 3D normalised mixing map

The distribution of mixing times observed appears to meet the general expectations of the mixing trends within the tank. The areas surrounding the impeller mix the fastest, while corners and edges require a longer duration. The tracer was introduced beneath the surface at approximately one-third of the liquid depth. This injection instantly propels the tracer towards the tank's bottom and towards the impeller, which rationalizes the shorter mixing times in the lower regions and the longer ones at the top. This is due to the necessity for the tracer to be initially drawn from the tank's bottom and redistributed to the upper portions

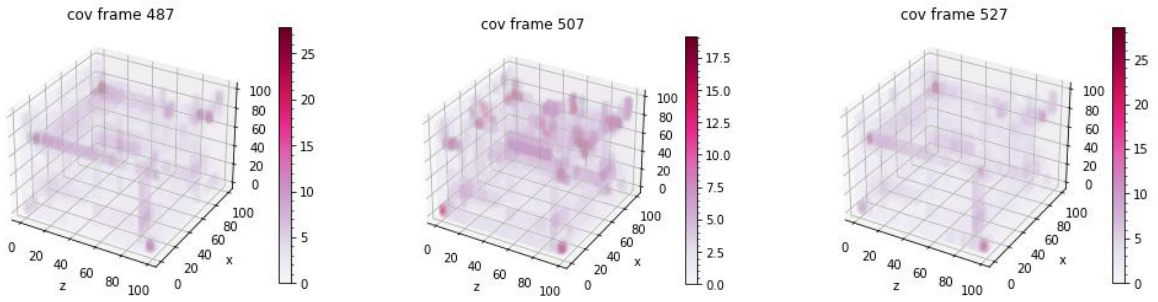

(a) Local CoV, t=19.2 [s] **(b)** Local CoV,t=20 [s] **(c)** Local CoV, t=20.8 [s]

Figure 4.24: Local CoV in final grids of experimental data reconstruction

The anomalous nature of the artifacts is particularly noticeable in the local CoV plots of the final timesteps, with many point-like objects clustered around the water's surface. In a manner similar to the synthetic data, we can observe that the tank edges deviate most from the overall volume. Nevertheless, the CoV doesn't decrease in the final two seconds within these regions, indicating that this can't be attributed to less intensive corner mixing, but rather to the flaws in the projections.

5

Conclusions & Recommendations

In this final chapter, the developed methodology and obtained results are evaluated and linked to the research questions posed in chapter 2.3. The project was of exploratory nature, aimed to create from scratch both an experimental setup and software implementation of the tomographic reconstruction techniques for mixing quantification from a highly limited number of views, therefore leaving plenty of room for further development.

5.1. Conclusions

To answer the first research question the following obstacles were identified in three-dimensional dynamic tracer distribution reconstruction:

- The constantly changing tracer volume data needs to be processed in a sequence to maintain the continuity between the frames. This leads to computationally expensive reconstruction with limited possibilities of parallelization
- Occlusion - the fewer angles used in the reconstruction the less information about the tracer behind the light absorbing objects such as impeller is available. Moreover with the highly irregular shapes of the tracer ”cloud”, zones of high concentration can occlude the regions of minimal concentration leading to non-smooth profiles along the ray path.
- Ghosting and its similarity to the edge zones of spreading tracer. Ghosting presence is inversely proportional to the number of projections used. The filtering techniques used to eliminate this effect can change the tracer dispersion. During attempts to remove ghosting, zones of low attenuation can also be filtered.
- Managing sizeable matrices representing the volume and projections. As the number of projections, frame rate, and resolution increase, data handling becomes increasingly difficult. Contrary, collecting good-quality data at a high frame rate leads to less significant changes between frames and easier reconstruction. The projections and reconstruction matrices downsizing facilitate the use of a higher frame rate and a number of projections at a cost of reconstruction resolution.
- The complication of light-path modelling. The project made a significant simplification by assuming a pencil beam for the forward problem. Violating some of these assumptions leads to artifacts or noise in the projections. Therefore, if a calibration-free approach is employed for solving the forward problem, the imaging environment should closely adhere to ideal conditions. If only absorption is assumed as the sole modifier of beam intensity, light scattering or refraction can cause substantial errors.

The second research question addressed the optimal construction of experimental equipment to best utilize data from three cameras recording a back-lit stirred tank. Although the design leading concepts such as minimal aperture and proper detector-to-light source distance for effective collimation targeted this question, the final experimental setup did not meet these initial expectations due to the camera type switch. Since these assumptions went untested, we can only discern the outcomes of their deviation, which led to disorderly projections abundant with artifacts like light refraction on the tank edges and surface, partial reflections on the tank side, and geometric distortion from camera misalignment, among others. Nevertheless, when confined to three points of view, the concept of axis alignment proved advantageous. It further streamlined both forward and back-projection implementation, thus negating the need to store the projection operator for each view. The use of square LED panels as a light source needs to be reconsidered as in the case of larger tanks and more viewing points fitting the illumination components around the tank while maintaining the detector-source line of view is challenging.

The third research question, concerning the isolation of ray-dye interactions from raw images, was addressed by developing a comprehensive pre-processing pipeline. This procedure, which included steps for brightness normalization, colour inversion, the use of neural networks for impeller removal, background subtraction based on image similarity metrics, and finally, frame cutting and resizing, resulted in an accurate representation of the tracer. However, during the quantification of mixing, it became clear that the approach to submerged object handling requires refinement. The inconsistent number of pixels representing the impeller between time frames was associated with instability in concentration and challenges in reconstructing the impeller shape.

At last the issue of how to obtain relevant mixing information from projections and reconstructed volumetric data has to be addressed. Extending the [8] post-processing to the 3rd dimension results in a meaningful description of the mixing process as it compresses both spatial and temporal information into a single matrix easy to visualize. However, the reconstruction and projections' quality needs to be significantly improved in order to create precise three-dimensional mixing maps. Monitoring the local Coefficient of Variance relating the sliding cube to the bulk of the mixing domain facilitates further insights into the mixing evolution. The three-point setup might not be sufficient for quantitative mixing time distribution prediction, although, for qualitative assessment of relative mixing intensity and dead zone identification, it could suffice if the experimental conditions were closer to the assumed ones.

5.2. Recommendations

The employment of light-based tomographic reconstruction for evaluating mixing presents potential, but the methodology introduced in this study necessitates significant refinement and validation to yield reliable and impactful results. Moreover, due to the limitations of visible light use as an imaging beam, other techniques such as Electrical Resistance Tomography might be more promising ways of the 3D mixing assessment. To continue the development of the presented methodology, following areas of improvement should be of interest:

- Introduction of more viewpoints should be attempted as collecting projections from more angles is the most straightforward way of improving reconstruction. However, increasing the number of projections would require modifications to both the designed equipment as well as the forward and backward models. Sensitivity analysis of reconstruction quality dependency on viewpoints number could be attempted using synthetic data to find a minimum number of cameras allowing the quantitative mixing assessment.
- Using proper cameras with optics facilitating the approximation of the pencil beam to fully demonstrate the current methodology potential and limitations
- The substitution of the black impeller with a transparent one may be considered, as it could reduce the information loss resulting from occlusion. Given its complex geometry and movement, the interaction of the impeller with light needs careful investigation. While focusing on occlusion reduction, such a change may inadvertently introduce more measuring noise due to the scattering, reflection, and refraction of light.
- Constraining the number of pixels used in impeller removal to increase the calculation stability. It could be done by imposing the constant number of 0 valued pixels to be used to represent the impeller during the prediction step of the segmentation algorithm (YOLOv7 currently).
- An attempt at reconstruction with more complicated tank geometry would be interesting. In theory, the same approach could be utilised by simply submerging the target tank in the bigger cube for refractive index matching and maintaining the forward problem simplicity. Also, the utilisation of specific geometry masks could be incorporated into the back projection.

- Calibration pattern utilisation for solving the forward problem to more accurately describe the ray paths
- The more comprehensive forward model implementation such as radiative transport equation based approach to capture more realistically the light propagation through the tank.
- The implemented reconstruction is simplistic. The use of more complicated algorithms or gradient-based optimisation should be attempted. Moreover, single-thread CPU operations dominate the calculations and reconstruction data is saved into CSV timestep files leading to inefficient use of the computational resources. The potential for significant improvement in calculation speed and reconstruction resolution lies in the parallelization of calculations and shifting of computations to the GPU.

References

[1] Mohammed Abdulameer Aljanabi et al. “Design of a hybrid measure for image similarity: a statistical, algebraic, and information-theoretic approach”. In: *European Journal of Remote Sensing* 52.sup4 (2019), pp. 2–15. DOI: `10.1080/22797254.2019.1628617`. URL: `https://doi.org/10.1080/22797254.2019.1628617`.

[2] Ashraf Amanullah, Barry C. Buckland, and Alvin W. Nienow. “Mixing in the Fermentation and Cell Culture Industries”. In: *Handbook of Industrial Mixing*. John Wiley Sons, Ltd, 2003. Chap. 18, pp. 1071–1170. ISBN: 9780471451457. DOI: `https://doi.org/10.1002/0471451452.ch18`. eprint: `https://onlinelibrary.wiley.com/doi/pdf/10.1002/0471451452.ch18`. URL: `https://onlinelibrary.wiley.com/doi/abs/10.1002/0471451452.ch18`.

[3] Simon Arridge and John Schotland. “TOPICAL REVIEW: Optical tomography: forward and inverse problems”. In: *Inverse Problems* 25 (Dec. 2009). DOI: `10.1088/0266-5611/25/12/123010`.

[4] Henry Barrington et al. “Computer Vision for Kinetic Analysis of Lab- and Process-Scale Mixing Phenomena”. In: *Organic Process Research & Development* 26.11 (2022), pp. 3073–3088. DOI: `10.1021/acs.oprd.2c00216`. eprint: `https://doi.org/10.1021/acs.oprd.2c00216`. URL: `https://doi.org/10.1021/acs.oprd.2c00216`.

[5] David A. R. Brown et al. “Experimental Methods”. In: *Handbook of Industrial Mixing*. John Wiley & Sons, Ltd, 2003. Chap. 4, pp. 145–256. ISBN: 9780471451457. DOI: `https://doi.org/10.1002/0471451452.ch4`. eprint: `https://onlinelibrary.wiley.com/doi/pdf/10.1002/0471451452.ch4`. URL: `https://onlinelibrary.wiley.com/doi/abs/10.1002/0471451452.ch4`.

[6] Martin Eberhart, Stefan Loehle, and Philipp Offenhäuser. “3-D visualization of transparent fluid flows from snapshot light field data”. In: *Experiments in Fluids* 62.8, 165 (Aug. 2021), p. 165. DOI: `10.1007/s00348-021-03255-y`.

[7] J.B. Fasano and William Penney. “Avoid Blending Mix-Up”. In: *Chemical Engineering Progress* 87 (Oct. 1991), pp. 56–63.

[8] J. Fitschen et al. “Novel evaluation method to determine the local mixing time distribution in stirred tank reactors”. In: *Chemical Engineering Science: X* 10 (2021), p. 100098. ISSN: 2590-1400. DOI: `https://doi.org/10.1016/j.cesx.2021.100098`. URL: `https://www.sciencedirect.com/science/article/pii/S2590140021000113`.

[9] Dominik Fleischmann and Franz Boas. “Computed tomography—old ideas and new technology”. In: *European radiology* 21 (Mar. 2011), pp. 510–7. DOI: `10.1007/s00330-011-2056-z`.

[10] C.L Ford. “A Simple Dye-Based Tomography Method to Estimate Component-Fluid Distributions in Laminar Mixing Problems”. In: *Experimental Techniques* (2022). DOI: `10.1088/1361-6501/ac92a1`.

[11] F. Garcia-Ochoa, V.E. Santos, and E. Gomez. “2.15 - Stirred Tank Bioreactors”. In: *Comprehensive Biotechnology (Second Edition)*. Ed. by Murray Moo-Young. Second Edition. Burlington: Academic Press, 2011, pp. 179–198. ISBN: 978-0-08-088504-9. DOI: `https://doi.org/10.1016/B978-0-08-088504-9.00108-2`. URL: `https://www.sciencedirect.com/science/article/pii/B9780080885049001082`.

[12] Richard Gordon, Robert Bender, and Gabor T. Herman. “Algebraic Reconstruction Techniques (ART) for three-dimensional electron microscopy and X-ray photography”. In: *Journal of Theoretical Biology* 29.3 (1970), pp. 471–481. ISSN: 0022-5193. DOI: `https://doi.org/10.1016/0022-5193(70)90109-8`. URL: `https://www.sciencedirect.com/science/article/pii/0022519370901098`.

[13] Samuel J. Grauer et al. “Volumetric emission tomography for combustion processes”. In: *Progress in Energy and Combustion Science* 94 (2023), p. 101024. ISSN: 0360-1285. DOI: `https://doi.org/10.1016/j.pecs.2022.101024`. URL: `https://www.sciencedirect.com/science/article/pii/S0360128522000338`.

[14] James Gregson et al. “Stochastic tomography and its applications in 3D imaging of mixing fluids”. In: *ACM Transactions on Graphics (TOG)* 31.4 (2012), pp. 1–10.

[15] H. Hartmann, J. J. Derksen, and H. E. A. van den Akker. “Mixing times in a turbulent stirred tank by means of LES”. In: *AIChE Journal* 52.11 (2006), pp. 3696–3706. DOI: `https://doi.org/10.1002/aic.10997`. eprint: `https://aiche.onlinelibrary.wiley.com/doi/pdf/10.1002/aic.10997`. URL: `https://aiche.onlinelibrary.wiley.com/doi/abs/10.1002/aic.10997`.

[16] Ramesh R. Hemrajani and Gary B. Tatterson. “Mechanically Stirred Vessels”. In: *Handbook of Industrial Mixing: Science and Practice*. John Wiley & Sons, 2004. Chap. 6, pp. 345–364.

[17] Bin Hu et al. “Development of an X-ray computed tomography (CT) system with sparse sources: Application to three-phase pipe flow visualization”. In: *Experiments in Fluids* 39 (Oct. 2005), pp. 667–678. DOI: `10.1007/s00348-005-1008-2`.

[18] Clément Jailin and Stéphane Roux. “Dynamic Tomographic Reconstruction of Deforming Volumes”. In: *Materials* 11.8 (2018). ISSN: 1996-1944. DOI: `10.3390/ma11081395`. URL: `https://www.mdpi.com/1996-1944/11/8/1395`.

[19] Avinash C. Kak and Malcolm Slaney. “Introduction”. In: *Principles of Computerized Tomographic Imaging*. Society for Industrial and Applied Mathematics, 2001, pp. 1–3. ISBN: 0879421983.

[20] Avinash C. Kak and Malcolm Slaney. *Principles of Computerized Tomographic Imaging*. Society for Industrial and Applied Mathematics, 2001. DOI: `10.1137/1.9780898719277`. eprint: `https://epubs.siam.org/doi/pdf/10.1137/1.9780898719277`. URL: `https://epubs.siam.org/doi/abs/10.1137/1.9780898719277`.

[21] Suzanne M. Kresta et al. “Introduction: A Technical Definition of Mixing”. In: *Advances in Industrial Mixing: A Companion to the Handbook of Industrial Mixing*. Wiley, Nov. 2015, pp. 1–9. ISBN: 9780470523827.

[22] Alena Kukukova, Joelle Aubin, and Suzanne M. Kresta. “A new definition of mixing and segregation: Three dimensions of a key process variable”. In: *Chemical Engineering Research and Design* 87.4 (2009). 13th European Conference on Mixing: New developments towards more efficient and sustainable operations, pp. 633–647. ISSN: 0263-8762. DOI: `https://doi.org/10.1016/j.cherd.2009.01.001`. URL: `https://www.sciencedirect.com/science/article/pii/S0263876209000021`.

[23] Jaime Moreno Juez, Riccardo Artoni, and Bogdan Cazacliu. “Monitoring of concrete mixing evolution using image analysis”. In: *Powder Technology* 305 (2017), pp. 477–487. ISSN: 0032-5910. DOI: `https://doi.org/10.1016/j.powtec.2016.10.008`. URL: `https://www.sciencedirect.com/science/article/pii/S0032591016306908`.

[24] Volodymyr Mosorov. “24 - Applications of tomography in mixing process”. In: *Industrial Tomography (Second Edition)*. Ed. by Mi Wang. Second Edition. Woodhead Publishing Series in Electronic and Optical Materials. Woodhead Publishing, 2022, pp. 773–798. ISBN: 978-0-12-823015-2. DOI: `https://doi.org/10.1016/B978-0-12-823015-2.00008-X`. URL: `https://www.sciencedirect.com/science/article/pii/B978012823015200008X`.

[25] R.F. Mudde. “Time-Resolved X-Ray Tomography of a Fluidized Bed”. In: *Powder Technology - POWDER TECHNOL* 199 (Oct. 2008). DOI: `10.1016/j.powtec.2009.04.021`.

[26] Fan Peng et al. “Assessment of imaging models for volumetric tomography of fluid flows”. In: *Measurement* 204 (2022), p. 112174. ISSN: 0263-2241. DOI: `https://doi.org/10.1016/j.measurement.2022.112174`. URL: `https://www.sciencedirect.com/science/article/pii/S0263224122013707`.

[27] Tigran Petrosyan. *Introduction to the coco dataset*. Oct. 2021. URL: `https://opencv.org/blog/2021/10/12/introduction-to-the-coco-dataset/#:~:text=Key%5C%20points-,What%5C%20is%5C%20COCO%5C%3F,over%5C%201.5%5C%20million%5C%20object%5C%20instances.`.

[28] M. J. D. Powell. “An efficient method for finding the minimum of a function of several variables without calculating derivatives”. In: *The Computer Journal* 7.2 (Jan. 1964), pp. 155–162. ISSN: 0010-4620. DOI: `10.1093/comjnl/7.2.155`. eprint: `https://academic.oup.com/comjnl/article-pdf/7/2/155/959784/070155.pdf`. URL: `https://doi.org/10.1093/comjnl/7.2.155`.

[29] *Roboflow*. 2023. URL: `https://app.roboflow.com/` (visited on 05/01/2023).

[30] Darius Rückert et al. “NeAT: Neural Adaptive Tomography”. In: *ACM Trans. Graph.* 41.4 (July 2022). ISSN: 0730-0301. DOI: `10.1145/3528223.3530121`. URL: `https://doi.org/10.1145/3528223.3530121`.

[31] David Sanned et al. “Arbitrary position 3D tomography for practical application in Combustion Diagnostics”. In: *Measurement Science and Technology* 33 (Sept. 2022). DOI: `10.1088/1361-6501/ac92a1`.

[32] Chien-Yao Wang, Alexey Bochkovskiy, and Hong-Yuan Mark Liao. “YOLOv7: Trainable bag-of-freebies sets new state-of-the-art for real-time object detectors”. In: (2022). DOI: `https://doi.org/10.48550/arXiv.2207.02696`. arXiv: `2207.02696 [cs.CV]`.

[33] Zhou Wang et al. “Image Quality Assessment: From Error Visibility to Structural Similarity”. In: *Image Processing, IEEE Transactions on* 13 (May 2004), pp. 600–612. DOI: `10.1109/TIP.2003.819861`.

[34] Martin Willemink and Peter Noël. “The evolution of image reconstruction for CT—from filtered back projection to artificial intelligence”. In: *European Radiology* 29 (Oct. 2018). DOI: `10.1007/s00330-018-5810-7`.

[35] Xiaogang Yang et al. “A hybrid tomographic reconstruction algorithm for high speed X-ray tomography”. In: *Computer Physics Communications* 196 (2015), pp. 27–35. ISSN: 0010-4655. DOI: `https://doi.org/10.1016/j.cpc.2015.05.010`. URL: `https://www.sciencedirect.com/science/article/pii/S0010465515001885`.

[36] Jiafeng Yao and Masahiro Takei. “Application of Process Tomography to Multiphase Flow Measurement in Industrial and Biomedical Fields - A Review”. In: *IEEE Sensors Journal* 17 (Mar. 2017), pp. 8196–8205. DOI: `10.1109/JSEN.2017.2682929`.

A

A.1. Sythetic frames reconstruction errors

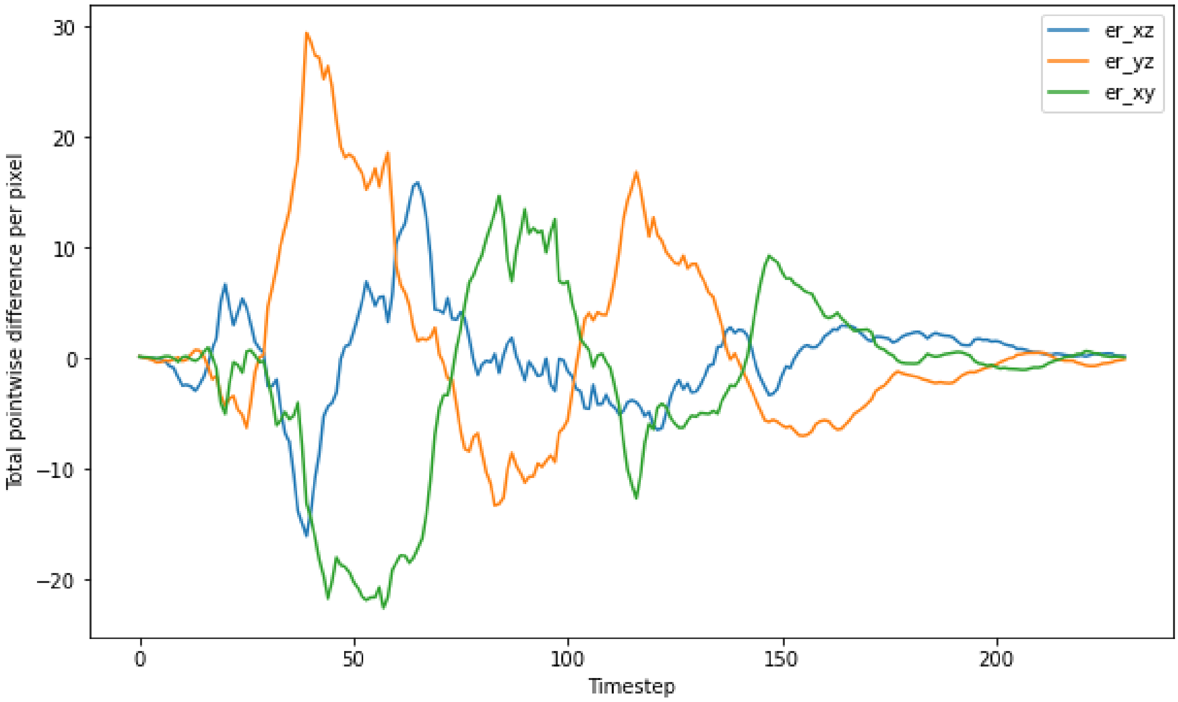

Figure A.1: View point-wise difference per pixel after synthetic data backward reconstruction

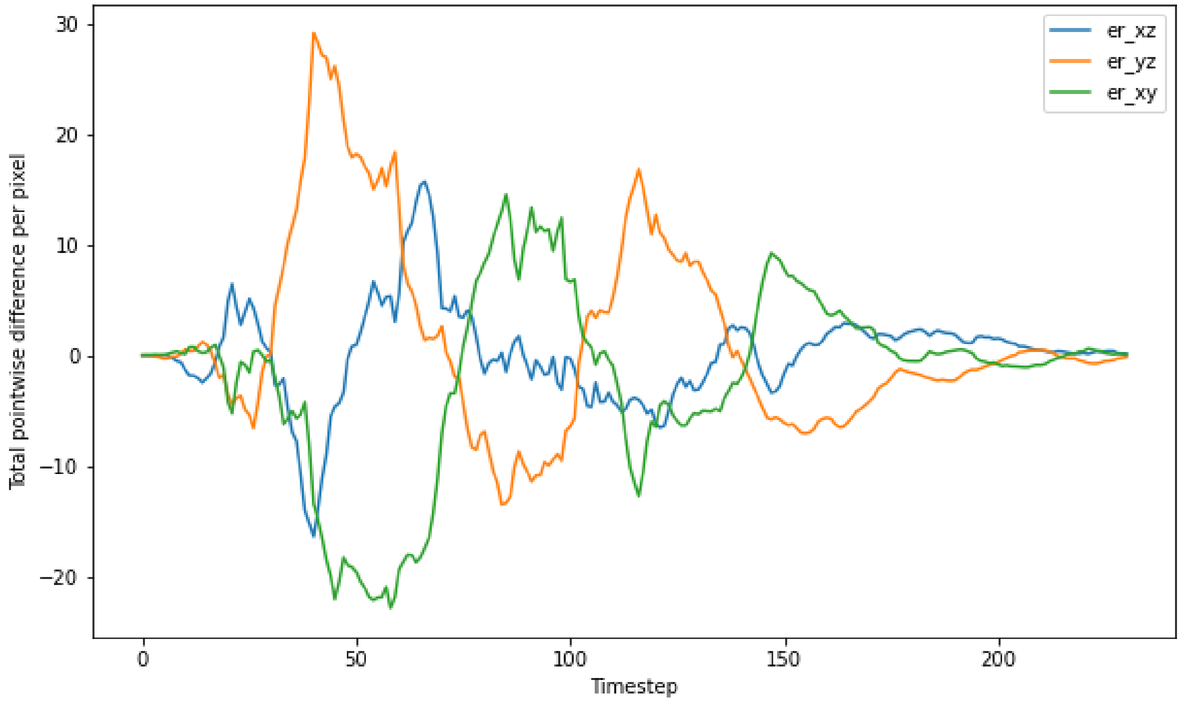

Figure A.2: View point-wise difference per pixel after synthetic data forward reconstruction

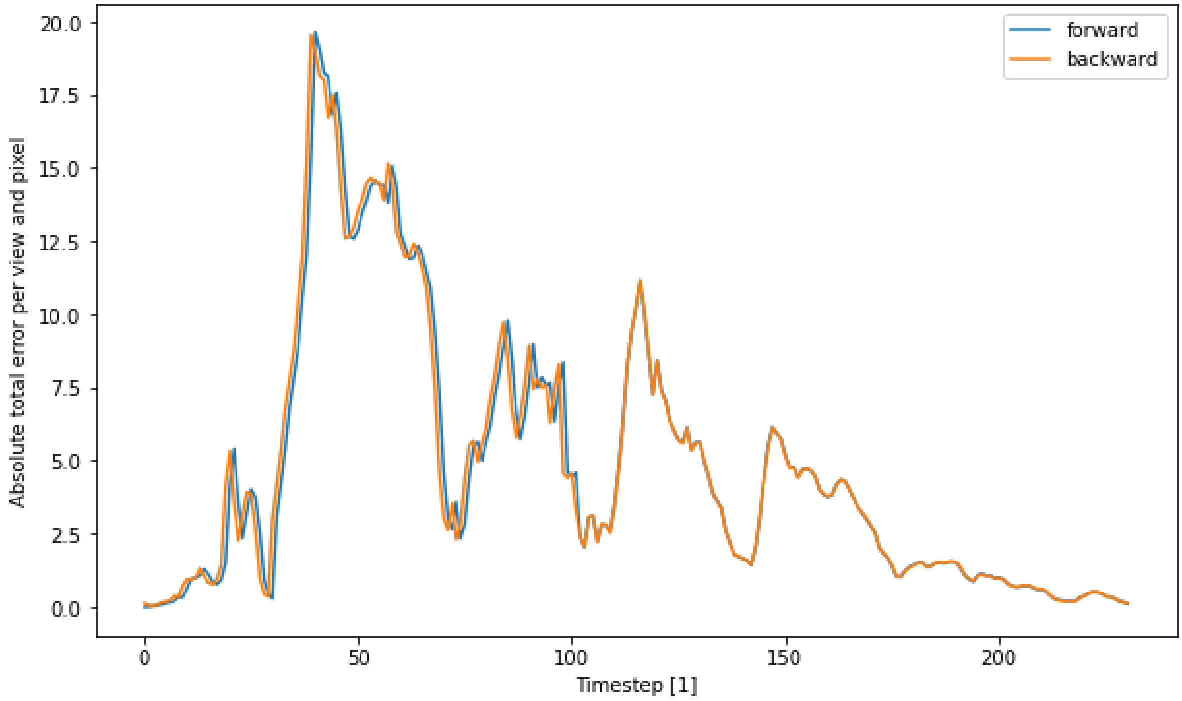

Figure A.3: Total absolute point-wise difference per pixel after synthetic data reconstruction

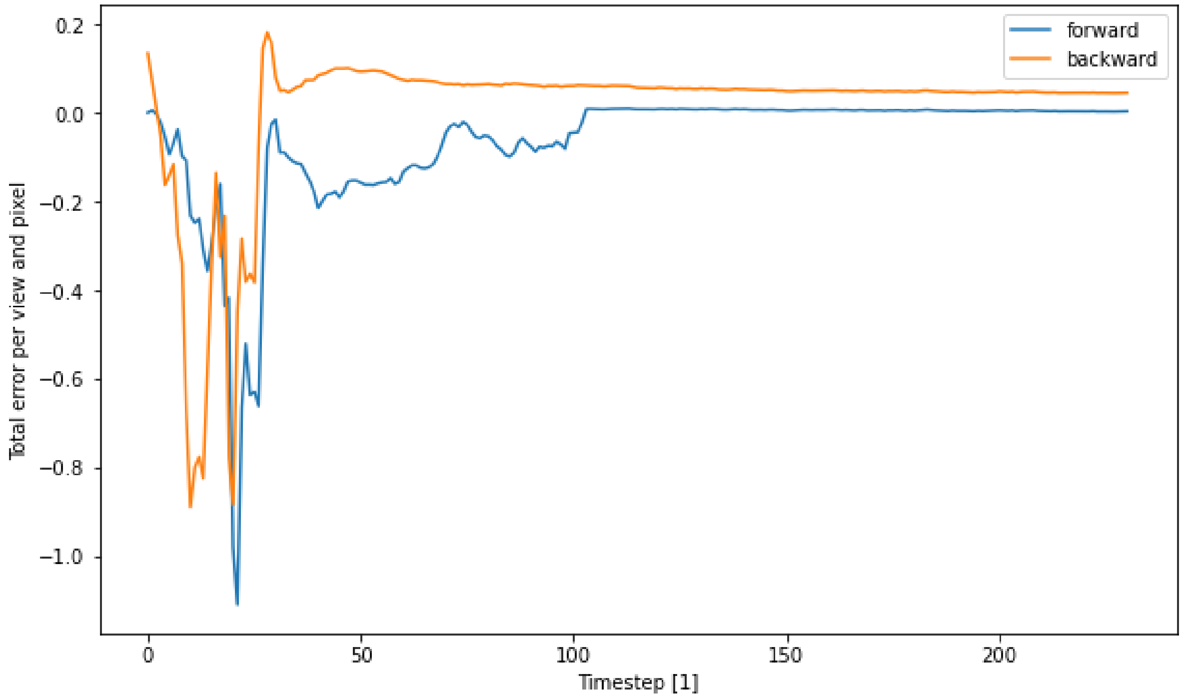

Figure A.4: Total point-wise difference per pixel after synthetic data reconstruction

A.2. Synthetic data reconstruction, reference & local CoV

In the following pages the visualizations of raw concentration data and 3D reconstruction from synthetic frames are presented, sampled at each second of the mixing process.

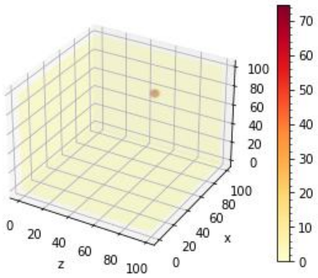

(a) Reconstruction, t=0[s]

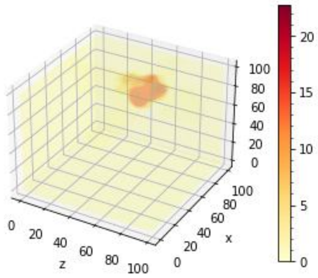

(b) Reconstruction, t=1[s]

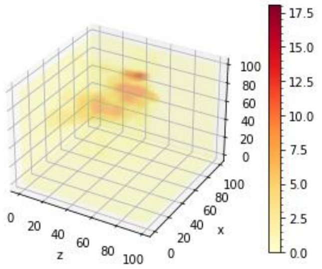

(c) Reconstruction, t=2[s]

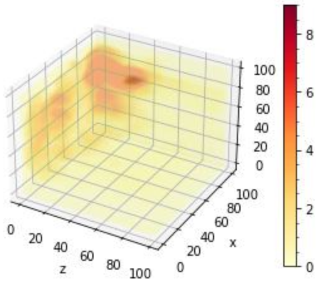

(d) Reconstruction, t=3[s]

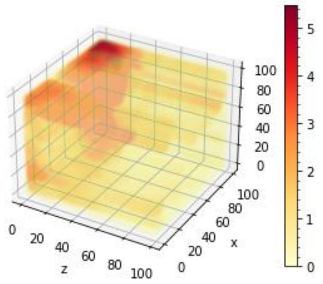

(e) Reconstruction, t=4[s]

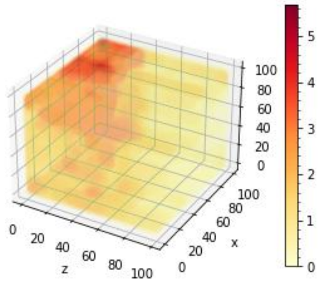

(f) Reconstruction, t=5[s]

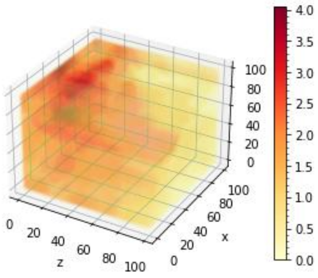

(g) Reconstruction, t=6[s]

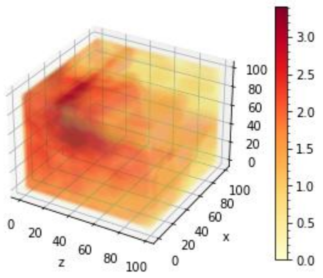

(h) Reconstruction, t=7[s]

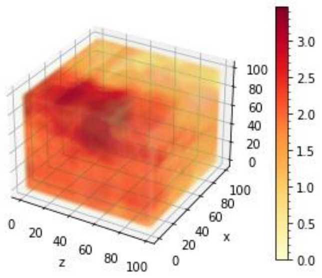

(i) Reconstruction, t=8[s]

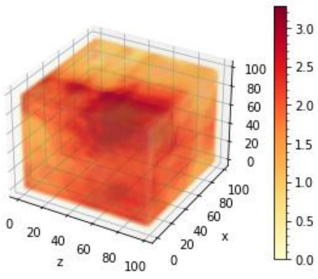

(j) Reconstruction, t=9[s]

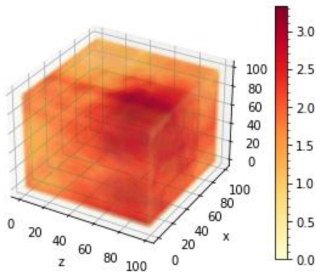

(k) Reconstruction, t=10[s]

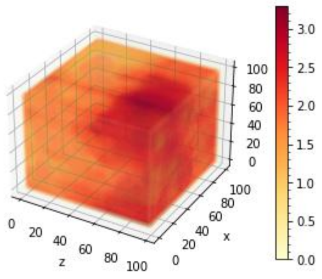

(l) Reconstruction, t=11[s]

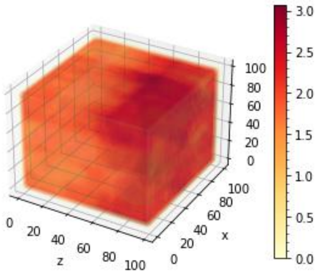

(m) Reconstruction, t=12[s]

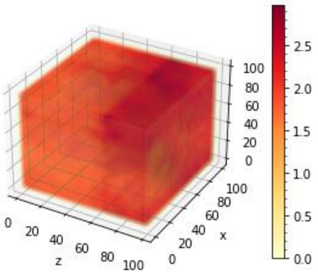

(n) Reconstruction, t=13[s]

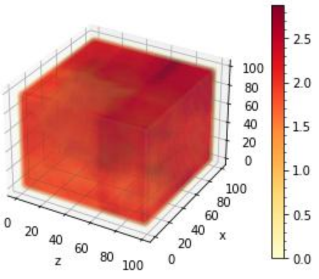

(o) Reconstruction, t=14[s]

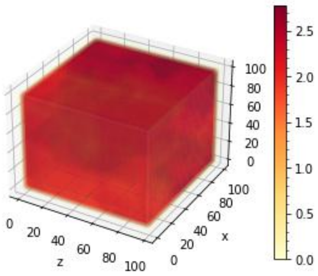

(a) Reconstruction, t=15[s]

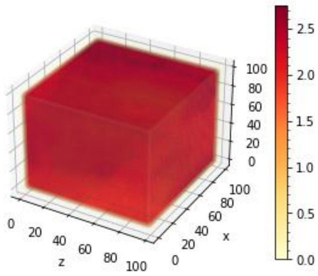

(b) Reconstruction, t=16[s]

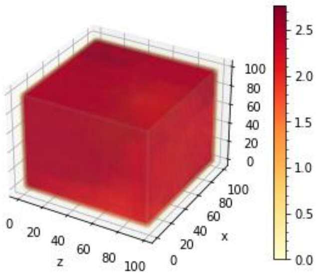

(c) Reconstruction, t=17[s]

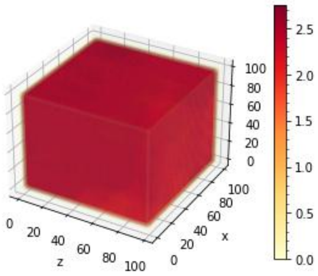

(d) Reconstruction, t=18[s]

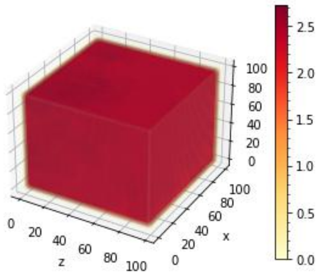

(e) Reconstruction, t=19[s]

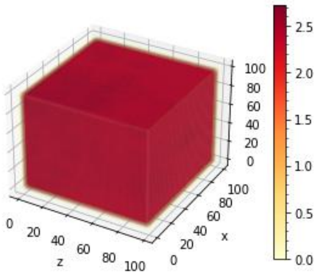

(f) Reconstruction, t=20[s]

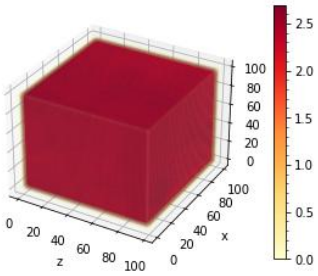

(g) Reconstruction, t=21[s]

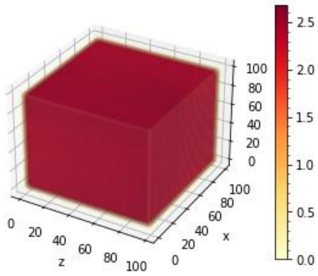

(h) Reconstruction, t=22[s]

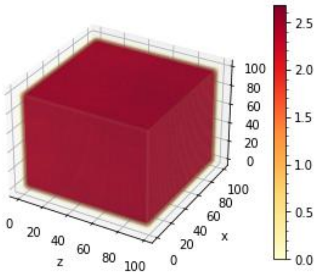

(i) Reconstruction, t=23[s]

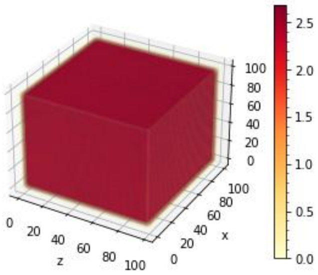

(j) Reconstruction, t=24[s]

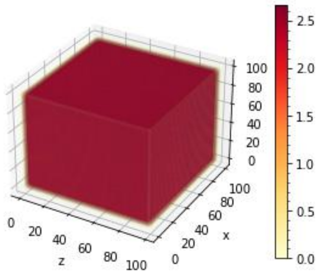

(k) Reconstruction, t=25[s]

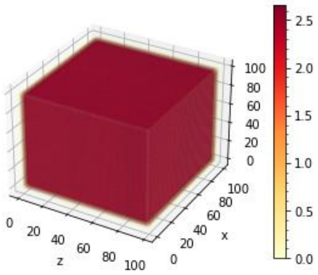

(l) Reconstruction, t=26[s]

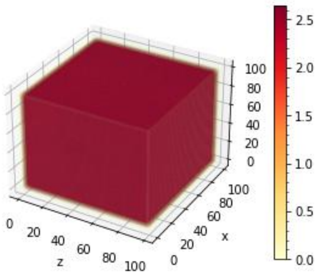

(m) Reconstruction, t=27[s]

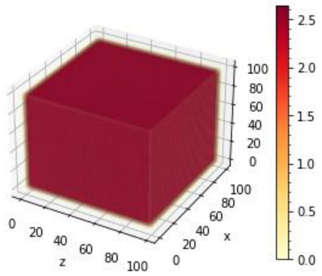

(n) Reconstruction, t=28[s]

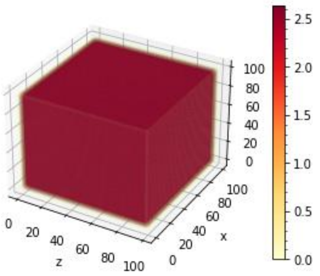

(o) Reconstruction, t=29[s]

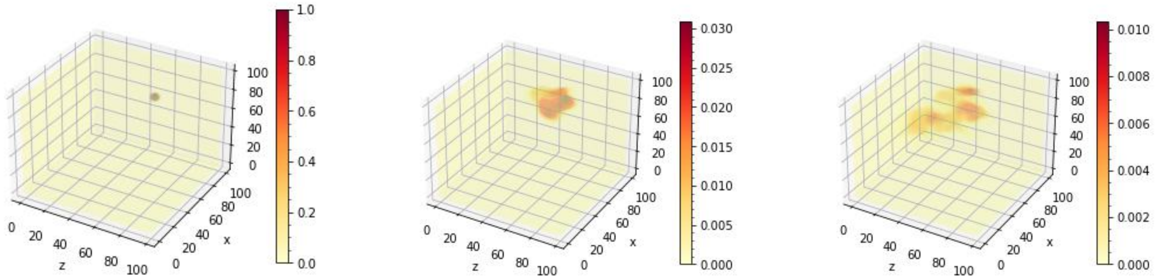

(a) Reference, t=0[s]

(b) Reference, t=1[s]

(c) Reference, t=2[s]

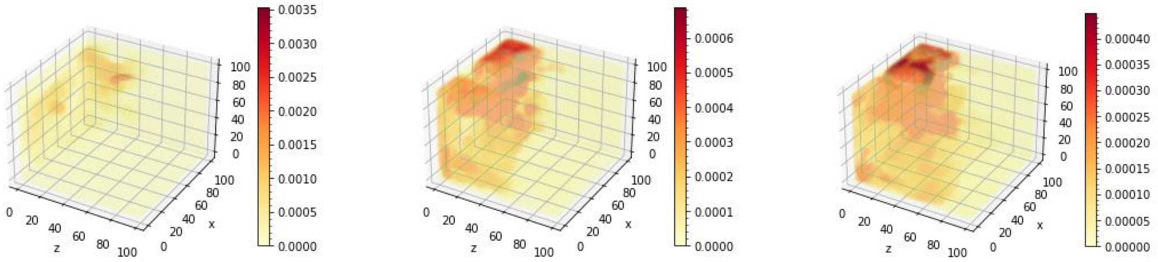

(d) Reference, t=3[s]

(e) Reference, t=4[s]

(f) Reference, t=5[s]

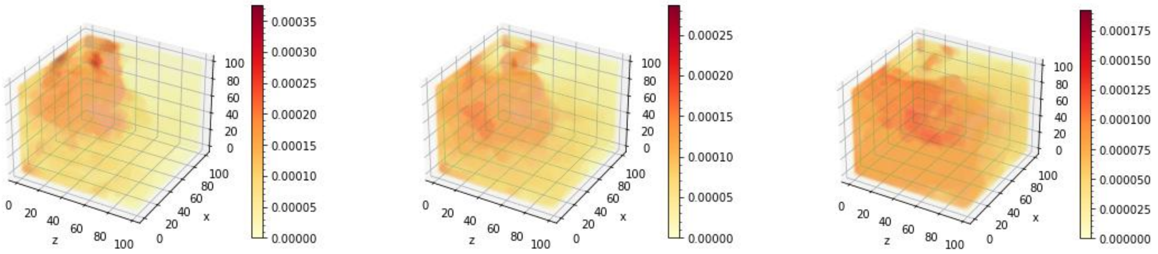

(g) Reference, t=6[s]

(h) Reference, t=7[s]

(i) Reference, t=8[s]

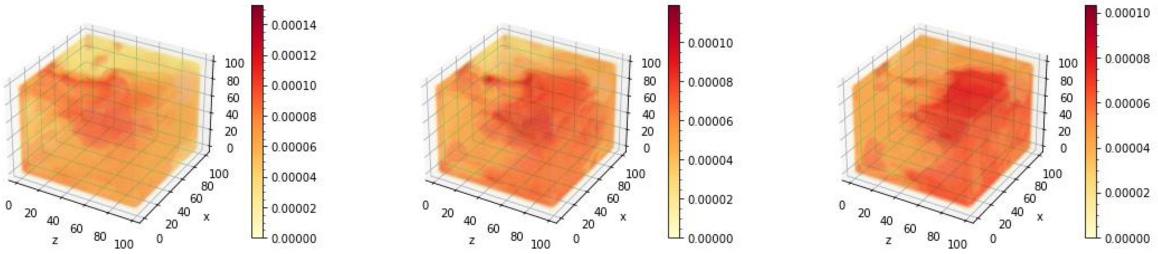

(j) Reference, t=9[s]

(k) Reference, t=10[s]

(l) Reference, t=11[s]

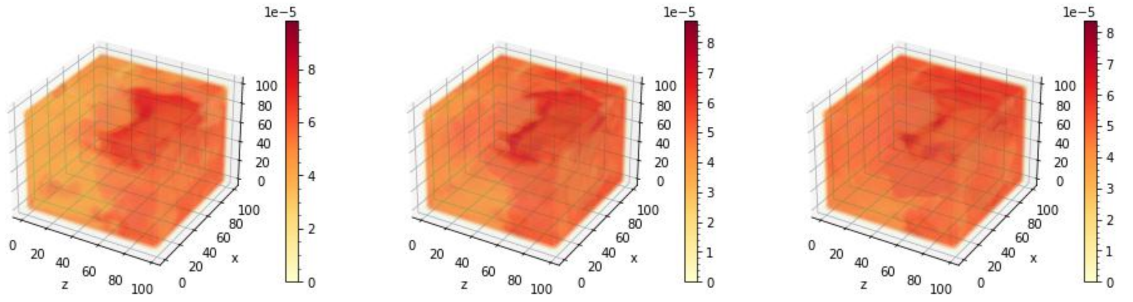

(m) Reference, t=12[s]

(n) Reference, t=13[s]

(o) Reference, t=14[s]

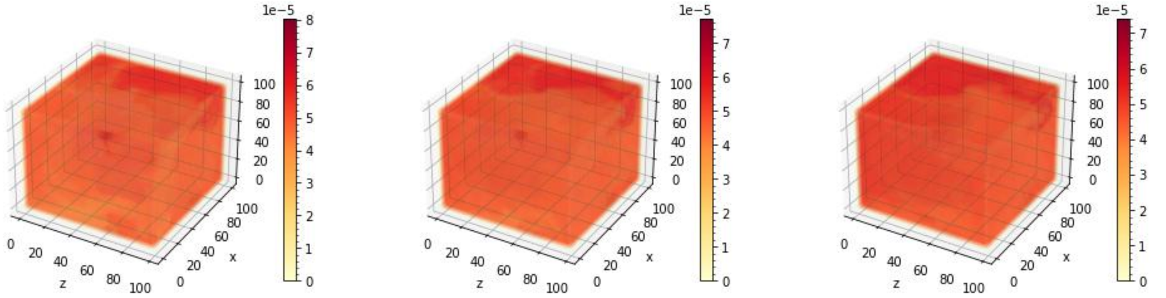

(a) Reference, t=15[s]

(b) Reference, t=16[s]

(c) Reference, t=17[s]

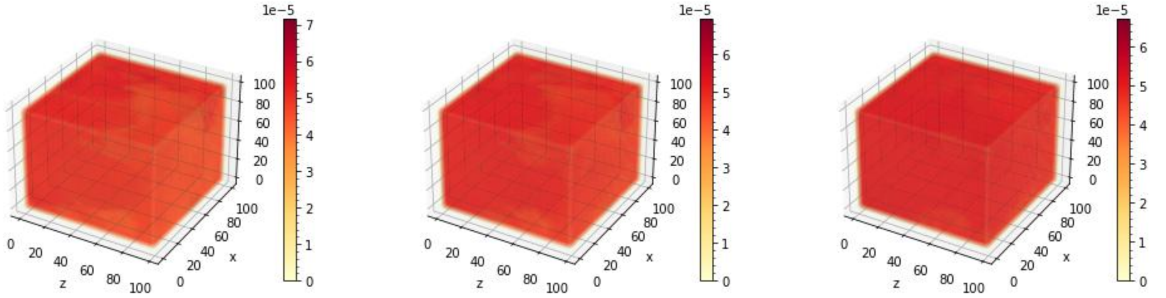

(d) Reference, t=18[s]

(e) Reference, t=19[s]

(f) Reference, t=20[s]

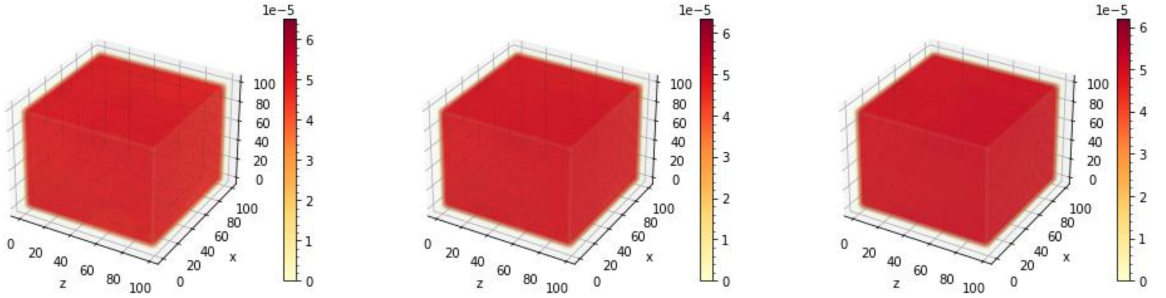

(g) Reference, t=21[s]

(h) Reference, t=22[s]

(i) Reference, t=23[s]

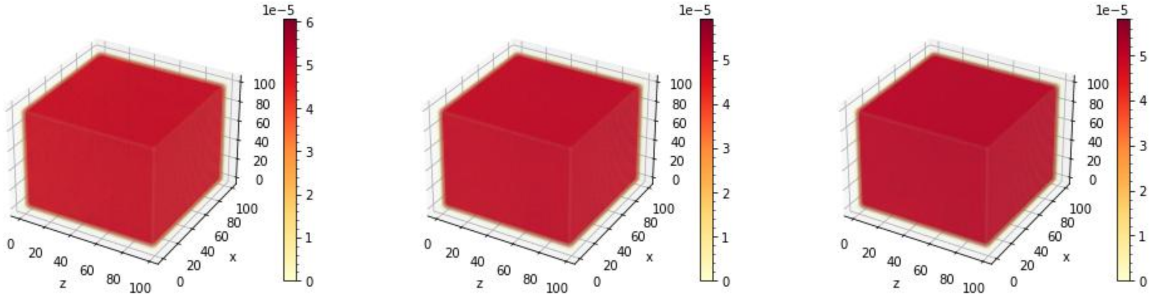

(j) Reference, t=24[s]

(k) Reference, t=25[s]

(l) Reference, t=26[s]

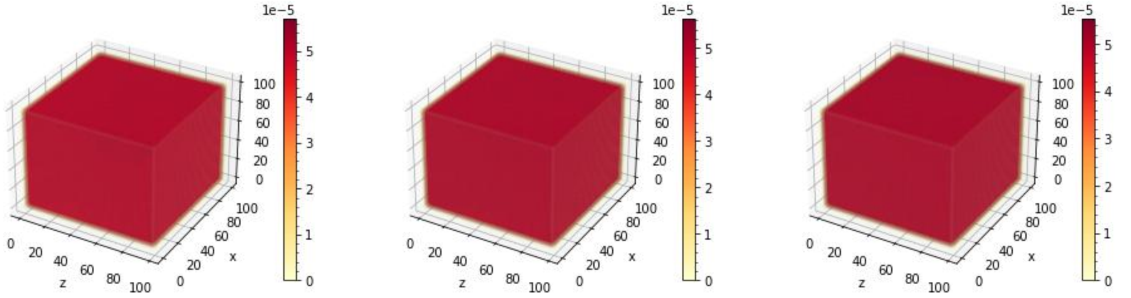

(m) Reference, t=27[s]

(n) Reference, t=28[s]

(o) Reference, t=29[s]

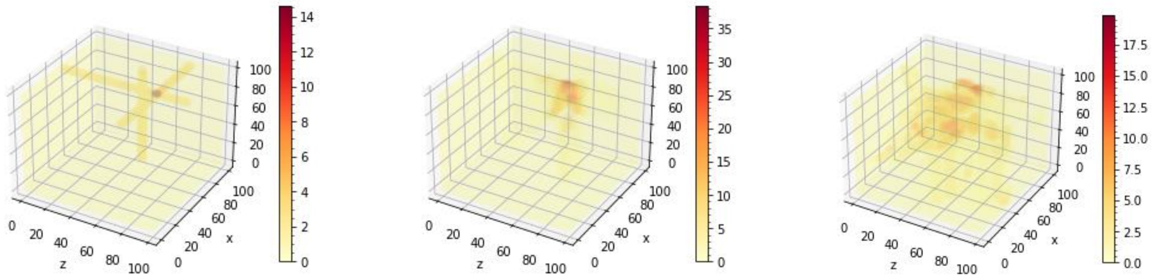

(a) Reconstruction with no ghosting filtering, t=0[s]

(b) Reconstruction with no ghosting filtering, t=1[s]

(c) Reconstruction with no ghosting filtering, t=2[s]

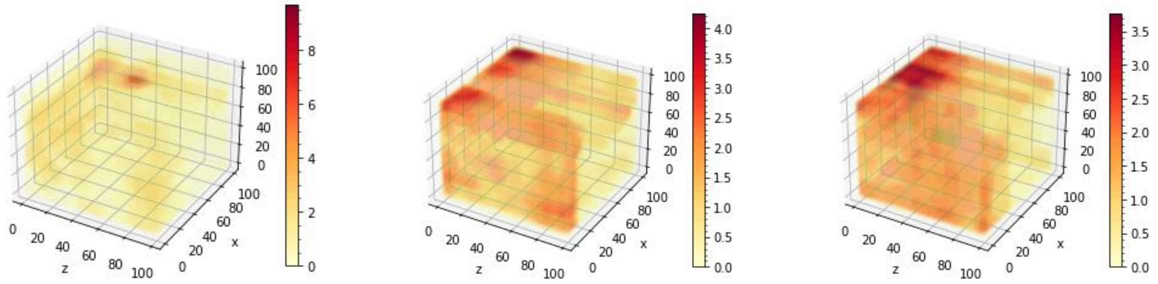

(d) Reconstruction with no ghosting filtering, t=3[s]

(e) Reconstruction with no ghosting filtering, t=4[s]

(f) Reconstruction with no ghosting filtering, t=5[s]

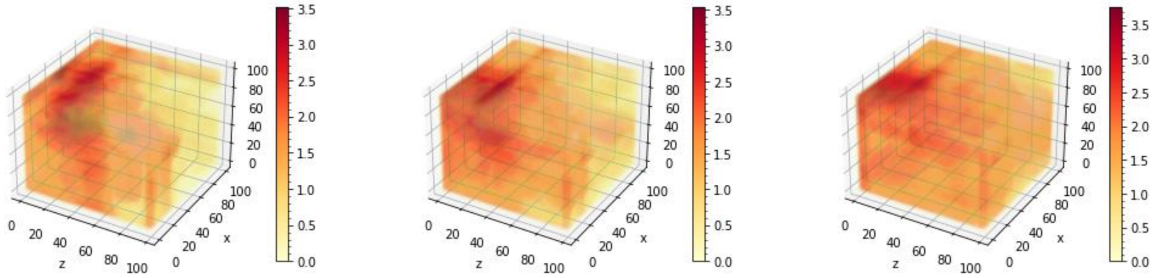

(g) Reconstruction with no ghosting filtering, t=6[s]

(h) Reconstruction with no ghosting filtering, t=7[s]

(i) Reconstruction with no ghosting filtering, t=8[s]

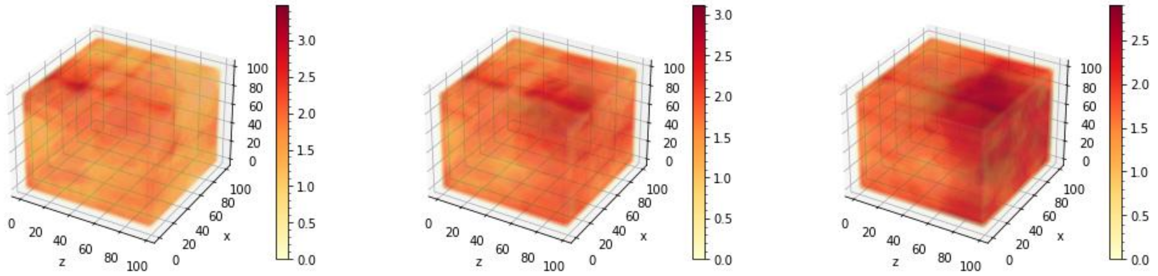

(j) Reconstruction with no ghosting filtering, t=9[s]

(k) Reconstruction with no ghosting filtering, t=10[s]

(l) Reconstruction with no ghosting filtering, t=11[s]

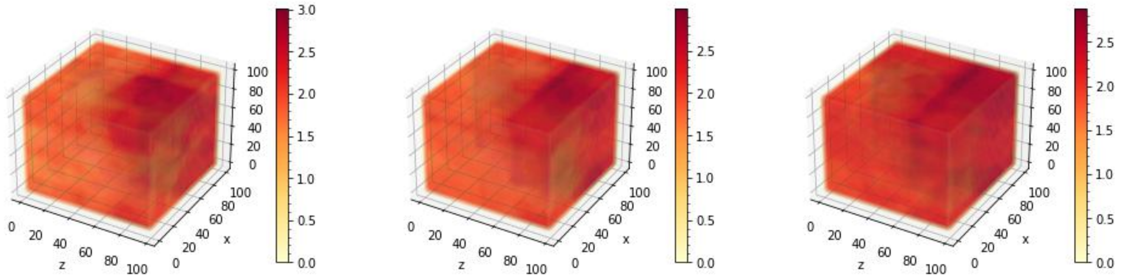

(m) Reconstruction with no ghosting filtering, t=12[s]

(n) Reconstruction with no ghosting filtering, t=13[s]

(o) Reconstruction with no ghosting filtering, t=14[s]

Figure A.9

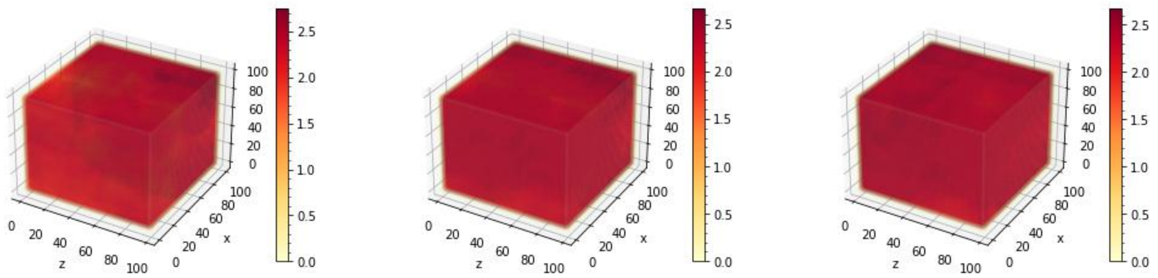

(a) Reconstruction with no ghosting filtering, t=15[s]

(b) Reconstruction with no ghosting filtering, t=16[s]

(c) Reconstruction with no ghosting filtering, t=17[s]

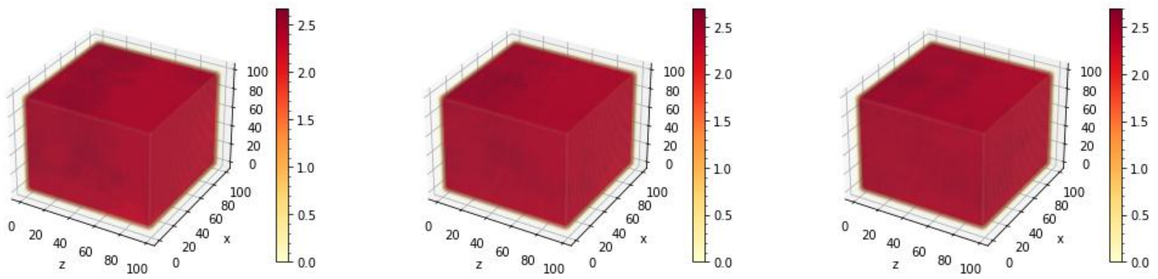

(d) Reconstruction with no ghosting filtering, t=18[s]

(e) Reconstruction with no ghosting filtering, t=19[s]

(f) Reconstruction with no ghosting filtering, t=20[s]

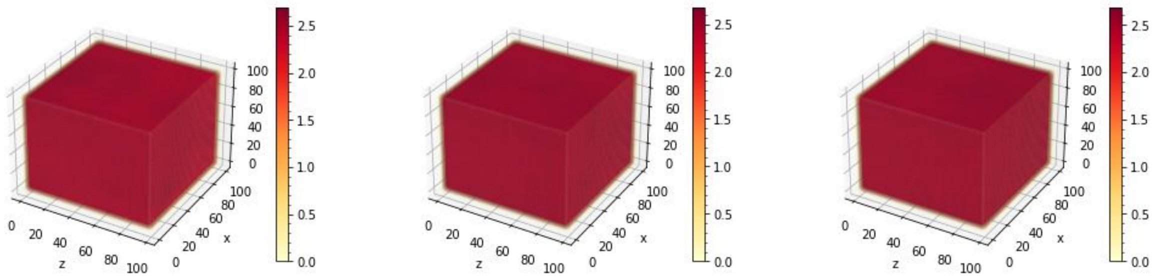

(g) Reconstruction with no ghosting filtering, t=21[s]

(h) Reconstruction with no ghosting filtering, t=22[s]

(i) Reconstruction with no ghosting filtering, t=23[s]

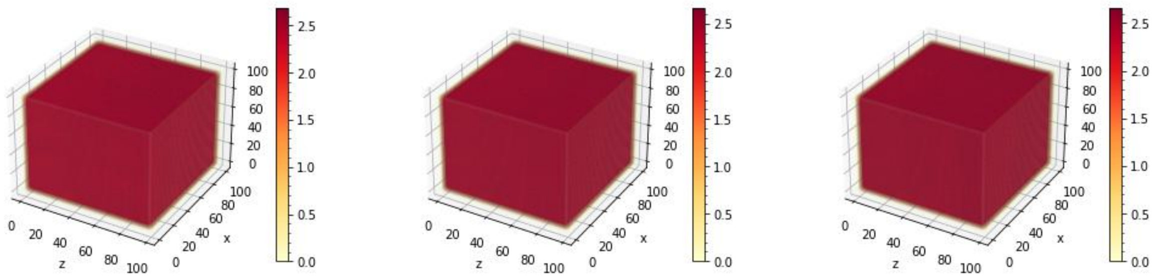

(j) Reconstruction with no ghosting filtering, t=24[s]

(k) Reconstruction with no ghosting filtering, t=25[s]

(l) Reconstruction with no ghosting filtering, t=26[s]

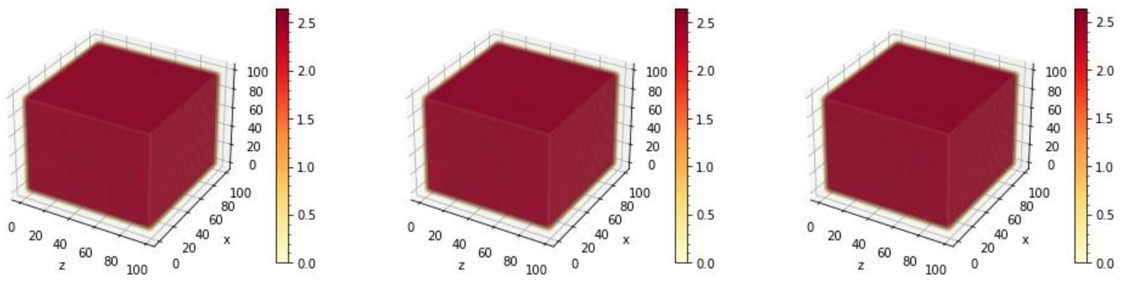

(m) Reconstruction with no ghosting filtering, t=27[s]

(n) Reconstruction with no ghosting filtering, t=28[s]

(o) Reconstruction with no ghosting filtering, t=29[s]

Figure A.10

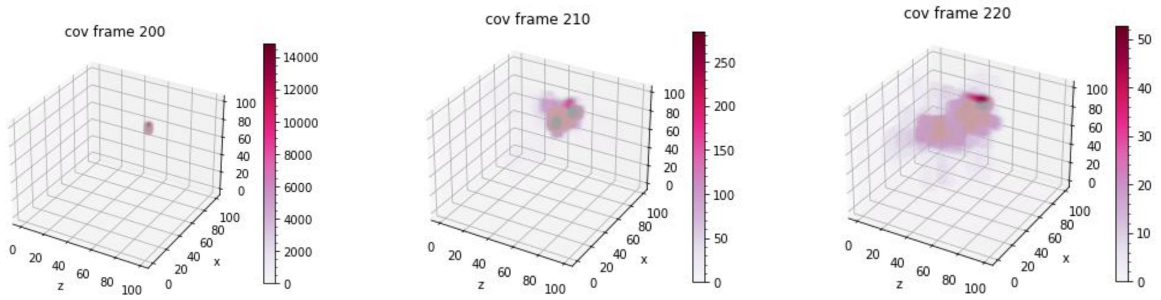

(a) Local CoV, t=0[s]

(b) Local CoV, t=1[s]

(c) Local CoV, t=2[s]

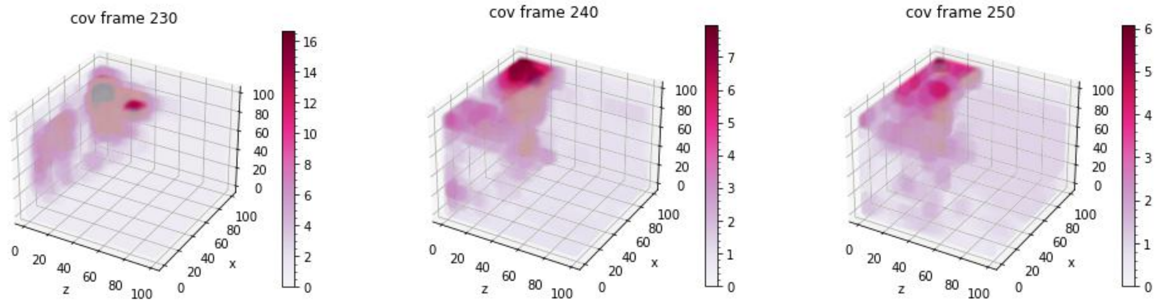

(d) Local CoV, t=3[s]

(e) Local CoV, t=4[s]

(f) Local CoV, t=5[s]

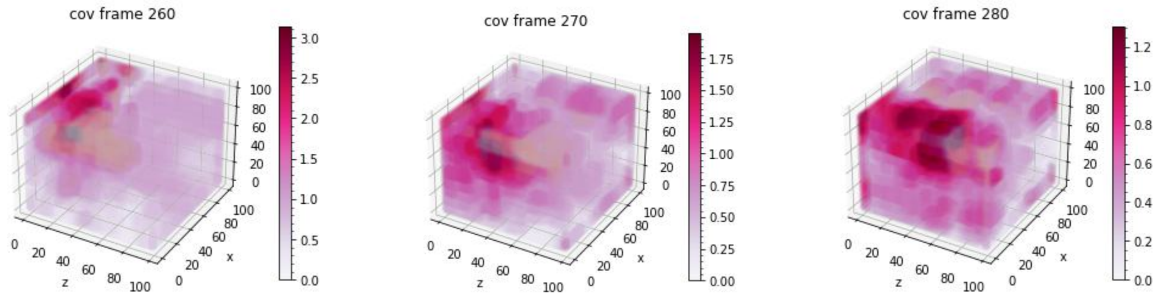

(g) Local CoV, t=6[s]

(h) Local CoV, t=7[s]

(i) Local CoV, t=8[s]

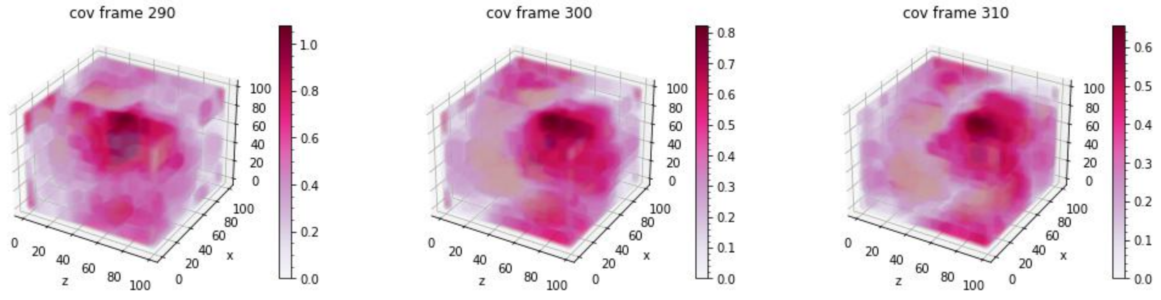

(j) Local CoV, t=9[s]

(k) Local CoV, t=10[s]

(l) Local CoV, t=11[s]

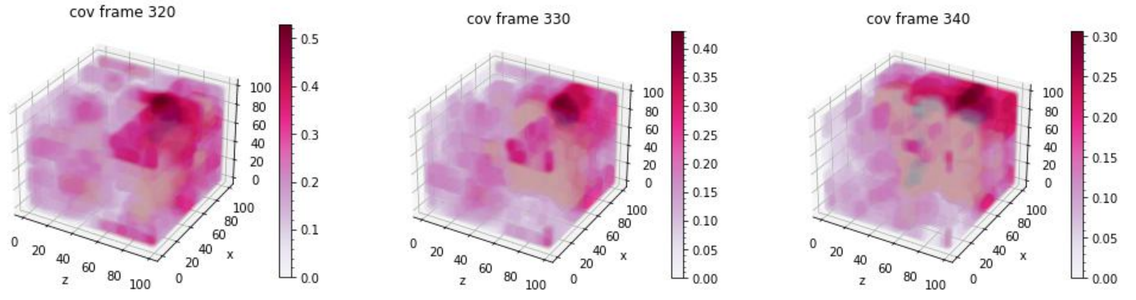

(m) Local CoV, t=12[s]

(n) Local CoV, t=13[s]

(o) Local CoV, t=14[s]

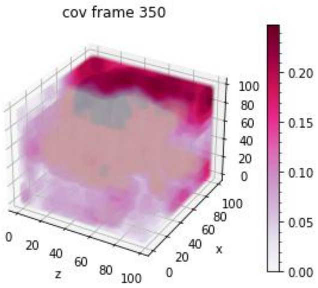

(a) Local CoV, t=15[s]

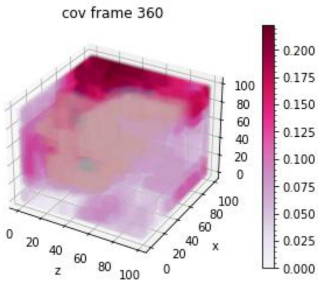

(b) Local CoV, t=16[s]

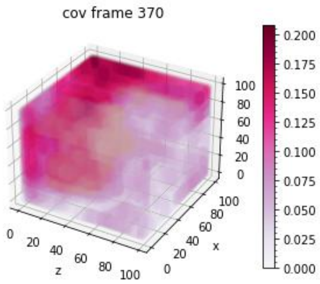

(c) Local CoV, t=17[s]

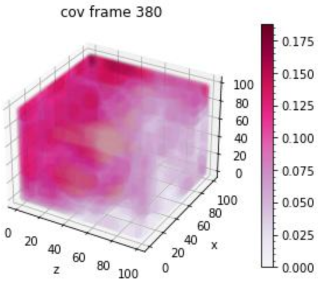

(d) Local CoV, t=18[s]

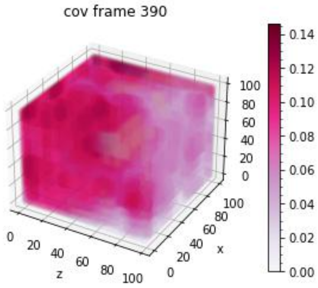

(e) Local CoV, t=19[s]

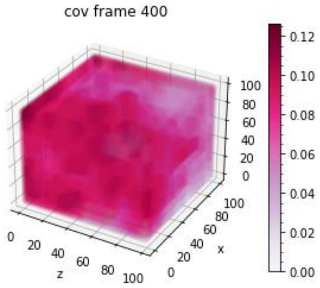

(f) Local CoV, t=20[s]

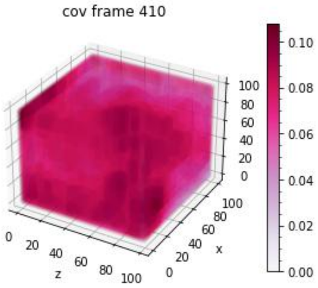

(g) Local CoV, t=21[s]

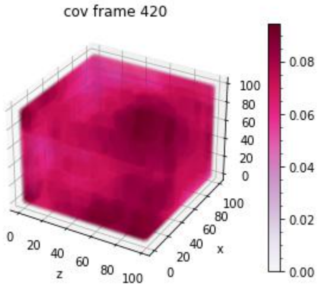

(h) Local CoV, t=22[s]

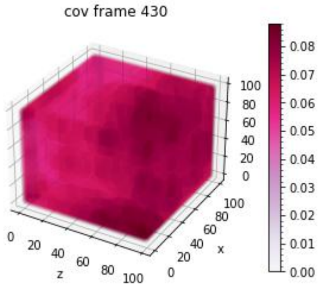

(i) Local CoV, t=23[s]

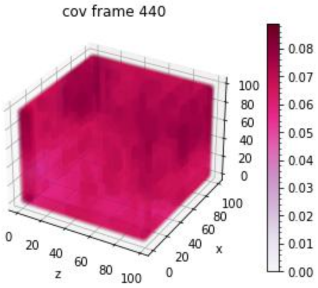

(j) Local CoV, t=24[s]

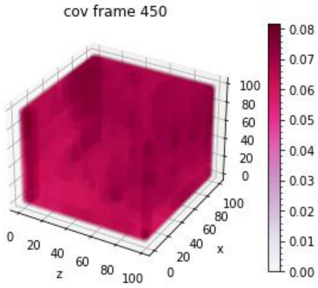

(k) Local CoV, t=25[s]

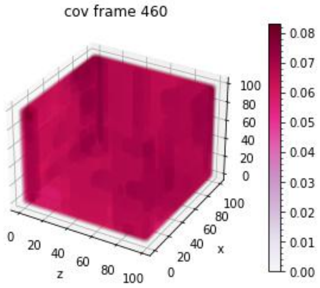

(l) Local CoV, t=26[s]

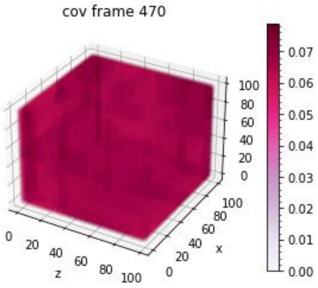

(m) Local CoV, t=27[s]

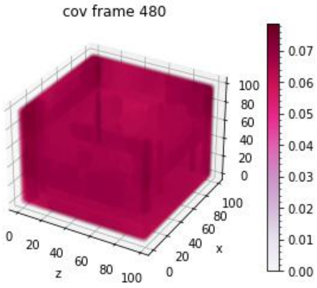

(n) Local CoV, t=28[s]

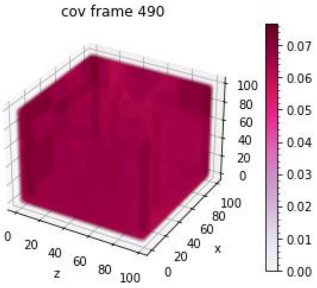

(o) Local CoV, t=29[s]

A.3. Experimental data reconstruction & local CoV

In the following pages the visualizations of 3D reconstruction from experimental frames are presented, sampled at each 0.4 s of the mixing process.

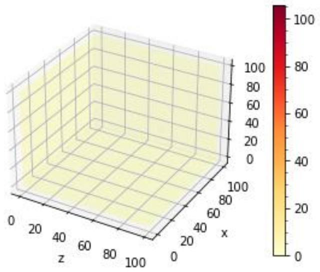

(a) Experimental data reconstruction, t=0[s]

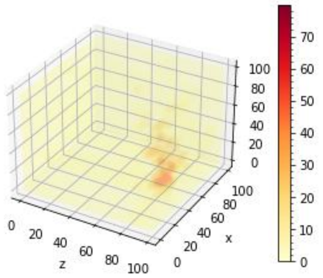

(b) Experimental data reconstruction, t=$4 \cdot 10^{-1}$[s]

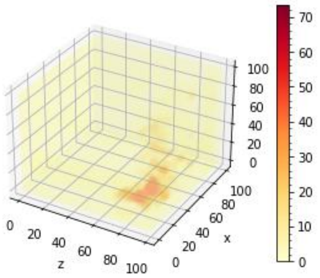

(c) Experimental data reconstruction, t=$8 \cdot 10^{-1}$[s]

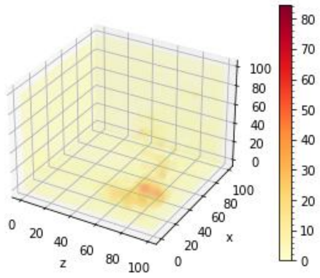

(d) Experimental data reconstruction, t=1.2[s]

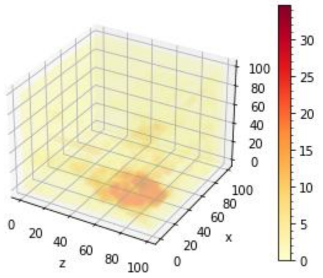

(e) Experimental data reconstruction, t=1.6[s]

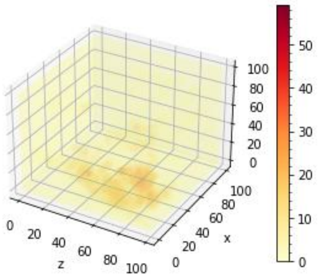

(f) Experimental data reconstruction, t=2[s]

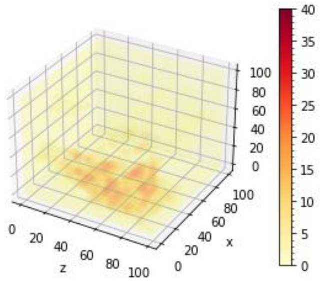

(g) Experimental data reconstruction, t=2.4[s]

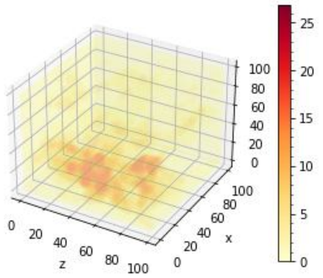

(h) Experimental data reconstruction, t=2.8[s]

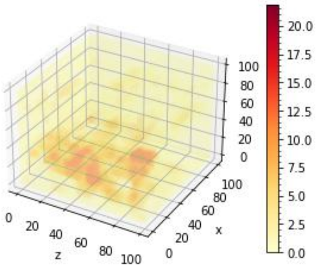

(i) Experimental data reconstruction, t=3.2[s]

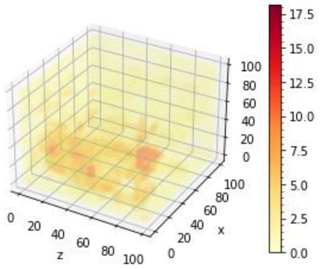

(j) Experimental data reconstruction, t=3.6[s]

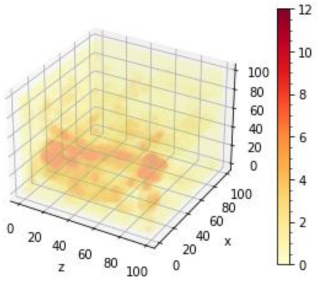

(k) Experimental data reconstruction, t=4[s]

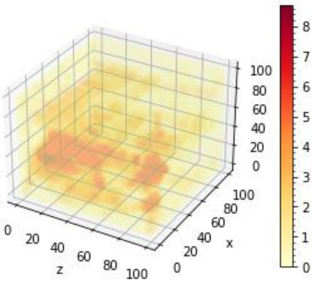

(l) Experimental data reconstruction, t=4.4[s]

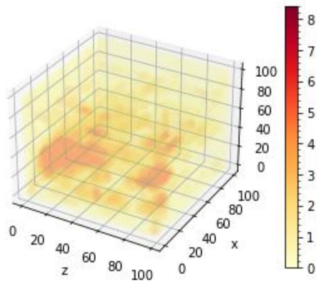

(a) Experimental data reconstruction, t=4.8[s]

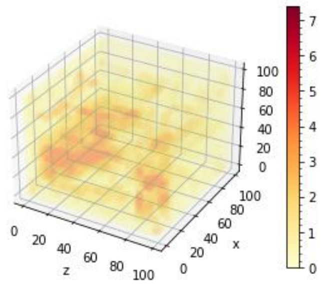

(b) Experimental data reconstruction, t=5.2[s]

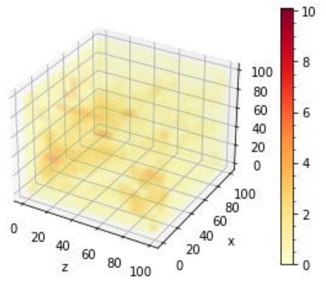

(c) Experimental data reconstruction, t=5.6[s]

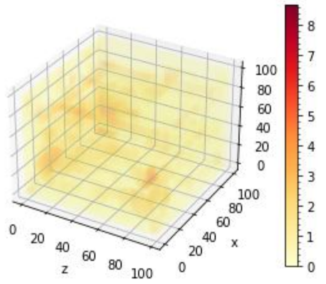

(d) Experimental data reconstruction, t=6[s]

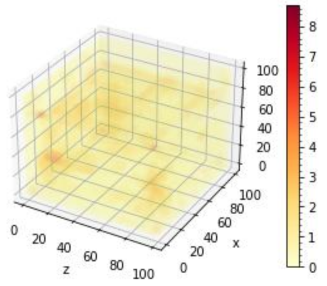

(e) Experimental data reconstruction, t=6.4[s]

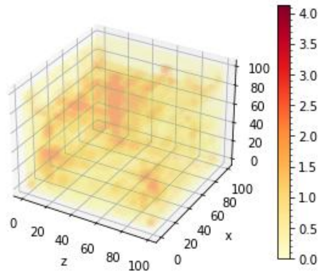

(f) Experimental data reconstruction, t=6.8[s]

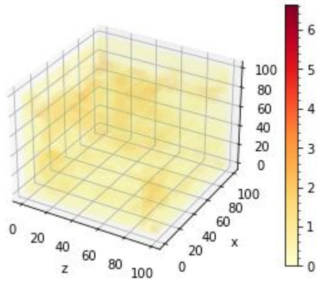

(g) Experimental data reconstruction, t=7.2[s]

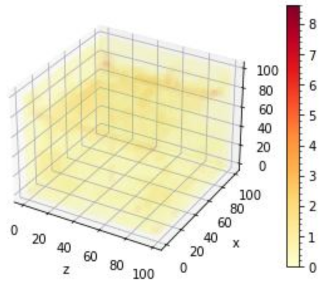

(h) Experimental data reconstruction, t=7.6[s]

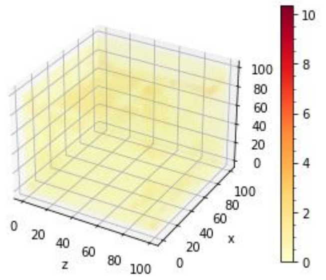

(i) Experimental data reconstruction, t=8[s]

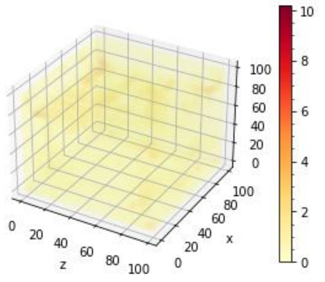

(j) Experimental data reconstruction, t=8.4[s]

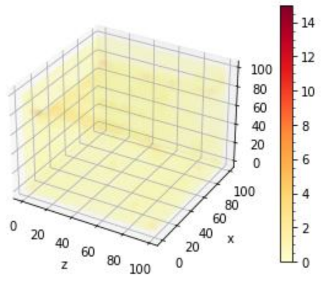

(k) Experimental data reconstruction, t=8.8[s]

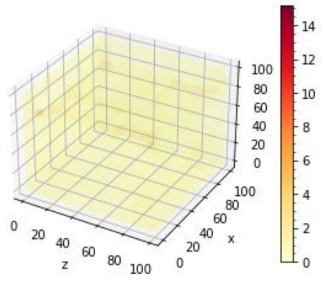

(l) Experimental data reconstruction, t=9.2[s]

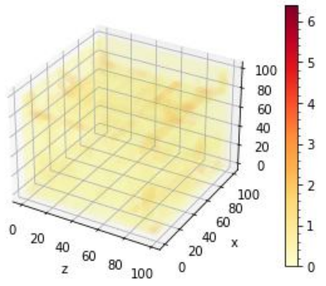

(m) Experimental data reconstruction, t=9.6[s]

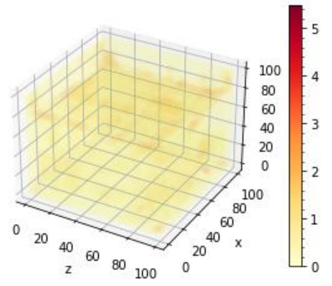

(n) Experimental data reconstruction, t=10[s]

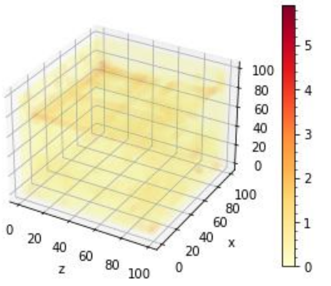

(o) Experimental data reconstruction, t=10.4[s]

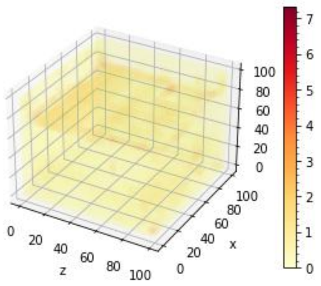

(a) Experimental data reconstruction, t=10.8[s]

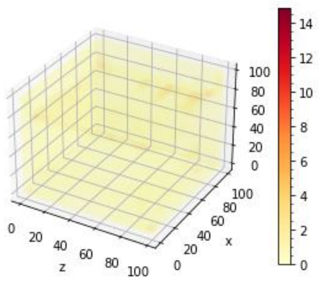

(b) Experimental data reconstruction, t=11.2[s]

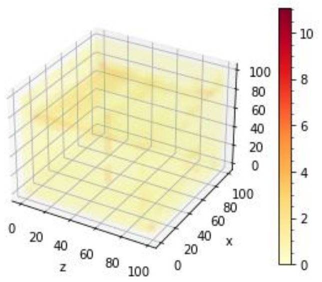

(c) Experimental data reconstruction, t=11.6[s]

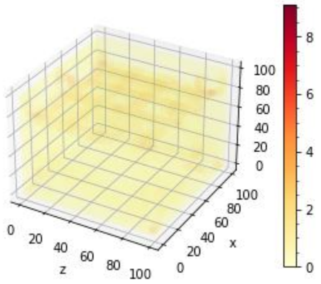

(d) Experimental data reconstruction, t=12[s]

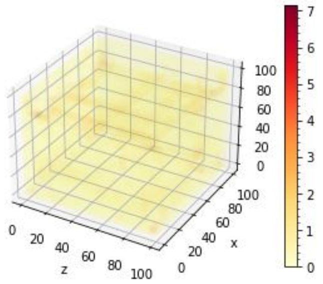

(e) Experimental data reconstruction, t=12.4[s]

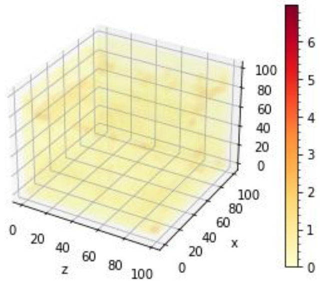

(f) Experimental data reconstruction, t=12.8[s]

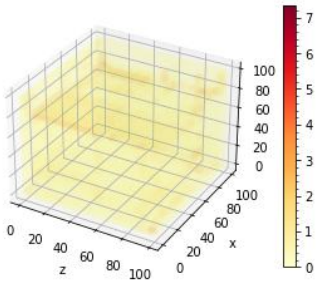

(g) Experimental data reconstruction, t=13.2[s]

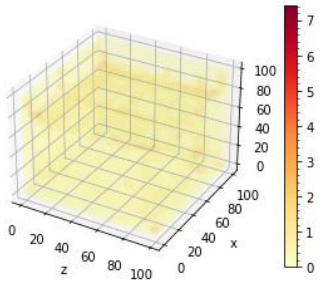

(h) Experimental data reconstruction, t=13.6[s]

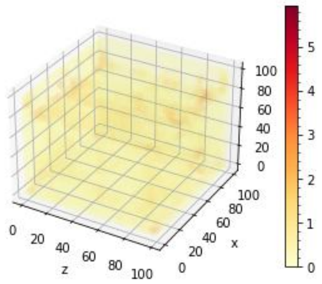

(i) Experimental data reconstruction, t=14[s]

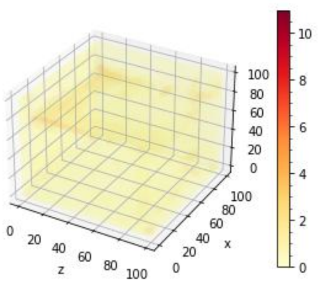

(j) Experimental data reconstruction, t=14.4[s]

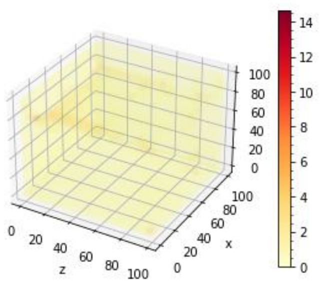

(k) Experimental data reconstruction, t=14.8[s]

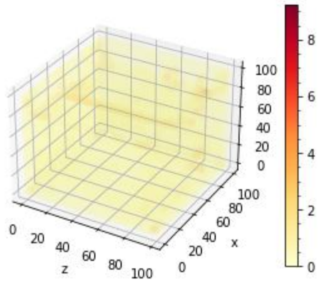

(l) Experimental data reconstruction, t=15.2[s]

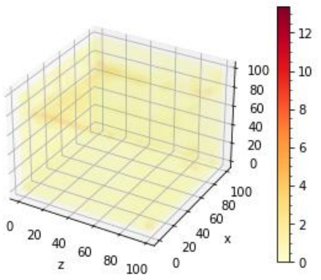

(m) Experimental data reconstruction, t=15.6[s]

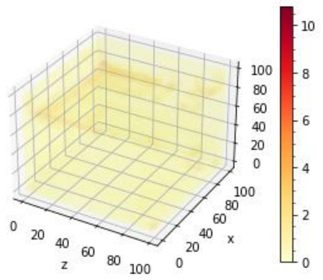

(n) Experimental data reconstruction, t=16[s]

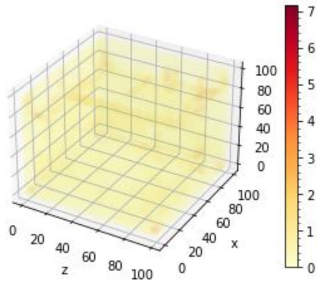

(o) Experimental data reconstruction, t=16.4[s]

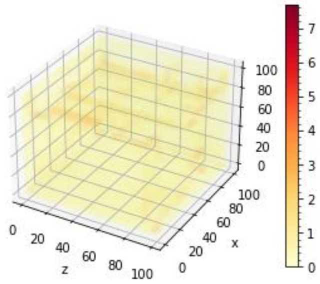

(a) Experimental data reconstruction, t=17.2[s]

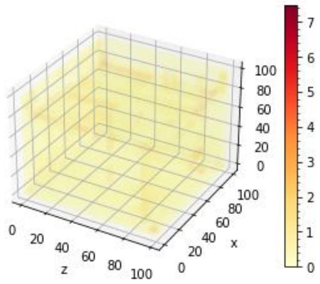

(b) Experimental data reconstruction, t=17.6[s]

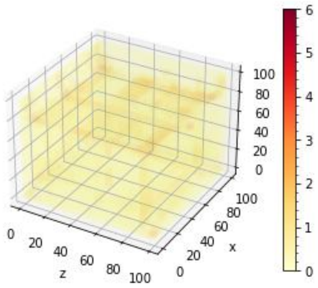

(c) Experimental data reconstruction, t=18[s]

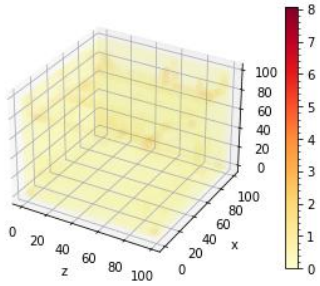

(d) Experimental data reconstruction, t=18.4[s]

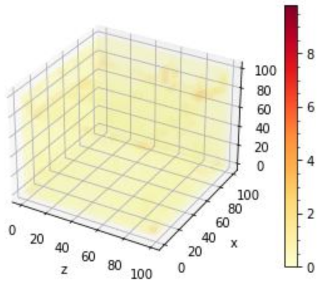

(e) Experimental data reconstruction, t=18.8[s]

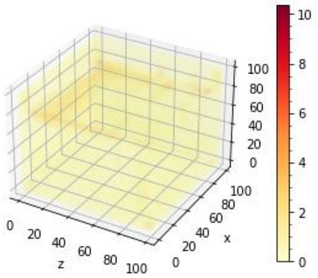

(f) Experimental data reconstruction, t=19.2[s]

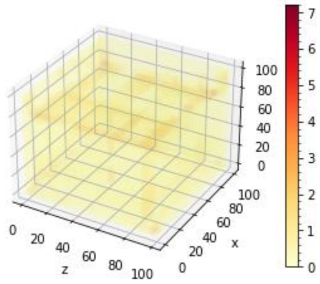

(g) Experimental data reconstruction, t=19.6[s]

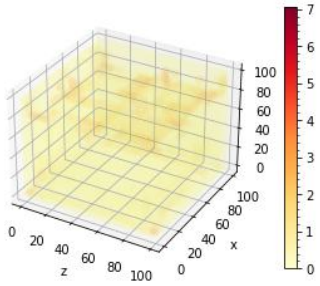

(h) Experimental data reconstruction, t=20[s]

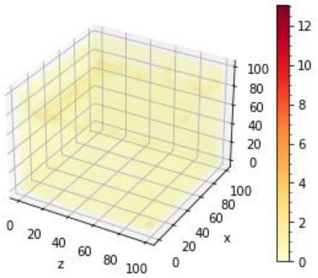

(i) Experimental data reconstruction, t=20.4[s]

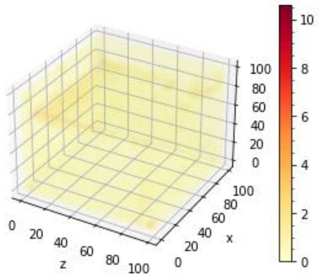

(j) Experimental data reconstruction, t=20.8[s]

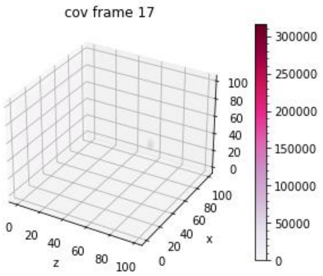

(a) Local CoV evaluation, t=0[s]

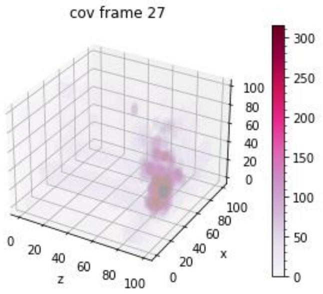

(b) Local CoV evaluation, t=$4 \cdot 10^{-1}$[s]

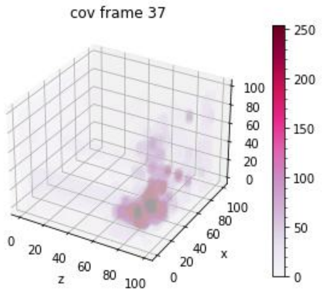

(c) Local CoV evaluation, t=$8 \cdot 10^{-1}$[s]

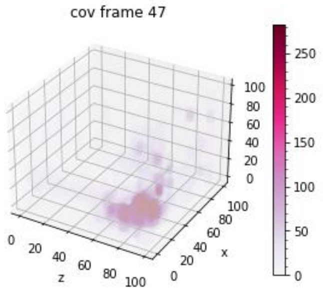

(d) Local CoV evaluation, t=1.2[s]

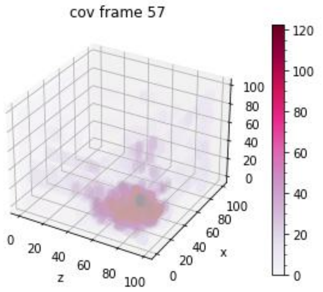

(e) Local CoV evaluation, t=1.6[s]

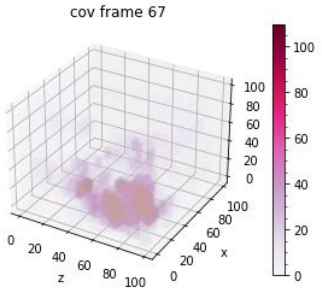

(f) Local CoV evaluation, t=2[s]

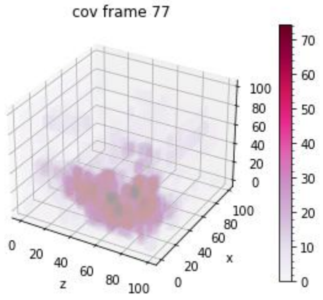

(g) Local CoV evaluation, t=2.4[s]

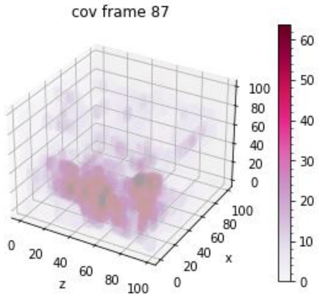

(h) Local CoV evaluation, t=2.8[s]

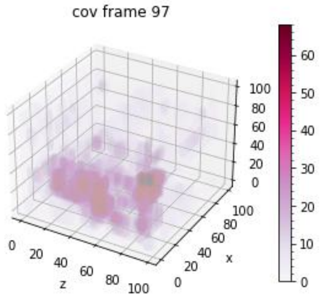

(i) Local CoV evaluation, t=3.2[s]

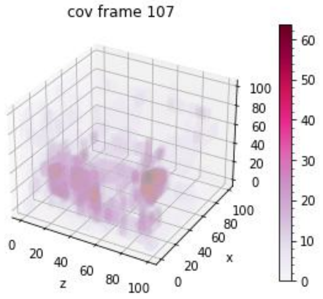

(j) Local CoV evaluation, t=3.6[s]

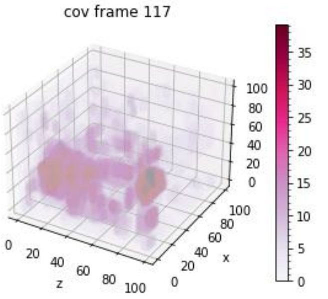

(k) Local CoV evaluation, t=4[s]

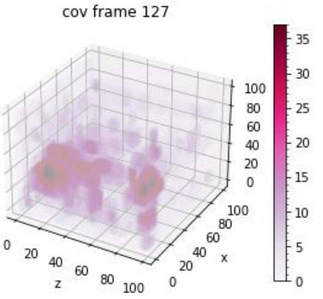

(l) Local CoV evaluation, t=4.4[s]

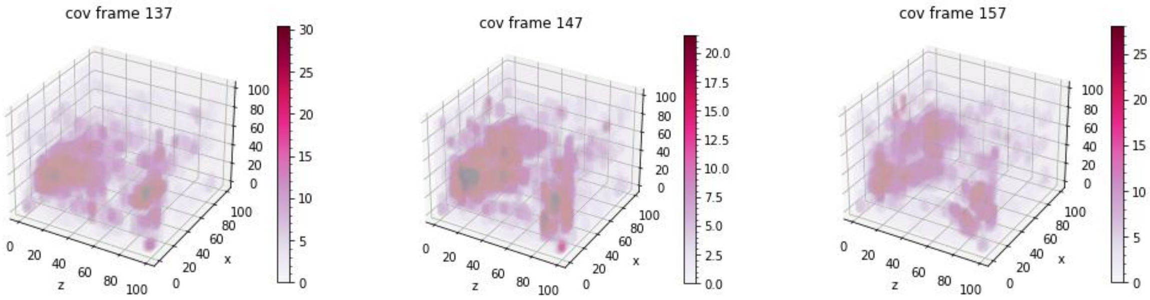

(a) Local CoV evaluation, t=4.8[s] **(b)** Local CoV evaluation, t=5.2[s] **(c)** Local CoV evaluation, t=5.6[s]

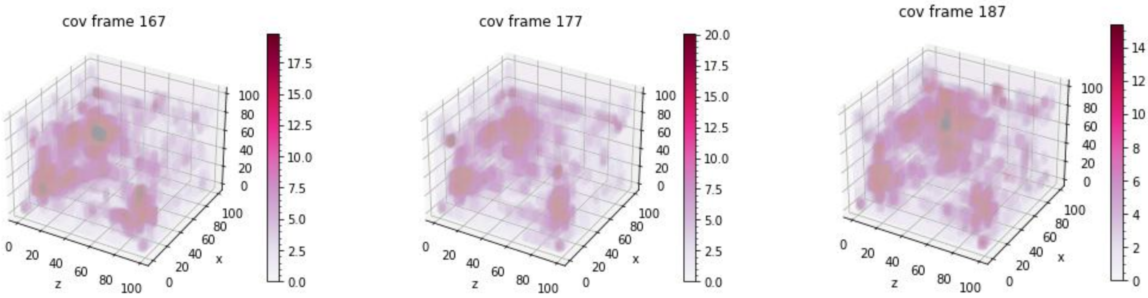

(d) Local CoV evaluation, t=6[s] **(e)** Local CoV evaluation, t=6.4[s] **(f)** Local CoV evaluation, t=6.8[s]

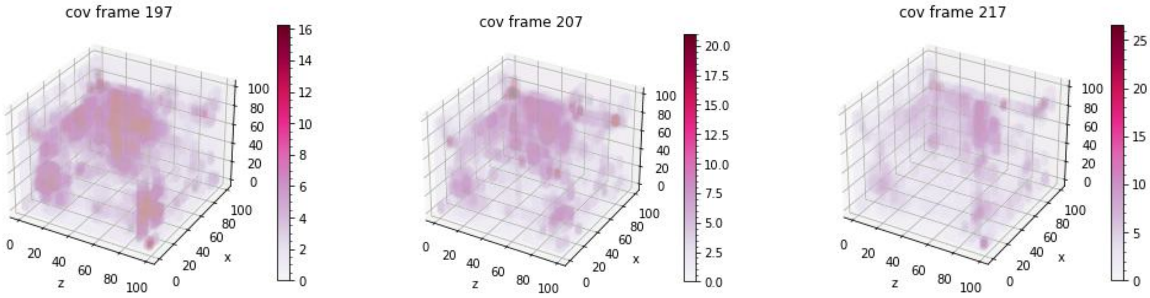

(g) Local CoV evaluation, t=7.2[s] **(h)** Local CoV evaluation, t=7.6[s] **(i)** Local CoV evaluation, t=8[s]

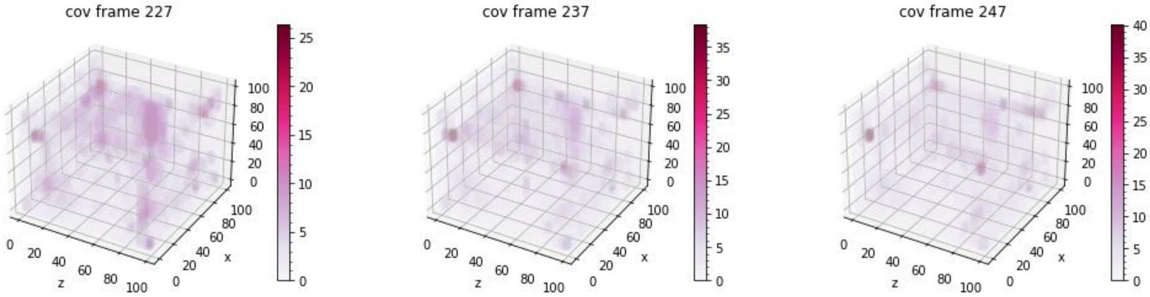

(j) Local CoV evaluation, t=8.4[s] **(k)** Local CoV evaluation, t=8.8[s] **(l)** Local CoV evaluation, t=9.2[s]

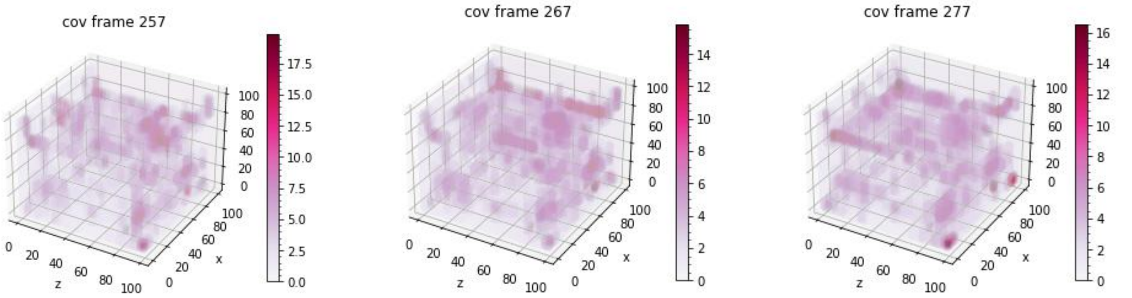

(m) Local CoV evaluation, t=9.6[s] **(n)** Local CoV evaluation, t=10[s] **(o)** Local CoV evaluation, t=10.4[s]

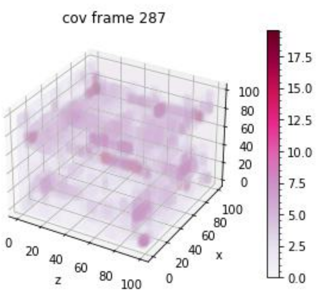

(a) Local CoV evaluation, t=10.8[s]

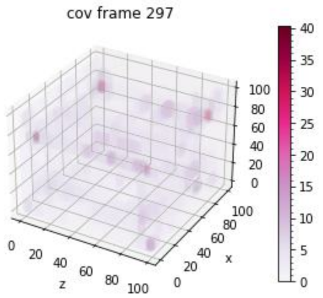

(b) Local CoV evaluation, t=11.2[s]

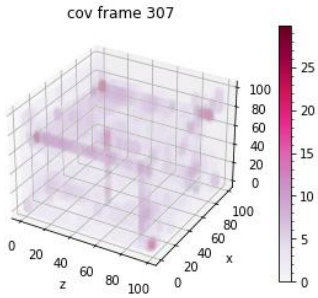

(c) Local CoV evaluation, t=11.6[s]

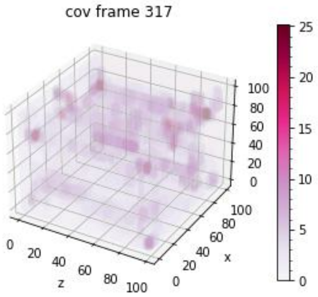

(d) Local CoV evaluation, t=12[s]

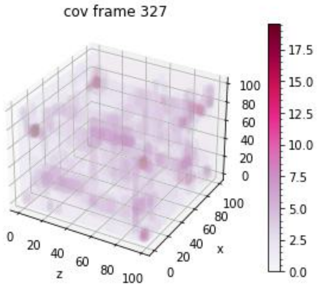

(e) Local CoV evaluation, t=12.4[s]

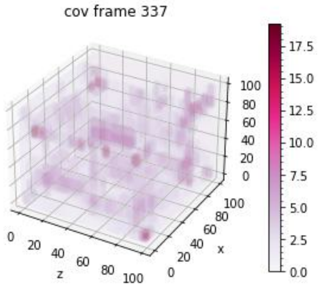

(f) Local CoV evaluation, t=12.8[s]

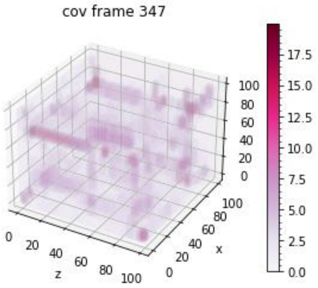

(g) Local CoV evaluation, t=13.2[s]

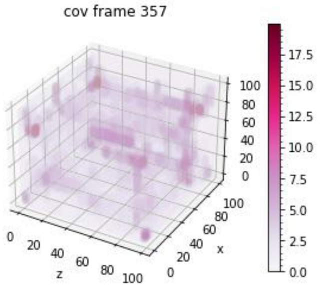

(h) Local CoV evaluation, t=13.6[s]

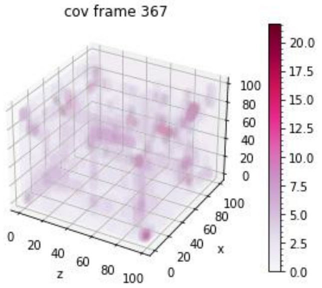

(i) Local CoV evaluation, t=14[s]

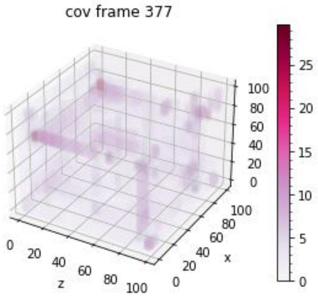

(j) Local CoV evaluation, t=14.4[s]

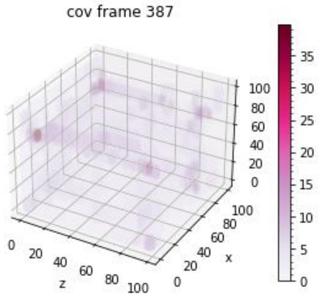

(k) Local CoV evaluation, t=14.8[s]

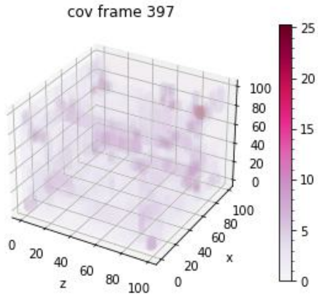

(l) Local CoV evaluation, t=15.2[s]

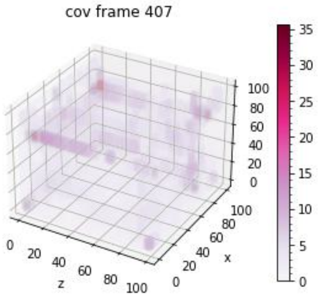

(m) Local CoV evaluation, t=15.6[s]

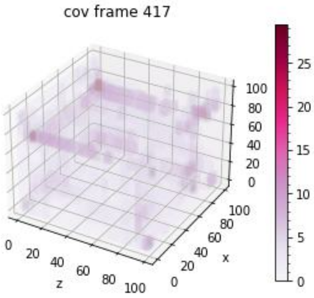

(n) Local CoV evaluation, t=16[s]

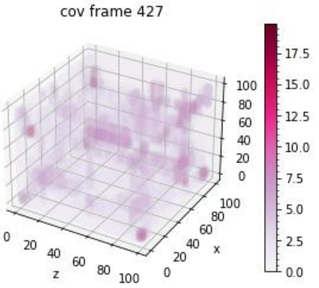

(o) Local CoV evaluation, t=16.4[s]

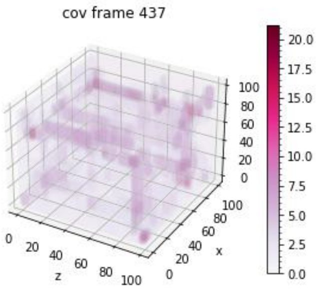

(a) Local CoV evaluation, t=17.2[s]

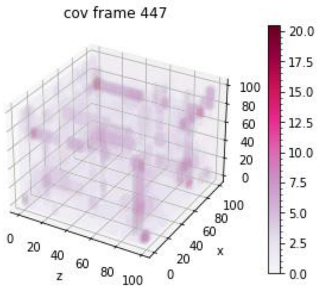

(b) Local CoV evaluation, t=17.6[s]

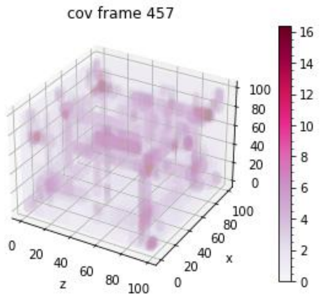

(c) Local CoV evaluation, t=18[s]

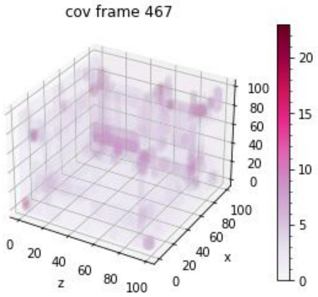

(d) Local CoV evaluation, t=18.4[s]

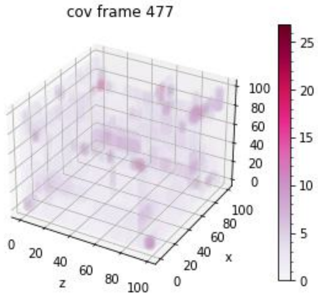

(e) Local CoV evaluation, t=18.8[s]

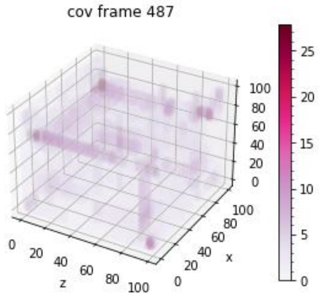

(f) Local CoV evaluation, t=19.2[s]

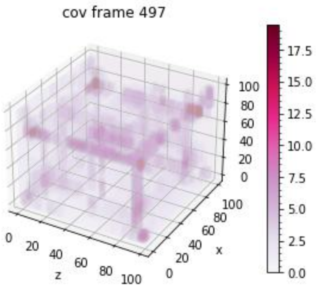

(g) Local CoV evaluation, t=19.6[s]

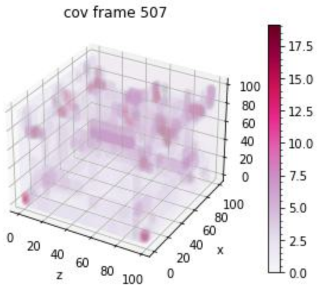

(h) Local CoV evaluation, t=20[s]

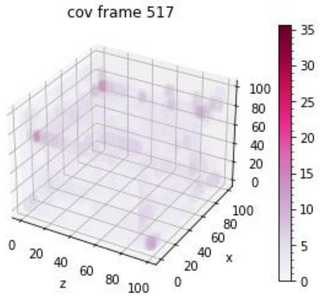

(i) Local CoV evaluation, t=20.4[s]

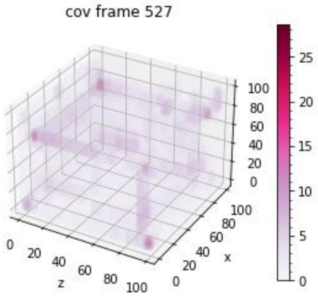

(j) Local CoV evaluation, t=20.8[s]

A.4. Experimental data mixing maps

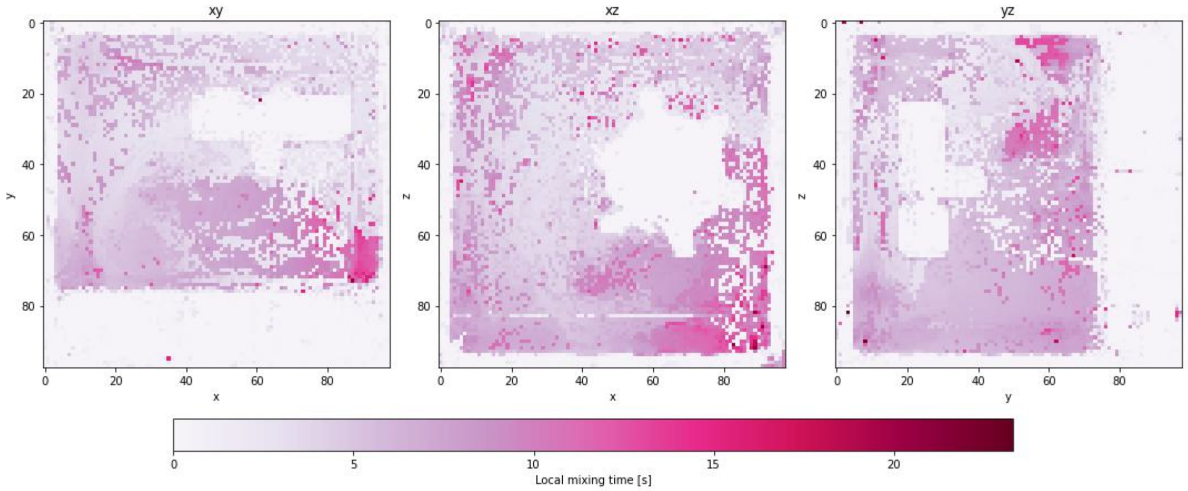

Figure A.21: Experimental data non-normalised (92%) mixing map

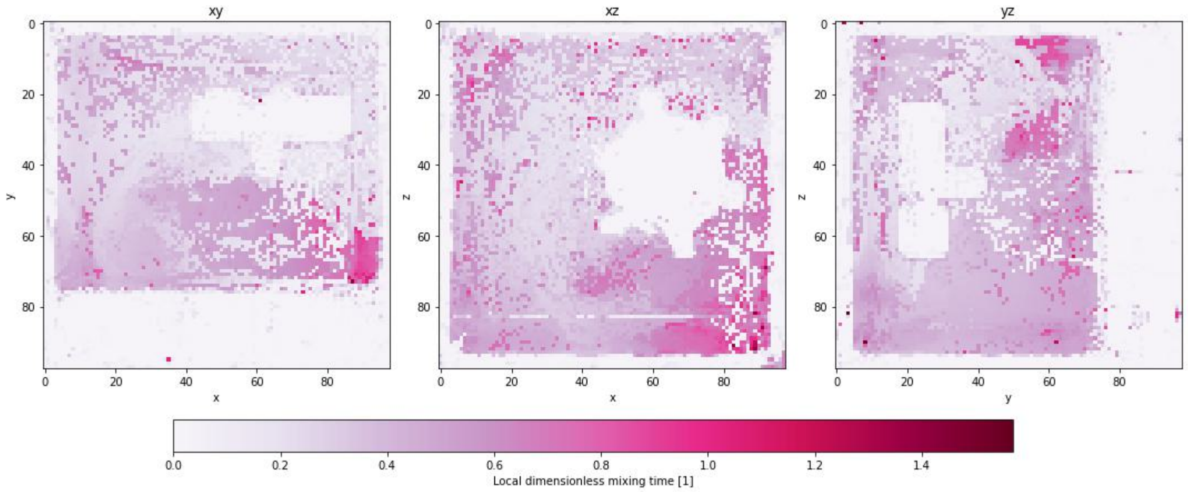

Figure A.22: Experimental data normalised (92%) mixing map

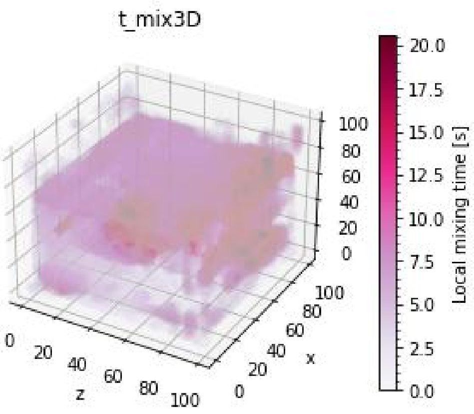

Figure A.23: Experimental data 3D non-normalised (92%) mixing map

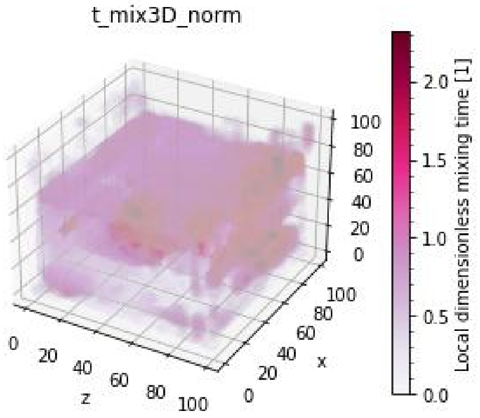

Figure A.24: Experimental data (92%) 3D normalised mixing map

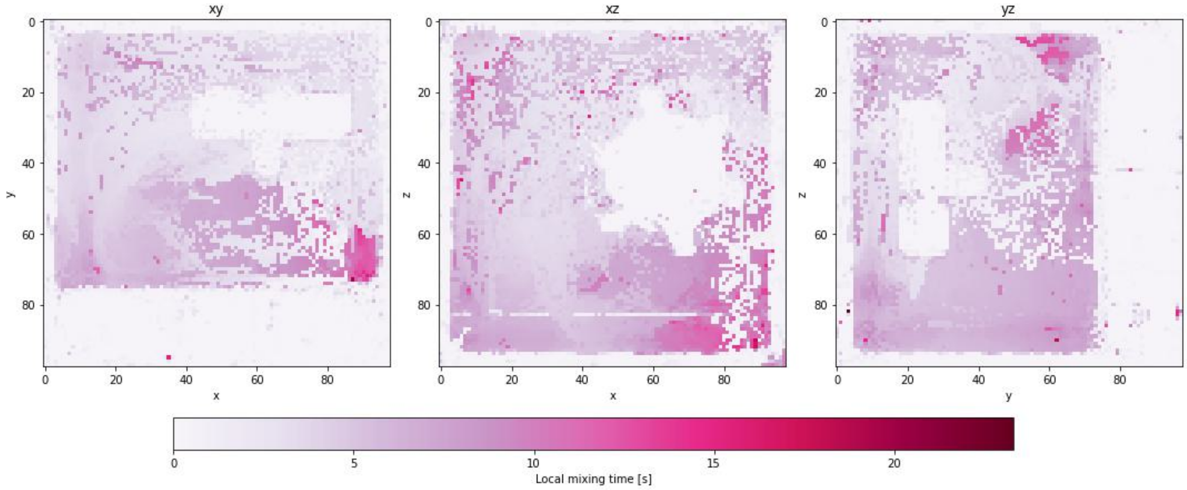

Figure A.25: Experimental data non-normalised (85%) mixing map

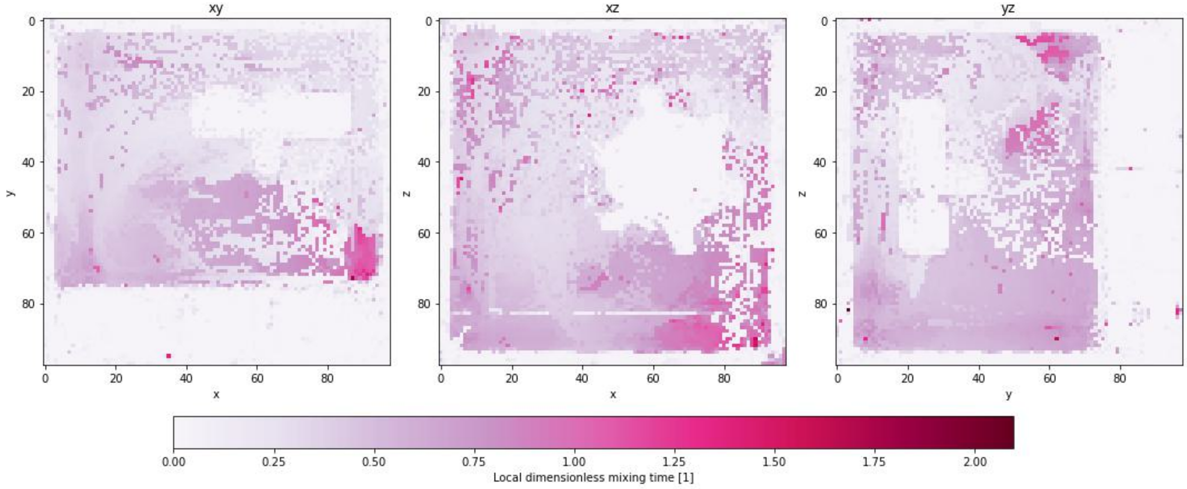

Figure A.26: Experimental data normalised (85%) mixing map

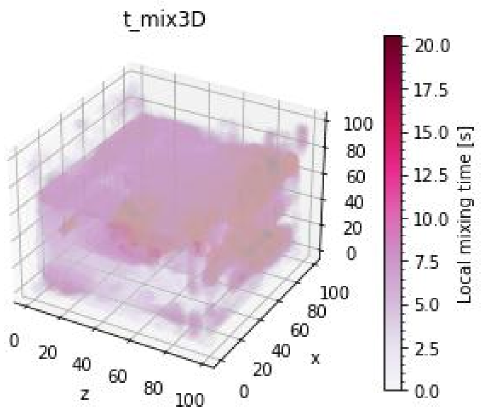

Figure A.27: Experimental data 3D non-normalised (85%) mixing map

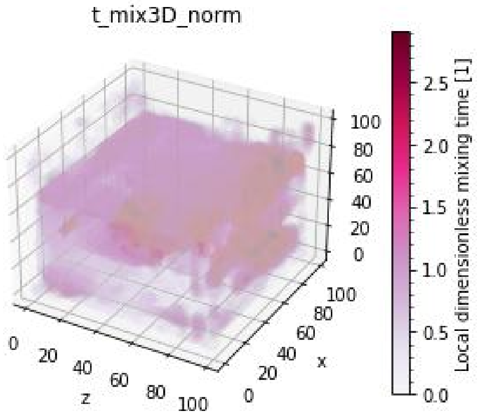

Figure A.28: Experimental data (85%) 3D normalised mixing map